



POLITECNICO
MILANO 1863

DEPARTMENT
OF ENERGY

DOCTORAL PROGRAMME IN
ENERGY AND NUCLEAR SCIENCE AND TECHNOLOGY

DEVELOPMENT OF NANOSTRUCTURED
MATERIALS FOR HIGH INTENSITY
LASER-PLASMA APPLICATIONS

Doctoral Dissertation of:
Davide Orecchia

Supervisor:

Prof. Matteo Passoni

Co-supervisor:

Prof. Alessandro Maffini

Tutor:

Prof. Valeria Russo

The Chair of the Doctoral Program:

Prof. Vincenzo Dossena

2024 – Cycle XXXVI

Abstract

LASER-MATTER interaction applications have gathered significant attention in recent years, due to their high scientific, technological and societal relevance: from clean energy production through inertial confinement fusion, to laser-driven particle accelerators for medical or security applications. Toward the aim to fulfill their potential, the coupling between laser and matter is a fundamental aspect. Nanostructured low-density materials are particularly promising candidates in this regard, with the ability to enhance laser-matter interaction and energy absorption. This PhD thesis work investigates their production through the versatile nanosecond and femtosecond pulsed laser deposition techniques (ns-PLD and fs-PLD), finding the relationship between process parameters and material properties. The insight gained are exploited for the design and production of nanostructured targets for high-intensity laser-matter interaction experiments: entirely produced double-layer targets (DLTs) for laser-driven particle acceleration, carbon nanofoams and nanostructured materials as ablaters for inertial confinement fusion (ICF), and hydrogen-enriched boron-based nanofoams for proton-boron fusion. The results of the laser-matter interaction experiments performed on three laser facilities with significantly different properties confirm the potential of nanostructured materials and nanofoams as laser-matter interaction enhancers, and provide indications on the dependence of the ideal target characteristics on the laser properties. This consolidates the need for a versatile material production technique such as pulsed laser deposition, able to produce nanostructured materials with a wide variety of densities, morphologies and compositions.

Contents

I	State of the art and thesis goals	5
1	Introduction to laser-matter interaction	7
1.1	Pulsed laser technology	7
1.2	Fundamentals of laser-matter interaction	10
2	Overview of select laser-matter interaction applications	19
2.1	Laser-driven particle acceleration	19
2.2	Inertial Confinement Fusion (ICF)	26
2.3	Proton-Boron fusion	31
3	Nanostructured materials and nanofoams	35
3.1	Nanostructured materials morphology and properties	35
3.2	Nanofoams synthesis methods	39
3.3	Laser-matter interaction with micro and nanostructured materials	45
4	Thesis goals and methods	51
4.1	Thesis objectives and personal contribution	51
4.2	Nanosecond and femtosecond Pulsed Laser Deposition	53
4.3	Nanofoam characterization techniques	54
4.4	Introduction to the laser facilities of this thesis work	56

II	Experimental investigation on nanofoam production with Pulsed Laser Deposition	59
5	Carbon nanofoam production through ns-PLD and fs-PLD	61
5.1	Fractal aggregate analysis	62
5.2	Morphological analysis	68
5.3	Raman analysis	72
5.4	Average density characterization	74
6	Versatile nanofoam synthesis through fs-PLD	79
6.1	Morphological characterization	80
6.2	Thickness evolution and deposition rate	84
6.3	Average density characterization and modeling	87
III	Target production for laser-matter interaction experiments	93
7	Carbon nanofoam Double-Layer Targets for particle acceleration	95
7.1	VEGA 3 laser facility, experimental setup and goals	95
7.2	Target design and production	97
7.3	Preliminary results	99
8	Carbon nanofoams as ICF ablaters	103
8.1	ABC laser facility, experimental setup and goals	104
8.2	Preparatory hydrodynamic simulations	105
8.3	Target design and production with PLD	110
8.4	Experimental campaign results	113
9	Hydrogen-enriched boron nanofoams for proton-boron fusion experiments	117
9.1	TARANIS laser facility, experimental setup and goals	117
9.2	Boron-based targets design and production with fs-PLD	119
9.3	Experimental campaign results	122
IV	Conclusions and perspectives	125
	Bibliography	133

Introduction

The field of laser-matter and laser-plasma interaction is gaining increasing interest from the scientific community in recent years, owing to the multiple applications of great scientific, technological and societal impact. At the same time, the scientific and technological complexity inherent to laser-matter and laser-plasma interaction cannot be overstated, particularly for the more demanding applications—that indeed are those with the higher societal impact, such as inertial confinement fusion or laser-driven isotope production for medical application. In all these, the coupling between laser and matter is a fundamental aspect, and its enhancement can be the key to reach technological viability. In order to do so, near-critical density and nanostructured materials are gaining increasing interest as laser-facing components, with very promising results. A specific influence of the nanostructure morphology on the laser-matter interaction process has also been demonstrated, highlighting the need for a proper design and control of the nanostructured targets. Which is also fundamental in regard to the variety of regimes of interest for different applications—tabletop or high intensity lasers, ultrashort pulses or high energy nanosecond pulses—each with its own target requirement for optimal laser-matter coupling.

Currently exploited material science techniques to obtain nanostructured materials and nanofoams present significant limitation in this regard: chemical methods can have difficulties in controlling the material structure down to the nanoscale, each is generally limited to a specific class of material (or even a few elements/compounds depending on the reaction), and unwanted byproducts may be present. A physical vapour deposition technique such as Pulsed Laser Deposition (PLD) can address many of these limitations, as a

Contents

bottom-up approach with potentially great nanostructure control, stoichiometric growth capabilities and great flexibility thanks to the many tunable process parameters. One process parameter not often considered is the laser pulse duration: while nanosecond lasers are routinely part of PLD systems (ns-PLD), ultrafast ablation with femtosecond lasers—in the much less explored fs-PLD approach—could provide an even greater flexibility in material choice, thanks to the electronic ablation mechanism and direct nanoparticle production. This PhD thesis work is thus focused on the production and characterization of nanofoams and nanostructured materials through PLD, together with their test as laser-facing components in high-intensity laser-matter interaction experimental campaigns, for multiple applications requiring different laser properties.

Structure of the thesis

The PhD thesis is organized as follows:

Part I: The first Part of the thesis aims at introducing the topic and all the elements necessary for the following developments, from an analysis of the relevant state of the art to the objectives guiding the research activity. In Chapter 1, laser technology and laser-matter interaction fundamentals are introduced, as unifying elements of this thesis work—central for both the PLD technique and the high-intensity laser-matter interaction applications. Regarding the latter, the most relevant for this thesis work are presented in Chapter 2: laser-driven particle acceleration, inertial confinement fusion (ICF), and proton-boron fusion. Chapter 3 introduces nanostructured materials and nanofoams as a promising mean to enhance laser-matter coupling, together with their synthesis techniques. In light of the previous discussion, the first Part ends with the presentation of the thesis objectives in Chapter 4, along with the methods exploited to achieve them. The nanostructured material production technique of choice (PLD) is described, along with the main material characterization techniques exploited, and the laser facilities on which laser-matter interaction experiments have been performed.

Part II: In this second Part, the results regarding the investigation into PLD production of nanostructured materials and nanofoams are reported. Chapter 5 deals with the comparative analysis between the well-established ns-PLD and the unconventional fs-PLD, with a focus on carbon nanofoams. The effects of the main deposition parameters are investigated, and their effect on the nanofoam nano, micro and macroscale

properties are established. The analysis is extended in Chapter 6, where a greater variety of elements are investigated, and the flexibility of fs-PLD as nanofoam production method is demonstrated. In both Chapters, special attention is given to the average nanofoam density, being one of the most relevant properties for laser-matter interaction applications.

Part III: This Part, capitalizing on the insight obtained in the previous one, is dedicated to the experimental test of specifically designed nanofoam-based targets in high-intensity laser-matter interaction campaigns. In Chapter 7, entirely produced carbon nanofoam-based double-layer targets (DLTs) are tested on the petawatt-class laser VEGA 3, as targets for efficient proton acceleration. Carbon nanofoams and nanostructured materials are also investigated as potential ablator material for direct-drive ICF in Chapter 8, able to increase the laser absorption and ablation loading on the substrate. The experimental activity is carried out on the ABC laser at the ENEA Frascati laboratories. Finally, Chapter 9 demonstrates the value of the fs-PLD versatility, able to produce hydrogen-enriched boron nanofoams for enhanced alpha particle production in proton-boron fusion experiments. The experimental campaign is performed on the Taranis laser at Queen’s University Belfast. In all these cases, data analysis is still ongoing, therefore the discussion is limited to preliminary results.

Part IV: In this final Part, the conclusions of the whole thesis work are drawn, together with a mention of interesting future research perspectives.

Publications and research activity

The following articles were published in the framework of this PhD work:

- Maffini A., **Orecchia D.**, Pazzaglia A., Zavelani-Rossi M. and Passoni M., “*Pulsed laser deposition of carbon nanofoam*”, Applied Surface Science **599** (2022): 153859
- Maffini A., Mirani F., Galbiati M., Ambrogioni K., Gatti F., De Magistris M.S.G., Vavassori D., **Orecchia D.**, Dellasega D., Russo V. and Zavelani-Rossi M., “*Towards compact laser-driven accelerators: exploring the potential of advanced double-layer targets*”, EPJ Techniques and Instrumentation **10.1** (2023): 15
- Maffini A., Cipriani M., **Orecchia D.**, Ciardiello V., Formenti A., Consoli F., and Passoni M., “*Numerical Study of Carbon Nanofoam Tar-*

Contents

gets for Laser-Driven Inertial Fusion Experiments”, Laser and Particle Beams **2023** (2023): 9

- **Orecchia D.**, Maffini A., Zavelani-Rossi M. and Passoni M., “*Versatile synthesis of nanofoams through femtosecond Pulsed Laser Deposition*”, Small Structures **5** (2024): 2300560

The results of the research activity were also presented in the following international conferences and workshops:

- Targetry for High Repetition Rate Laser-Driven Sources Workshop (TARG5), HZDR (Dresden), 25th-27th October 2021, with the **oral contribution** “*Advancements in double-layer target production for enhanced laser-driven ion acceleration*”
- 2nd International Workshop on Proton-Boron Fusion, Catania, 5th-8th September 2022, with the **oral contribution** “*Pulsed laser deposition of boron-based targets for p-11B studies*”
- CMD30-FisMat joint conference, Milano, 4th-8th September 2023, with the **oral contribution** “*Femtosecond Pulsed Laser Deposition of low-density nanofoams*”
- 3rd International Workshop on Proton-Boron Fusion, Prague (& ELI Beamlines), 2nd-5th October 2023, with the **oral contribution** “*Advancements in Pulsed Laser deposition of boron-based targets for p-¹¹B studies*”

During the PhD I also participated in multiple experimental campaigns:

- ENEA Centro Ricerche Frascati, laser-matter interaction experimental campaign on the ABC laser, 27th February 2023 - 10th March 2023
- Queen’s University Belfast, proton-boron fusion experimental campaign on the TARANIS laser, 31st July 2023 - 4th August 2023
- Centro de Laseres Pulsados (CLPU), Salamanca, proton and neutron acceleration campaign with advanced targets on the VEGA 3 laser, 18th - 24th November 2023

Lastly, I co-supervised 3 MsC thesis in Nuclear Engineering (Vittorio Ciardiello, Maria Sole Galli De Magistris and Alessandro Milani).



Part I

State of the art and thesis goals

CHAPTER *1*

Introduction to laser-matter interaction

This first Chapter gives an introduction to the physics of laser-matter interaction, unifying factor of this thesis work. In Section 1.1, the technology of pulsed lasers is briefly introduced, including the latest achievements in ultra-short and high intensity lasers. The main features of laser-matter interaction are discussed in Section 1.2, considering both the ablation process typical of moderate intensity lasers and the peculiarities of high-intensity laser-plasma interaction, along with plasma dynamics and relativistic effects.

1.1 Pulsed laser technology

Since the first laser system devised and operated by Maiman in 1960 [1], lasers have been at the forefront of technology, with several successful applications in the most diverse fields of engineering, from information technology to material science and characterization. The reason can be found in the laser light unique properties, originated from the physics of a stimulated emission process happening in a cavity: extreme spatial and temporal coherence, allowing tight focusing even at high distances, monochromaticity, and potential to reach considerably high powers. Moreover, since the accumulation of energy in the excited levels of the laser active material—for later release through stimulated emission of radiation—is generally achieved with

optical excitation (e.g. flashlamps), both continuous wave and pulsed laser operation can be achieved. Pulsed lasers in particular, thanks to the high concentration of energy at shorter timescales, were exploited to achieve higher instantaneous powers and intensities, paving the way to novel applications such as nonlinear optics—as the laser approached the atom electric field of 10^8 V/m. Historically, the first technique developed was Q-switching [2], allowing nanosecond pulses through fast periodic modulation of the cavity losses. Further reduction of the pulse duration was achieved thanks to a different technique, mode-locking [3], by constructive interference of different cavity modes. Picosecond or tens of femtosecond pulses can be obtained in this way, down to just a few optical cycles. Both techniques are still exploited in current lasers: Q-switching is limited to nanosecond pulse duration, but can reach higher energies per pulse, while the shorter femtosecond pulses achievable in mode-locking are limited in the energy output per pulse.

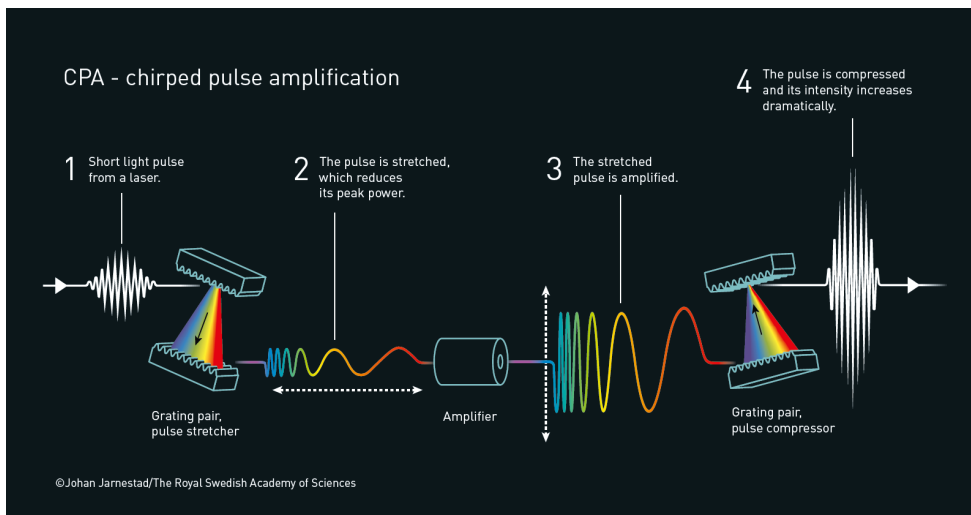


Figure 1.1: Schematic representation of the Chirped Pulse Amplification (CPA) technique (from [4]).

Q-switching and mode-locking can be exploited to reach intensities in the order of 10^{10} W/cm², and up to 10^{14} W/cm² with further amplification stages. Nevertheless, an upper limit on the energy (and thus intensity) increase comes from the damage threshold of the optical components ($\sim 10^9$ W/cm²), which halted the growth in laser intensity for more than a decade in the '70s. A Nobel prize worthy idea was needed for further advancements: the Chirped Pulse Amplification (CPA) scheme, depicted in Figure 1.1, devised by Donna Strickland and Gérard Mourou [5]. To counteract the issues related with a too high laser intensity on the optics and gain material, the

Another class of large-scale laser facilities worth mentioning is related to the research into laser-driven Inertial Confinement Fusion (ICF), where hundreds of high energy laser beams are exploited to compress and heat small spherical pellets to fusion relevant conditions. Together with state-of-the-art beam transport, amplification, control and synchronization lines, the main figure of merit of those facilities is the total laser energy that can be provided (megajoule and higher), within a few tens of nanoseconds. The National Ignition Facility (NIF), located at Lawrence Livermore National Laboratory in the US, is the first example of such a facility, operative since 2010 [10]. It consists of 192 beamlines of neodymium-doped phosphate glass lasers, pumped through multiple stages by high energy flashlamps. After amplification, the 1053 nm infrared laser is converted to UV (third harmonic, 351 nm) allowing a better energy delivery and pellet compression. A total of 1.8 MJ energy can be achieved. In Europe, France is currently building a similar facility, the Laser Megajoule [11]: 176 UV beams with nanosecond pulse duration will deliver a total energy exceeding 1 MJ. The facility installation and commissioning is currently underway, and experimental activity with a fraction of the total beams is being performed. The facility also includes PETAL, a high intensity Petawatt laser system (few kJ pulse energy, 500 fs - 10 ps pulse duration), with multiple interesting applications if coupled to the main LMJ beams (e.g. laboratory astrophysics, fast ignition ICF).

Beside high intensity and high energy lasers—and their building-sized facilities—the same advancements in laser technology led to the diffusion of tabletop short pulse lasers, limited in size but still able to reliably provide few mJ laser pulses at few tens of fs and kHz repetition rate. They are of interest for various lab-scale application, in particular in the fields of material science and laser-matter interaction (and central to this thesis work, as will be clear in the following).

1.2 Fundamentals of laser-matter interaction

The effects that can arise following the interaction of a laser pulse with matter can be the most varied, with a rich underlying physics [12, 13]. Needless to say, both the properties of matter—such as aggregation state, optical and electronic properties, surface features, physical properties—and those of the laser—pulse duration, intensity, wavelength—determine the laser-matter interaction evolution and the subset of processes that can take place under the specific conditions. Considering the scope of this thesis, the focus will be on the interaction of both moderate and high intensity lasers—from $\sim 10^8 - 10^{12}$ to $> 10^{20}$ W/cm² and pulse duration ranging from femtoseconds to nanoseconds—with solid materials. Moreover, since ionization and

subsequent plasma formation are inevitable when a sufficiently high intensity is reached ($\sim 10^{13} - 10^{14}$ W/cm²) laser-plasma interaction is also discussed.

When a laser pulse interacts with a non-transparent solid material it can penetrate only for a few nanometers, the so-called skin depth, where an evanescent electromagnetic field is present and absorption can take place. Part of the laser pulse is reflected or diffused, depending on the surface roughness and opacity/reflectivity. The remaining fraction can be absorbed, thanks to the coupling between the laser pulse electromagnetic field and the electrons of the solid material, through processes such as *inverse bremsstrahlung* [13]. Electron-phonon interactions are then the mean through which the laser energy, first delivered to the electrons, can finally be transferred to the lattice ions, and heating occurs. Depending on the amount of laser energy provided, melting and evaporation can take place, leading to material ablation and a variety of other phenomena according to the laser intensity. As a matter of fact, the most important parameter to be considered in this process is not the laser energy by itself, but the laser fluence (i.e. laser pulse energy over spot size, J/cm²) together with the laser intensity (laser pulse power over spot size, W/cm²). The first defines the laser energy delivered over a certain material volume—considering a constant skin depth as the third spatial dimension—and thus can be a broad measure of the laser effect. For this reason, the ablation threshold of materials is generally expressed in form of fluence [14]. The laser intensity instead, as previously mentioned, defines what is the regime of laser-matter interaction, and thus which physical processes can happen.

Beside the effects related to the change in intensity, the duration of the laser pulse itself has a profound influence on the physics of laser matter interaction. The reason lies in the interplay between the timescales typical of the material response and those associated with the pulse duration, with several significant consequences [15]. The electron dynamics following laser-matter interaction evolves typically fast, in the femtosecond timescales, due to the low electron inertia; the energy transfer to the high inertia ion lattice is instead significantly slower, in the order of nanoseconds. As a consequence, all phenomena related to the ions and lattice phonons—such as heating and heat conduction, thermal effects, melting and evaporation—have analogous characteristic timescales. If the laser pulse is in the nanosecond range, the picture is the one described above, with the laser energy absorption by the electrons followed with transfer to the ion lattice, heating, then eventually melting and evaporation [12]. In the case of shorter (i.e. femtoseconds) laser pulses instead, all the laser energy is delivered to the electrons in a timescale not allowing the energy transfer to the ions. This suprathreshold electron popula-

Chapter 1. Introduction to laser-matter interaction

tion can then promote quite different physical mechanisms, not thermal but electronic in nature [16]. Notable examples are *phase explosion*, in which isochoric heating is followed by rapid adiabatic expansion [17], *nonthermal melting* [18, 19], where the highly energetic electrons promote ion displacements without previous thermalization, and *coulomb explosion* [20], where clusters drained of electrons can disintegrate and accelerate ions due to their mutual electrostatic repulsion. The time evolution of the different processes in the two representative cases—up to material ablation—is shown in Figure 1.3.

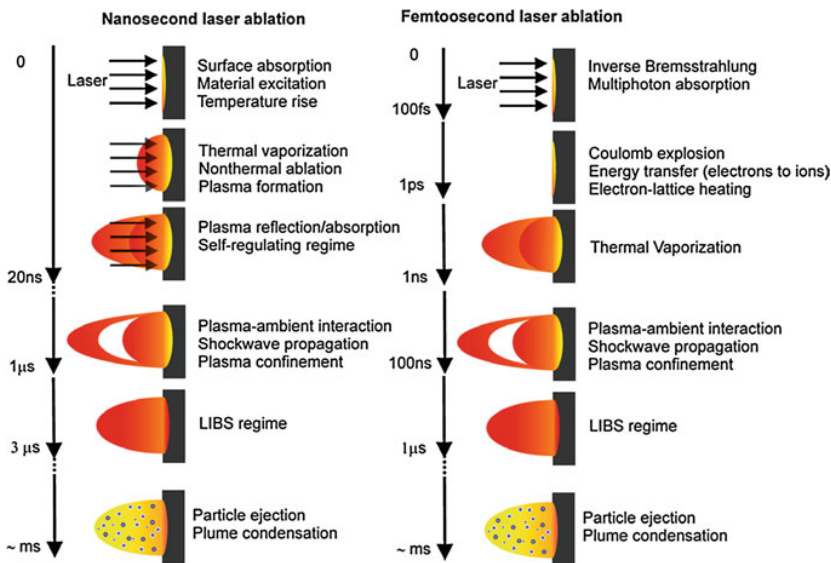


Figure 1.3: Timescales of laser-matter interaction with short and ultrashort pulsed lasers (nanosecond and femtosecond respectively) with the associated processes, from [15].

Another effect worth mentioning—related to the laser pulse duration—is the possible interaction between the laser pulse and the previously ablated material from the target. When a nanosecond laser pulse is considered, this process is an integral part of the laser-matter interaction, since the thermal processes such as heating, melting and evaporation happen in the same timescales as the laser pulse duration [21]. One consequence is that the later parts of the laser pulse interact with a material which is far from the original conditions; another is the screening of the laser pulse by the previously ablated species, along with further ionization and plasma formation. This can lead to the formation of plasma emission for laser intensities even lower than those theoretically required for *prompt* material ionization. On the contrary, the same process cannot happen for ultrashort laser pulses, which are significantly faster than the material dynamics. Nevertheless, it should still

be noted that analogous effects can arise if multiple laser pulses affect the same target area one after another [22]: first, the target material will be modified by the previous pulses, and secondarily—depending also on the laser repetition rate—the following pulse may interact with the ablated species or plasma produced by the previous one. All these considerations are particularly relevant for the laser-driven physical vapour deposition techniques, where the intensity and fluence are sufficiently high to promote ablation and ionization, and thus plasma formation. In those conditions a plasma plume appears from the target surface, an elongated shape composed by ablated species with a bright plasma emission [23].

As previously mentioned, the laser intensity is the main parameter governing the physics of laser-matter interaction. If it is higher than the threshold for ionization (around $10^{13} - 10^{14}$ W/cm²) plasma formation will occur. For even higher intensities, common for the larger laser facilities ($> 10^{19} - 10^{20}$ W/cm²) the leading edge of the pulse can itself promote plasma formation, and therefore the laser-matter interaction will happen mainly as laser-plasma interaction. Higher intensities also promote nonlinear effects, such as higher order harmonic generation and parametric processes, and relativistic effects can become relevant. A brief overview of all these topics will be given in the following.

The laser-driven ionization process can follow two main pathways: *tunnel ionization* and *multi-photon ionization* [24]. The first one concerns the electron emission by quantum tunneling, thanks to the deformation of the atom potential well by the laser electromagnetic field. For this reason, it is the predominant effect for strong laser fields and materials with a lower ionization energy. On the contrary, multi-photon ionization is a classical over-the-barrier process, where nonlinear interaction involving multiple photons can allow electron emission. It is more relevant for lower wavelengths lasers, where the photons are more energetic and a smaller number is required to overcome the potential barrier. Multiple ionizations, and in particular those of core electrons, can follow different mechanisms due to their higher binding potential, such as electron collisions or plasma kinetic effects.

The propagation of a laser pulse in a plasma can be described by its dispersion relation [25]:

$$\omega^2 = \omega_p^2 + k^2 c^2 \tag{1.1}$$

where $\omega_p = \sqrt{4\pi e^2 n_e / m_e}$ is the *electron plasma frequency*, a measure of the electron oscillation happening naturally in a plasma medium, function only of electron density n_e , mass m_e and charge e . Considering the expression of

the linear refractive index as follows:

$$N = \frac{kc}{\omega} = \sqrt{1 - \frac{\omega_p^2}{\omega^2}} \quad (1.2)$$

it is clear that only waves with frequency higher than the plasma frequency can propagate in the plasma, corresponding to a real refractive index in Equation 1.2. In the opposite case, an imaginary N will only allow the existence of exponentially vanishing waves (up to the skin depth $\lambda_{sd} = c/\sqrt{\omega_p^2 - \omega^2}$) in the material. If the same threshold behaviour (corresponding to $\omega = \omega_p$) is expressed as a function of the plasma density instead of plasma frequency, by inverting the definition of ω_p , the resulting density is known as the *critical density*:

$$n_c = \frac{m_e \omega^2}{4\pi e^2} \quad (1.3)$$

If the plasma density $n < n_c$, such as in the case of a laser ionizing a gas, the regime is *underdense* and the electromagnetic wave can propagate through the created plasma. On the contrary, when a laser interacts with solid density matter an *overdense* plasma is often produced, with $n > n_c$. The refractive index is imaginary, thus the pulse is damped exponentially in the skin depth and then mostly reflected backwards. Between the two extremes, the case of a *near-critical* density plasma—where $n \approx n_c$ —is of particular interest: it corresponds to the conditions in which the laser pulse excites the plasma at the frequency of the plasma oscillations themselves, i.e. the textbook description of a resonant interaction. In these conditions the coupling between laser and matter, and thus the process of laser absorption and energy transfer, are strongly enhanced.

In the previous discussion, relativistic effects have not been considered, although they can quickly become relevant for intensities higher than 10^{18} W/cm², due to the relatively low rest mass of the electrons compared to the energy they can gain after laser interaction. Two fundamental parameters are the dimensionless value of the laser field vector potential a and the relativistic Lorentz factor γ , that can be expressed as follows:

$$\mathbf{a} = e\mathbf{A}/m_e c^2, \quad \gamma = \sqrt{1 + a^2} \quad (1.4)$$

As can be seen from the expression of the gamma factor, relativistic effects become important for $a > 1$. A first notable consequence is the increase of the critical density in respect to the non-relativistic case, to $n_{c,rel} = \gamma n_{c,nr}$. Considering the propagation in a classically overdense plasma, the increase in critical density due to relativistic effects can render the plasma underdense, a phenomena known as *relativistic self-induced transparency*. Similar

considerations can apply to the dispersion relation and the refractive index of Equation 1.1 and 1.2, where the term ω_p^2 can be substituted with ω_p^2/γ . The outcome is an increased refractive index for the relativistic plasma where the laser pulse is higher in intensity, in contrast with the surrounding media presenting a lower refractive index. The general picture is analogous to that of an optical fiber, where total internal reflection can take place: the laser will be focused in the plasma channel created by the laser itself, through the well known *relativistic self-focusing* effect [26].

Another important nonlinear effect related to the propagation of high intensity electromagnetic waves in a plasma is the *ponderomotive force*, which is not relativistic in nature and can simply be seen as a form of radiation pressure:

$$\mathbf{F}_p = -\frac{e^2}{4m_e\omega^2}\nabla E^2, \quad \mathbf{F}_{p,rel} = -m_e c^2 \nabla \gamma \quad (1.5)$$

It is inversely proportional to the gradient of the field, acting as a force pushing the electrons from the high field to the low field regions. As can be seen from its classical expression in Equation 1.5, the force is higher on the electrons, due to their lower mass.

After the above discussion, the main electron heating mechanisms in laser-matter and laser-plasma interaction can be briefly summarized. As mentioned, the laser intensity is the main parameter differentiating among the different regimes: for intensities lower than 10^{18} W/cm², *inverse bremsstrahlung* and *resonant absorption* are the predominant phenomena. The first one, more effective at lower electron and laser energies, involves the interaction between an electron and the laser pulse in the presence of the atom electric field. Resonant absorption, instead, is the acceleration of electrons by laser-created plasma waves, driven at the material interface by the oscillating component of the Lorentz force—which should be perpendicular to the material surface, therefore requires a p-polarized pulse. For intensities higher than 10^{18} W/cm², relativistic effects can not be neglected, and two other mechanisms arise: *Brunel effect* and *J × B heating*. In the Brunel effect, also known as *vacuum heating*, the electron are extracted from the material by the electric part of the pulse Lorentz force, and then accelerated back during the subsequent half period. Also in this case, the laser must be p-polarized (and have oblique incidence) to possess a nonzero component of the electric Lorentz force. In the opposite case—s-polarization or normal incidence—it is the (oscillating) magnetic component of the Lorentz force to accelerate electrons, with a similar process than the one described above. If the target is underdense (or notably, becomes underdense due to the relativistic self-induced transparency), a third kind of process can occur: *direct laser acceleration* [27], in which the plasma density modulation in the laser

channel can sustain electric fields than accelerate electrons.

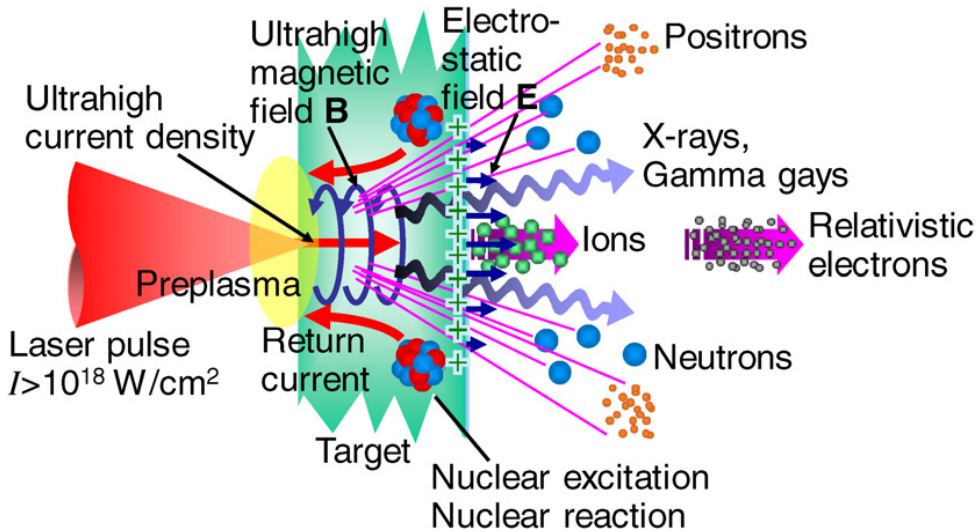


Figure 1.4: Schematic representation of laser-matter interaction in the ultra-high intensity regime, with the multitude of processes that can take place (from [28]).

The phenomena here presented are just some of the fundamentals of laser-matter interaction, and it is already clear how rich and vast the underlying physics is. Considering the effects of the interaction of laser with matter, especially for the case of high energy and high intensity pulses, the emission of particles and radiation are of fundamental relevance. Part of the reason lies in the opportunity to exploit them in applications, as will be discussed in Chapter 2; but just as importantly, the radiation and particles emitted can be detected, and exploited to study the interaction, with the aim to either better understand the physics or (and) develop the applications mentioned above. As represented in Figure 1.4, the interaction of a high intensity laser with matter can promote various processes, also thanks to the high energy provided by the laser. All these processes, beside provoking modification in the target material, stimulate the emission of electrons, ions, clusters, radiation in the form of X and gamma rays, electromagnetic pulses, higher order laser harmonics and light emission from parametric processes. Among those, the acceleration of highly energetic—multi MeV—ions (both from the front and the back of the target, depending on its thickness) is one of the main features of interest for applications [28], together with electron acceleration in underdense plasmas [29]. The reason are the highly intense transient electromagnetic fields that laser-plasma interaction can sustain, allowing particularly high accelerating gradients—impossible to achieve through conventional accelerator technology.

Beside the direct detection of emitted particles, in a laser-plasma interaction experiment the study of the emitted radiation can provide essential information on the plasma properties and their evolution. A notable example are the processes related to the interaction of the laser with a nonlinear medium (such as the plasma created by the laser itself), through which higher order harmonic of the laser can be created. The lowest order process, *second harmonic generation* (SHG) is the most common. Another possibility is the emission of light at specific frequencies due to parametric processes involving both the laser and the plasma, as happens in the *two plasmon decay* (TPD) instability [30,31]. The laser incident photon at ω_0 decays into two plasmons ω_p at half of the laser frequency, which can then interact with the laser itself—in a sum-frequency generation process—to give rise to an emission line at $3/2 \omega_0$. In order to respect energy and momenta conservation, the two plasmon decay can happen when the plasma density is one quarter of the critical density, therefore the detection of the $3/2 \omega_0$ line in an experiment can be exploited to get information on the plasma density profile [32]. Other notable laser-plasma instabilities are *stimulated Raman scattering* (SRS) and *stimulated Brillouin scattering* (SBS) [30,33], both happening in underdense plasmas: in SRS, an electron plasma wave is generated by the resonant interaction of the laser with the plasma, through the action of the ponderomotive force; SBS is a similar process, in which an ion acoustic wave is generated instead of the electron plasma wave. Not all radiation emission due to laser-matter and laser-plasma interaction are equally useful for diagnostics purposes: the fast electromagnetic pulses caused by the fast electron motions inside and outside the target material (EMPs, from MHz to THz in frequencies), can indeed be detrimental for most electronic devices, which therefore require proper shielding. Most research on EMPs is aimed at mitigating the issues they pose for equipment and diagnostics, but there are investigations into their potential application to strong magnetic field generation, charged particle acceleration and focusing or material characterization [34].

CHAPTER 2

Overview of select laser-matter interaction applications

After introducing the field of laser-matter and laser-plasma interaction, this second Chapter is meant to give a general overview of the most relevant potential applications, with a focus on those more closely related to this thesis work. Section 2.1 will discuss laser-driven particle acceleration, focusing on solid targets and ion acceleration. In Section 2.2 Inertial Confinement Fusion (ICF) is addressed. Lastly, Section 2.3 is devoted to the investigation into proton-boron fusion as a mean to produce alpha particles and potentially fusion energy.

2.1 Laser-driven particle acceleration

One of the characteristic features of laser-matter interaction is the emission of highly energetic charged particles, as introduced in the previous Chapter. Thanks to the high energy deposited by the laser, and the subsequent electron dynamics, strong electromagnetic fields can be generated, giving rise to the highest accelerating gradients currently achievable. With proper experimental design, it is possible to exploit this process to accelerate electrons or ions up to considerable energies (in the order of GeV for the former and 1-100

Chapter 2. Overview of select laser-matter interaction applications

MeV for the latter) within a few mm or even μm . The potential for compact particle accelerators is one of the advantages of laser-driven approaches to particle acceleration (in contrast with the state of the art radiofrequency accelerators and synchrotrons machines) together with the peculiar spatial, temporal and energetic properties of the accelerated particle bunches.

Depending whether the aim is to accelerate electrons or ions, the main physical mechanism—and the interaction scheme—are quite different. In the first case, the laser is exploited to drive a longitudinal plasma wave in an underdense plasma, thanks to the ponderomotive force pushing the electrons forward with the leading edge and backwards with the trailing edge. If the pulse duration is matched with the period of the plasma oscillation, continuous electron acceleration is possible, in which an electron bunch "rides" the plasma wave created by the laser: the process is known as *Laser Wakefield Acceleration* [35, 36]. Considering the requirements for the plasma density, which should allow laser propagation, underdense gas jet or liquid target are generally exploited. Another possibility are plasma capillaries, where the acceleration process driven by the laser is decoupled from the creation of the plasma itself, allowing longer accelerating plasma channels and better control of the process [37].

Ion acceleration on the contrary is most efficient in the interaction of a laser with a solid density target, where ion emission from the site of laser-matter interaction is a common occurrence. More interestingly, as evidenced by the first experiments performed in the 2000s with ultrashort (fs/ps duration) high intensity ($>10^{18}$ W/cm²) lasers [38–40], the use of thin micrometric targets led to ion emission from the rear surface of the target, a region where no direct interaction with the laser pulse took place. This initially surprising behaviour, along with the peculiar properties of the accelerated ions (such as high energy, ultrashort bunch duration, wide energy spectrum and high ion density per bunch), sparked the research interest into understanding the underlying physical mechanisms. While the first hypothesis was related to the acceleration of ions at the front of the target, followed by transport toward the backside and subsequent emission, the experimental evidence soon consolidated the opposite picture: the ions are actually accelerated from the rear side of the target in a process known as *Target Normal Sheath Acceleration* (TNSA) [28, 41].

As outlined in Figure 2.1, the interaction of the laser with the solid target, which is overdense, leads to plasma formation and electron acceleration by the mechanisms mentioned in the previous Chapter, such as Brunel effect and $J \times B$ heating. The highly energetic electrons can then travel through the target, balanced by a return current of cold electrons. Upon reaching the rear side of the target, the electrons are emitted and form a sheath electrostatic

2.1. Laser-driven particle acceleration

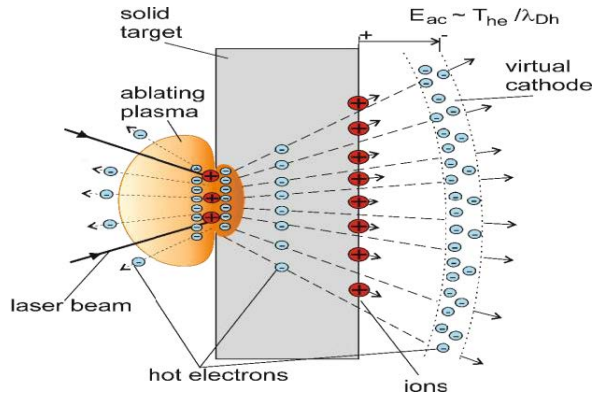


Figure 2.1: Schematic of the target normal sheath acceleration process (TNSA), from [42].

field between themselves and the now positively charged target. The sheath size can be estimated with the electron Debye length $\lambda_D = \sqrt{T/4\pi n_e e^2}$ (i.e. the amplitude of the characteristic electron oscillations due to their thermal energy) and the corresponding electric field can reach values as high as TV/m. Such a high electrostatic force can then promote the ionization and subsequent acceleration of the atoms present on the back surface of the target. The process is more efficient on lightly bound impurity ions present as contaminant on the rear target surface, such as hydrogen, therefore protons are the main ions accelerated in TNSA. At the same time, this does not exclude the simultaneous presence of other ions with the same origin (i.e. surface impurities), such as carbon, or even ions from the target material. If the aim is to increase the efficiency in heavy ion acceleration, the proton (and eventually carbon) component should be suppressed: various techniques to minimize the surface contaminants can be exploited, from Joule heating to laser ablation or sputtering [43].

As a consequence of the TNSA mechanism, the accelerated ions present unique properties: they show a wide energy spectrum, decreasing exponentially with a cutoff at high energies, consequence of the gradual reduction of the sheath field as a larger number of ions are accelerated. In Figure 2.2 an example of a representative experimental proton energy spectrum is shown, with the proton energy cutoff at around 6 MeV. Due to the fast acceleration of initially cold ions from a limited region of the target, other notable characteristics are the ion bunch short duration, high ion density and ultralow emittance. The ions are accelerated along the normal to the rear target surface, with a divergence angle of 20-60 degrees [41].

For these reasons, they are of interest for a wide range of application in different fields: thanks to the short bunch duration and exceptional emittance

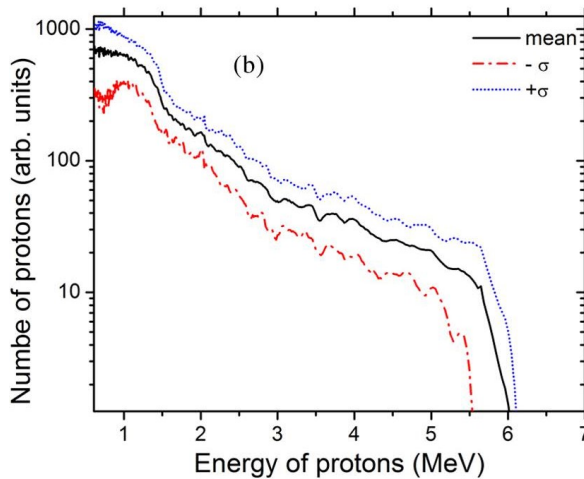


Figure 2.2: Typical proton spectrum in laser-driven ion acceleration, averaged over many laser shots (from [44]).

properties, laser-driven ions can be exploited in imaging applications, such as radiography and probing of plasma and its dynamics both in terms of density and electromagnetic fields [45–47]. In the medical field, the laser-driven proton beams could be exploited to produce radioisotope useful for nuclear medicine diagnostics, such as PET, with the main advantage being related to the potential compactness of laser-driven accelerators [48, 49]. The main drawback are the high average currents required, implying the necessity of a high repetition rate operation of the laser-driven accelerator, which is far from obvious. Another promising application is hadrontherapy, where energetic ions can deliver lethal dose to cancer cells with high precision and spare surrounding healthy tissues, thanks to the localized energy deposition characteristic of heavy charged particles (Bragg peak). Current laser-driven ion sources do not yet meet the requirements for therapeutic purposes (low energy spread and selectable energy in the 60–250 MeV range), but the demonstrated enhancements in radiobiological efficiency due to the ultra-high dose rate (i.e. FLASH effect) is particularly promising [50, 51]. The accelerated ions can also be exploited to promote nuclear reactions, both for their inherent interest (i.e. the study of nuclear reaction in a plasma environment [52, 53]) or to exploit the reaction products as secondary sources. Connected to the first aim are laboratory astrophysics studies [54, 55] and investigation into warm dense matter [56, 57], that exploit the high amount of energy delivered by the laser to reach extreme matter conditions of astrophysical relevance. Concerning the secondary sources, laser-driven neutron production garners the most interest, for its ability to produce short bursts of

neutrons up to 100 MeV in energy by exploiting a nuclear reaction in a converter material, generally in a pitcher-catcher configuration [58, 59]. Laser-driven fusion (i.e. inertial confinement fusion, ICF) and proton-boron fusion, while belonging to the topic of nuclear reaction promoted by lasers, are central to this thesis work and will be treated in detail in Section 2.2 and 2.3 respectively. Many of the radiation sources mentioned above (and in the previous discussion), from protons and electrons to neutrons and X-rays, can effectively be exploited as probes in material science techniques, from proton, neutron or X-ray radiography [58, 60, 61] to spectral techniques such as PIXE/PIGE (*Particle Induced X-ray Emission/Gamma ray Emission*) [62, 63] or EDXS (*Energy Dispersive X-ray Spectroscopy*) [64]. Beside the potential compactness of the setup, one great advantage would be the possibility to perform various analysis simultaneously, reaching a complete characterization of the sample within a single laser shot [61, 64, 65].

Despite TNSA being the predominant acceleration mechanism, it is worthwhile to mention the existence of other acceleration schemes, which start to become relevant at higher intensity conditions and/or specific target configurations. One is related to *Coulomb explosion*, already mentioned in Chapter 1 as one of the processes characteristic of laser-matter interaction with nanoparticles and clusters: by exploiting the efficiency of Coulomb explosion on a nanometric thick high Z target, it is possible to easily accelerate heavy ions and boost the high energy component of the spectrum, up to 200 MeV [66]. A second relevant mechanism, also related to the use of ultrathin targets and extremely high intensities, is *Radiation Pressure Acceleration* (RPA), in which the laser pulse can directly propel electrons forward—with high energies—after ionization of the thin target. While in experimental scenarios at ultrahigh intensity RPA and TNSA often coexist, the enhancement of high energy ion component due to RPA has been demonstrated. Indeed, the highest proton energies achieved in a laser-driven acceleration scheme (close to 100 MeV) can be attributed to this regime [67]. The RPA mechanism with thin targets is also known as *Light Sail* regime, in contrast with the behaviour of thick solid targets under similar laser conditions: in that case, the laser ponderomotive pressure pushes the electrons into the bulk of the target, creating an electrostatic shockwave that can propagate and accelerate ions. This is the *Hole Boring* (HB) regime of RPA, Known also as *Collisionless Shock Acceleration* [28].

It should be clear from the above discussion the importance of the target in the design of a laser-driven acceleration experiment, even more so considering the advancements—and limitations—in laser technology and the demanding requirements of the most promising applications. This is even more crucial for the design and development of compact laser-driven radia-

Chapter 2. Overview of select laser-matter interaction applications

tion sources, where stringent bounds come from the maximum performances achievable with tabletop laser systems. There is ample literature into the study of how the laser and target properties influence the acceleration process, and how they can be exploited to optimize it or tune the properties of the accelerated ions. As already partially highlighted, the thickness of the target is a key parameter: the use of thinner targets can be advantageous if coupled with ultrahigh intensity lasers, to leverage the advantage of the RPA light sail regime, but even in TNSA they allow a more efficient transport of the hot electron to the back of the target, and therefore better accelerating performances. As shown from Figure 2.3a, this holds in general, albeit with a couple of important caveats: considering thinner and thinner targets, the acceleration performances will increase only down to a certain thickness, for which the laser pulse starts to destroy (i.e. ionize) the whole target before the sheath field can be established. For the TNSA mechanism to efficiently take place, the rear surface of the target should still be solid—and as unperturbed as possible—since the presence of a plasma there will decrease the sheath field and hinder ion acceleration [41].

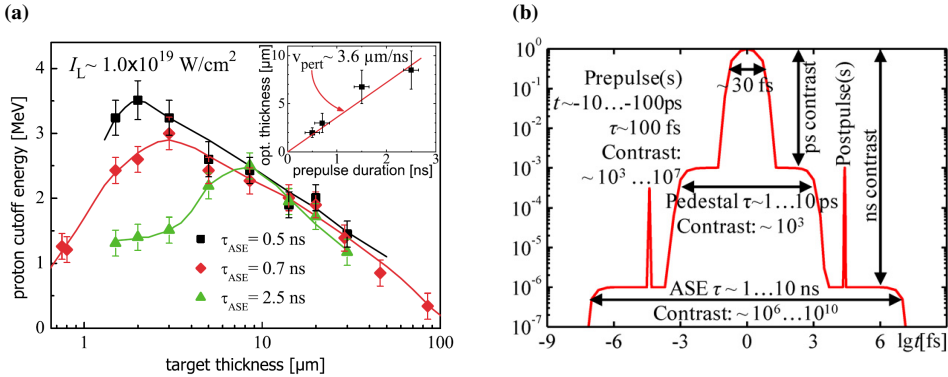


Figure 2.3: (a) Optimum target thickness for different laser prepulse durations, using the maximum proton energy as comparison parameter (from [68]); (b) Schematic representation of a high-intensity laser pulse temporal profile, with the most relevant pre- and post-pulses (from [28]).

Related to these considerations, there is one more laser parameter which must be considered, and is one of the main figure of merits of laser systems in high-intensity laser-matter interaction experiments: the *contrast ratio*. As a consequence of the physics of laser emission and the technology of high intensity amplifiers, even in ultrashort pulses (i.e. tens of femtoseconds of FWHM) various other features are generally present in the temporal shape of the pulse, both before and after the main pulse. These are ex-

emplified in Figure 2.3b: a picosecond pedestal caused by uncompensated higher order dispersion, a prepulse anticipating the main pulse originating from non-linearities in the CPA process and a nanosecond background due to Amplified Spontaneous Emission (ASE). The laser contrast is simply the ratio in intensity between these other features and the peak intensity of the pulse. Considering the laser interaction with a solid target, the presence of even a small fraction of the maximum laser intensity preceding the main pulse—especially in the case of ultra-high intensity lasers—can easily lead to plasma formation in the target or even destroy it before the main pulse can interact with it. As a consequence, the optimum (minimum) thickness of the target that leads to the highest acceleration efficiency is strongly dependent on the laser contrast (clearly shown in Figure 2.3a): a higher contrast ratio allows to exploit thinner targets and stronger TNSA accelerating fields, while on the contrary a lower contrast leads to heating and plasma creation on the rear of the target inhibiting the acceleration [68, 69]. As a last remark, it should be noted that purposely exploiting a low contrast laser to create a plasma in front of the target, while at the same time using thick targets to avoid modification on the rear side, can be successfully exploited to increase the laser absorption efficiency [70]. There are different measures that can be taken to increase the laser contrast, either at the origin—by specific design choices in the laser seeding and amplification processes (e.g. double CPA setup with stepwise nonlinear cleaning of the laser pulse through temporal filtering, to improve seed signal-to-noise ratio and thus reduce ASE impact [71])—or by "post-production" cleaning of the ultrashort high-intensity pulse. Among the latter, *plasma mirrors* can lead to the greater increase in laser contrast, thanks to a simple working scheme: the laser is sent on a material that is not reflective under normal conditions, but becomes so after the laser prepulse has ionized it, reflecting only the main pulse while discarding all previous intensity modulations [72].

Many different advanced target designs have been proposed, often with aims going beyond the simple enhancement of the number/energy of accelerated ions: mass-limited targets [73], with micrometric transverse size able to confine the hot electron population and thus enhance and stabilize the sheath field; shaped targets (curved or conical) [74] to exploit potential focusing effects, such as those consequence of the proton emission normal to the target surface typical of TNSA; solid target with an added micro-helical coil, for increased focusing and post-acceleration driven by the magnetic field inside the coil (induced by the hot electron themselves) [75]; micro- and nano-structured targets, to induce modulation in the ion beam or increase the laser absorption efficiency [76, 77]; and with similar aims double-layer targets, composed by a thin target with a near-critical density layer on the

laser-facing side [78, 79]. This last kind of targets, due to their specific interest in this thesis work, will be the subject of a more in depth discussion in Chapter 3 and Section 3.3.

2.2 Inertial Confinement Fusion (ICF)

In light of the ever-growing energy demands of the present society, together with the issues originating from the overuse of fossil fuels (i.e. pollution and climate change), the study of alternative energy sources is of great relevance. In this context, nuclear fusion is one of the most investigated subjects, thanks to its potential to deliver vast amounts of energy with minimal environmental impact and limited safety concerns [80]. In order to overcome the electrostatic repulsion and allow the onset of the (strongly exothermic) fusion reactions, energy must be supplied to the light nuclei used as fuel. The energy produced by the first reactions can then in part be exploited to maintain the required conditions, and promote further fusion reactions throughout the fuel material. It should be noted that the temperature needed is in the order of several hundred million degrees, conditions in which electrons cannot remain bound and matter is in the plasma state.

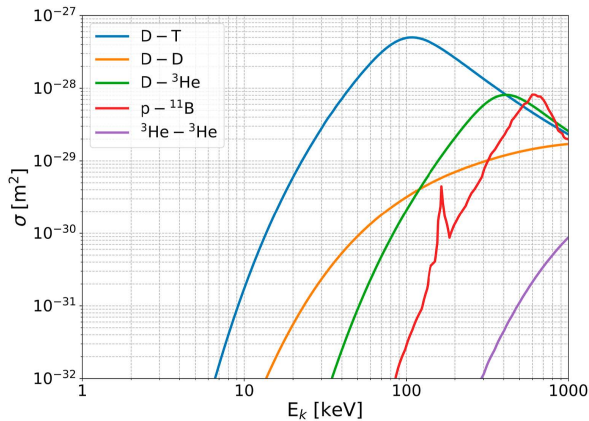
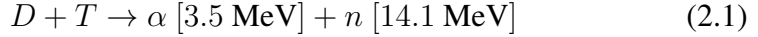


Figure 2.4: Fusion cross sections for various reactions of interest for energy production (from [81]).

One of the—arguably many—challenging aspects in the quest to exploit nuclear fusion for energy production is related to the extreme matter conditions required, due also to the generally low cross section of the reactions. Figure 2.4 shows the cross section for different potential fuel choices, highlighting the advantages in term of higher cross section across the whole range (and particularly relevant at moderate energies) of the deuterium-tritium (D-T) fusion reaction. For this reason, the great majority of fusion research is

aiming to use a deuterium-tritium fuel [80, 81]. The reaction, leading to the production of an alpha particle and a neutron, releases 17.6 MeV of energy overall, shared among the reaction products according to their mass:



Among the two, the positively charged alpha particles strongly interact with the surrounding plasma, depositing their energy in an area close to where the fusion reaction took place, while the neutrons can escape (and after moderation, their energy can potentially be harvested for electric energy production). Therefore the alpha particle can be responsible for keeping the hot plasma in the conditions required for fusion reactions to occur. In general, for the process to sustain itself, the alpha particle heating should be able to overcome the energy losses, mainly in the form of bremsstrahlung radiation and heat conduction. This condition, when the burning plasma can independently sustain itself from an energetic point of view, is known as *ignition*. It can be exemplified by the *Lawson criterion*, i.e. the combined conditions of plasma density, temperature and confinement time allowing a sustained burning plasma [82]: $nT\tau_e \geq 3 \cdot 10^{21} \text{ KeV s m}^{-3}$.

In order to meet this requirement, two avenues of research have been developed, with opposite approaches: on one side *Magnetic Confinement Fusion* (MCF) [83], where the aim is to confine a relatively low density plasma for a significantly long time, exploiting intense magnetic fields in devices such as tokamaks and stellarators. The European ITER project is a prime example of the former [84]. On the other hand, one can completely forego plasma confinement and rely only on the fuel inertia—strongly reducing the confinement time—by reaching substantially higher plasma densities to compensate, per the Lawson criterion. This is the basic idea of the *Inertial Confinement Fusion* (ICF) approach, where small capsules containing deuterium and tritium are compressed to the required conditions by powerful high-energy lasers [85].

The fuel capsules are deuterium-tritium shells, filled with D-T gas: the configuration is able to withstand the strong and fast compression needed to reach ignition, which would not be feasible for a solid material. On the outer side of the capsule, a thin external layer called *ablator* is present, with the purpose to absorb the laser energy and convert it to kinetic energy—that is, pellet compression: as the ablator is emitted in the outward direction after laser interaction, the rest of the capsule is compressed by the rocket effect. The evolution of the pellet from initial condition to ignition is schematically depicted in the lower panels of Figure 2.5: the external ablator layer absorbs the laser energy, forms a plasma and drives pellet compression; when the compression is maximum, the conditions of temperature and pressure

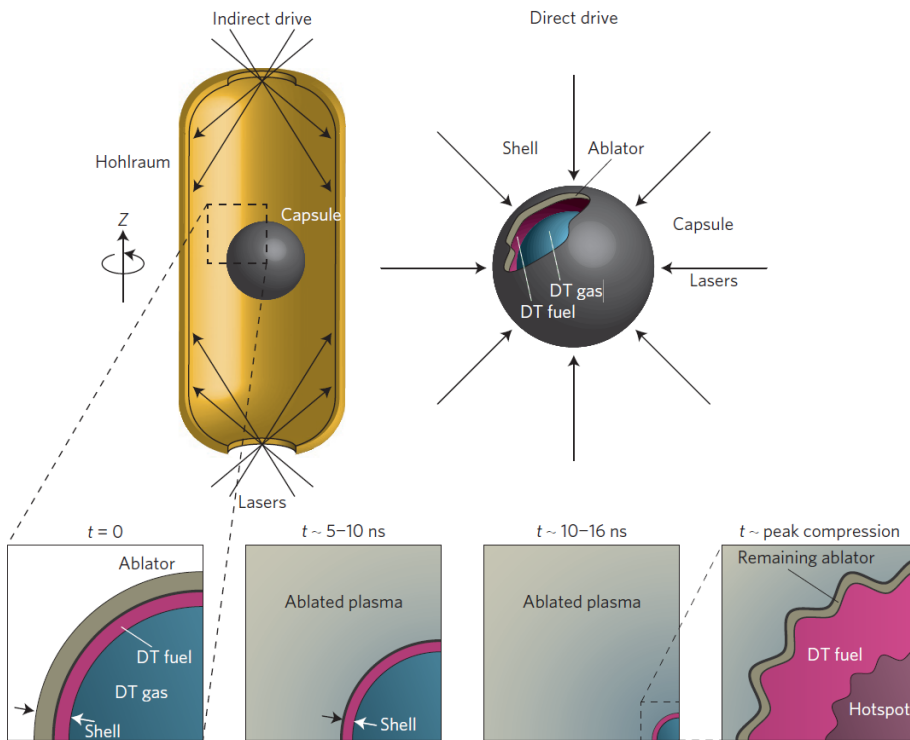


Figure 2.5: Schematic representation of the two ICF schemes, indirect drive (upper left) and direct drive (upper right), together with the phases of capsule implosion in the bottom row (from [85]).

in the center of the compressed capsule (the so-called *hotspot*) lead to the onset of fusion reactions. If the ignition conditions are satisfied, the reaction can self-sustain thanks to alpha heating, creating a burning plasma wave that propagates through the rest of the D-T fuel, before the inevitable expansion sets in and the fuel disintegrates. Despite the simple concept, the actual realization of laser compression and hotspot ignition is exceedingly complex: on one side, thermodynamic considerations lead to strong constraints on the laser driver temporal shape, since early heating of the fuel material hinders further compression. The laser driver, over the duration of a few nanoseconds, sends subsequent shocks into the capsule, with the aim to strike a balance between having a fast and high compression and avoiding instabilities [85]. Indeed, stringent geometrical constraints are imposed by the symmetry requirements of the implosion process, both for what concerns the laser drivers and the capsule itself. Hydrodynamic instabilities such as Rayleigh-Taylor are prone to take place due to the capsule design—lower density gas inside a solid density shell—and can be especially detrimental:

any defect on the ablator surface or laser driver inhomogeneity can be amplified during compression, and colder higher density fuel from the shell (or ablator material) can end up towards the capsule center, inhibiting hotspot creation [86]. This kind of issues are more prominent in the case of *direct drive* ICF [87], where multiple laser beams are directly focused on the pellet from many directions: due to the finite number of laser beams—if very large, in the order of one hundred—a completely uniform laser energy delivery over the ablator surface is not feasible. For this very reason, a second scheme has been investigated, involving the use of a high-Z cavity around the fuel pellet: *indirect drive* ICF [88]. Here the lasers are focused on the inner walls of a cavity (called *hohlraum*) to generate X-rays, and the superposition of many X-rays modes in the cavity—with proper design—can significantly increase the uniformity of capsule ablation. The downside is the limited efficiency of the X-ray conversion process, factor that becomes relevant in relation to the final aim of producing more energy than what is consumed. Both approaches mentioned are depicted in Figure 2.5.

Considering the multiple challenging aspects of achieving hotspot ignition discussed above, the possibility to exploit advanced ignition schemes is also being researched: by accepting a more complicated interaction scheme, it is possible to decouple the compression and ignition phases, with a significant reduction in the requirements for both. This can be done by exploiting an external driver to heat the fuel while at peak compression, igniting fusion reaction. One possibility is *fast ignition* [89], where laser-accelerated particle beams such as electrons or ions—with mechanisms analogous to those discussed in Section 2.1—are employed. As a matter of fact, the idea originated from the development of ultrafast lasers in the last decades, allowing the generation of ultrashort and energetic bursts of charged particles in coincidence with the time of maximum capsule compression. An important added benefit of the loosened compression requirements are the higher achievable gains: much larger capsules can be compressed (at lower implosion velocities) with a correspondingly higher fuel content and thus energy released. A second kind of scheme being investigated, with similar advantages and aims, is *shock ignition* [90, 91]. In this case, a strong final shock is launched in the compressed capsule by a final laser power spike. After colliding with the original shock moving outward from the compressed fuel core, a much stronger gigabar shock is generated, triggering ignition. Fast electrons driven by the laser (and originating from laser-plasma instabilities) could also increase the shock pressure, if they interact with a sufficiently dense fuel and are stopped near the surface of the capsule (limiting the detrimental heating effects).

In the last years, milestone results have been achieved at the National

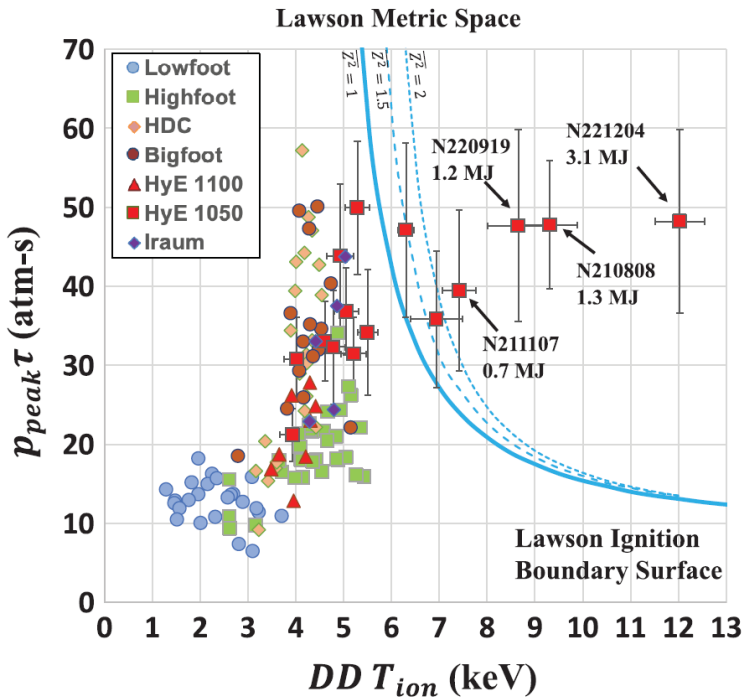


Figure 2.6: Progression toward ignition in indirect drive ICF experiments at the NIF from the 2010s to the present day, showing the substantial improvements in peak pressure, burn duration and hotspot temperature, together with the breakthrough achievements of both ignition and target gain exceeding unity in multiple recent experiments (from [92]).

Ignition Facility (NIF) [10] in the United States: as shown in Figure 2.6, from the first D-T experiments in 2011 the implosion performance was continuously improved, leading to breaking the ignition threshold in 2021 [93]. Further optimization of the experimental configuration resulted in achieving a target gain (i.e. fusion energy generated over total laser energy provided to the capsule) greater than unity, from 1.5 to 1.9 [92]. As demonstrated by the many decades elapsed between first NIF experiments and the achievement of ignition (the NIF was in operation well before the campaigns exploiting D-T capsules), many advancements in physics understanding and design improvements in all the different components were the origin for the final breakthrough results. On the target side, a gold-lined depleted uranium hohlraum filled with He gas gave the best results for homogeneous X-ray emission; a D-T ice capsule filled with D-T gas was exploited, with a nanocrystalline HDC (high density carbon) ablator specifically designed to avoid surface defects and inhomogeneities. A tungsten-enriched layer was also buried in the HDC ablator, to shield the X-rays and avoid fuel preheat-

ing. On the laser side, a modified high-foot pulse, with lower peak power and the same energy distributed over a longer time, was found to be beneficial for better compression and reduced instabilities. This has led to difficulties in laser propagation, due to screening by the wall plasma formation inside the hohlraum, solved by means of cross-beam energy transfer [92]. In conclusion, the promising results sparked new interest in ICF as promising mean to achieve fusion energy in the future, among which the proposal to establish a European ICF programme and a greater involvement by the European laser-matter interaction scientific community [94]. Among the most critical issues still to be addressed, reduction of instabilities and total efficiency increase are key to eventually demonstrate viable electric energy production. Thus, advancements in laser technology, laser-matter coupling, capsule design and experimental scheme are all to be pursued.

2.3 Proton-Boron fusion

Between the reactions of potential interest for nuclear fusion applications, deuterium-tritium is by far the most investigated, thanks to its comparably high cross section especially at low temperatures (blue curve in Figure 2.4). Nevertheless, D-T fusion is not without drawbacks, starting from the difficulties in tritium supply (being a short-lived radioactive isotope it has to be produced through nuclear reaction) together with the radioprotection issues stemming from the high mobility and thus difficult handling of tritium. At the same time the neutrons produced by the D-T reaction, while helpful in energy removal from the plasma, induce activation and thus added radioactivity in the surrounding reactor material, and even more importantly lead to radiation damages and potential functional/structural concerns. The proton-boron nuclear reaction is an interesting alternative in this regard, where a proton and a nucleus of ^{11}B combine emitting 8.7 MeV of energy and 3 alpha particles:



The alphas present a wide energy spectrum, with a main peak around 4 MeV and a secondary one close to 1 MeV, with the possibility of a secondary channel at higher energies (6-10 MeV) [95]. Since no neutrons are emitted as products, the related issues are avoided, and in addition both fuel components are abundantly present in nature (the isotopic abundance of ^{11}B in natural boron is 80.3%, the rest being ^{10}B). Despite these desirable features, the cross-section is significantly lower than D-T, even in the regions interested by nuclear resonances around 150 and 600 KeV (red curve in Figure 2.4). For this reason, the potential of the proton-boron reaction for nuclear

Chapter 2. Overview of select laser-matter interaction applications

fusion energy production was first evaluated negatively [96]. This conclusion was obtained considering a thermonuclear approach, such as MCF or conventional ICF, where the fuel is heated until its thermal energy is sufficient to induce self-sustaining fusion reactions (i.e. ignition). Nevertheless, the advent of ultrashort high intensity laser has rekindled the interest in the reaction, as the disadvantages of a lower cross section can be mitigated by a laser-driven approach, where suprathermal conditions can be achieved for part of the ion population. This can happen directly in the plasma state after laser interaction, or in beam-based approaches where a beam of highly energetic laser-accelerated protons interacts with a solid boron target [97]. Energy applications remain challenging, considering the fraction of the fuel undergoing fusion reactions in these kinds of approaches is rather limited, and the scientific maturity of proton-boron fusion research is presently far from D-T fusion research. Despite this, among the many private companies and startup active in the field of fusion energy production, some have opted for p-B fuel [81,98] and scientific interest in the field is increasing.

It is also important to note that energy production is not the only potential application of the proton-boron fusion reaction, and indeed a large portion of the present research effort is focused on the alpha particle beams emitted as a result of the fusion process, with favorable properties for ion beams applications: high current, MeV energy, and potentially high directionality with proper interaction design [99]. One other promising application related to proton-boron fusion is Proton Boron Capture Therapy (PBCT) [100], in which a conventional hadrontherapy setup using protons is coupled with a boron-containing compound. Thanks to the higher LET (Linear Energy Transfer) of the heavier alpha particles, the radiobiological efficiency of the treatment can be enhanced [101]. The use of laser driven protons, in order to exploit PBCT along with the FLASH effect, is a promising research direction for the future [102].

In the last years multiple laser-driven proton-boron fusion experiments have been performed, showing a promising increase in alpha particle yields (Figure 2.7). Different interaction configurations, target compositions and laser parameters are being explored, in order to find the most suitable combination. Two main interaction schemes are equally gathering interest: the “*in-target*” approach and the “*pitcher-catcher*” configuration. The former is quite straightforward, involving a target containing both boron and hydrogen (to provide the protons) on which a high-intensity laser pulse is focused to create a plasma, accelerate the ions and trigger fusion reactions [99]. The latter aims to separate the process in two stages: first the protons are accelerated by the use of a high intensity laser and a suitable first target (*pitcher*), and then a boron-containing target (*catcher*) is placed to collect the protons

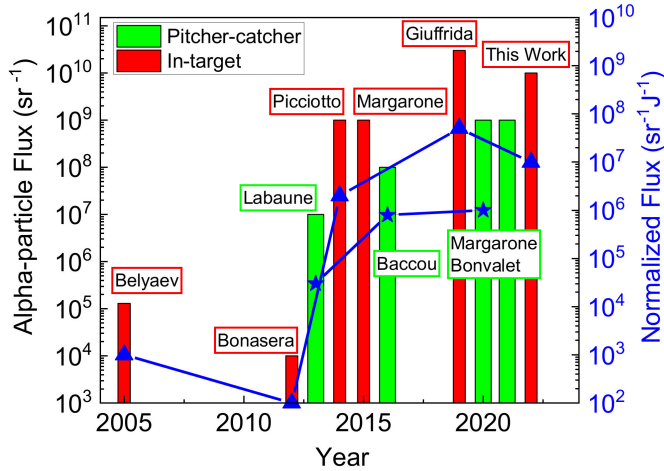


Figure 2.7: Advancements in alpha particle yields from multiple proton-boron fusion experiments in the last years (from [97]). In red the data related to the "in-target" scheme, while in green the results obtained in "pitcher-catcher" configuration experiments.

and enable the fusion reactions [103]. As shown in Figure 2.7, the in-target configuration is the one currently more successful in the number of alpha particles produced.

An interesting variation of the pitcher-catcher scheme is shown in Figure 2.8: here a lower intensity nanosecond laser is exploited to irradiate the boron catcher target, creating a boron plasma. Compared with just the solid boron catcher, a significant enhancement of proton-boron reactions was measured if the reaction happened in plasma [103]. The effect was attributed to multiple factors, such as a greater penetration of the protons inside the plasma in respect to a solid density material, no proton energy lost to ionization and the potential beneficial effect due to the TNSA electrons co-moving with the protons. Analogous beneficial effects in performing the reaction in plasma conditions are also observed for in-target configuration experiments [99, 104], despite the conditions (and thus proposed explanations) being different. In contrast with the TNSA ion acceleration from the back of a thin target, here the aim is to provide energy to the ions on the front of the (thick) target; a longer and generally more energetic laser pulse (nanosecond or picosecond in duration) is exploited, which creates a plasma and accelerates ions back toward the laser side. The mechanisms proposed to explain the high alpha particle yield include laser self-focusing and high spatial and temporal superposition of the proton and boron ions accelerated inside the plasma [99]. Another interesting observation is the enhancement of alpha particle energy due to the laser-created electric field on the front side of the

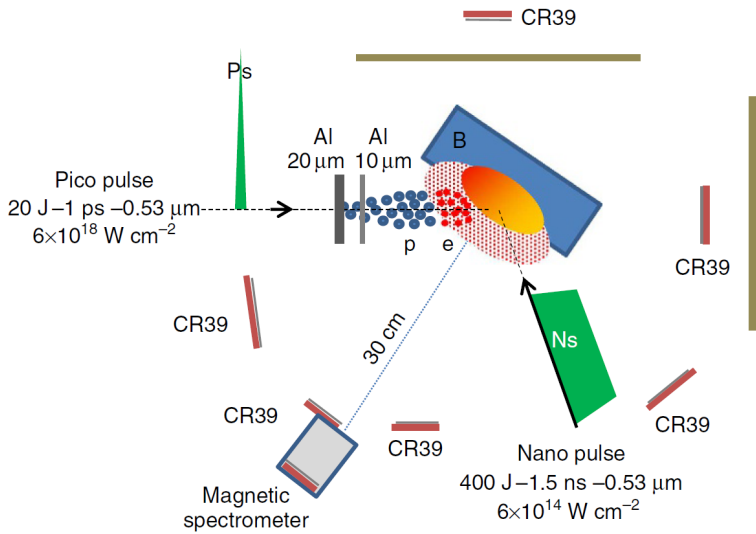


Figure 2.8: Scheme of a pitcher-catcher proton-boron fusion experiment, in which a second laser of longer duration is focused on the boron target to create a plasma (from [103]).

target, in a TNSA-like mechanism [104].

The design of an optimal target, especially for the in-target configuration, is certainly not straightforward: solid targets are mostly exploited, with different ways to incorporate both boron and hydrogen. The simplest approach is to rely on surface contaminant and material impurities, such as the commonly used Boron nitride (BN) targets, already providing satisfactorily results [97, 104]. Otherwise specifically designed targets can be exploited, such as silicon targets enriched in boron and hydrogen through thermal annealing and ion implantation [99] or boron nitride targets with a polymeric CH layer deposited by plasma-assisted physical vapour deposition [105]. In conclusion, in the field of proton-boron fusion—and its targetry in particular—there is space for great improvements, in the quest for fusion energy production and other alpha particles applications.

CHAPTER 3

Nanostructured materials and nanofoams

In this Chapter nanostructured materials will be introduced, with a focus on low-density porous nanofoams and their promising applications in the field of laser-matter interaction. Section 3.1 will describe the materials together with their outstanding properties, Section 3.2 will give an overview on the most common synthesis methods to obtain such unconventional structures, and lastly their relevance to laser-matter interaction is outlined in Section 3.3.

3.1 Nanostructured materials morphology and properties

Nanoscience and nanotechnology are fields of science showing great promise in relation to many different applications, with an ever-increasing ability to probe, design and exploit materials at the micro and nanoscale [106]. The advantages of such an approach are twofold: on one side, the ability to finely control the structure and composition of the material, and consequently its physical, chemical and biological properties (e.g. melting point, wettability, electrical and thermal conductivity, catalytic activity, light absorption and scattering, density, biotoxicity). On the other, thanks to quantum confinement effects, significant changes in material properties can happen in the transition from bulk to nanoscale materials, depending on their con-

finement size. By exploiting this effect, it is possible to explore ranges of material properties beyond what is otherwise achievable with standard techniques [107, 108].

Considering the wide variety of material properties that can be controlled by nanostructuring, their application in the most diverse field of science is not surprising. At the same time, the definition of nanostructured materials is rather broad, encompassing any material in which nanometer-sized components are present and influence its properties and functionality. A first category are bulk materials with nanometric grain size (nanocrystalline) or with nanoscale variations in composition, thanks to which the material properties—e.g. mechanical or electrical—can be tuned as desired [109, 110]. Particularly interesting is also their application in the development of materials resistant to radiation damage: nanostructured materials can have a considerably high concentration of defect sinks, which are able to strongly reduce the detrimental effects of radiation damage [111]. Another possibility are nanoparticles or nanoclusters decorating the surface of a substrate material, able to modify the interface properties. Applications commonly deal with optical properties and light interaction, such as photon detection and plasmonics [112, 113]. A similar approach consists in the nanoscale modification of the material surface to obtain a specific functionalization, either in terms of the aforementioned optical properties or tuning the surface hydrophobic/hydrophilic behaviour [114]. Both approaches are also interesting for applications in the biomedical field, where nanomaterials have the potential to promote the bio-functionality and biocompatibility of interfaces, thanks to their tunable properties at the micro and nanoscale [115, 116].

Going toward greater morphological complexity, the last category of nanostructured materials are films and coatings, with a thickness ranging from tens of nanometers to micrometers, and the most varied morphologies, both ordered and disordered (some examples are depicted in Figure 3.1). Considering their general structure, composed by distinct solid-density features (e.g. nanoparticles, nanorods, nanotubes, nanorods) with a nonuniform arrangement in space, they present a certain degree of porosity and thus a lower density than bulk materials. Another outstanding property consequence of their morphology—and one of the main reasons for their widespread appeal—is the substantial specific surface area (and area-to-volume ratio) owing to the nanoporosity of the structures. Any application in which there is a surface interaction (or reaction) between the material and the surrounding environment can strongly benefit from the approach, such as sensor technology [121], gas sensing [122] or catalysis [123–125]. Similarly, nanostructured materials show great promise in the electrochemical field, where they could be exploited in the development of the next generation batteries

3.1. Nanostructured materials morphology and properties

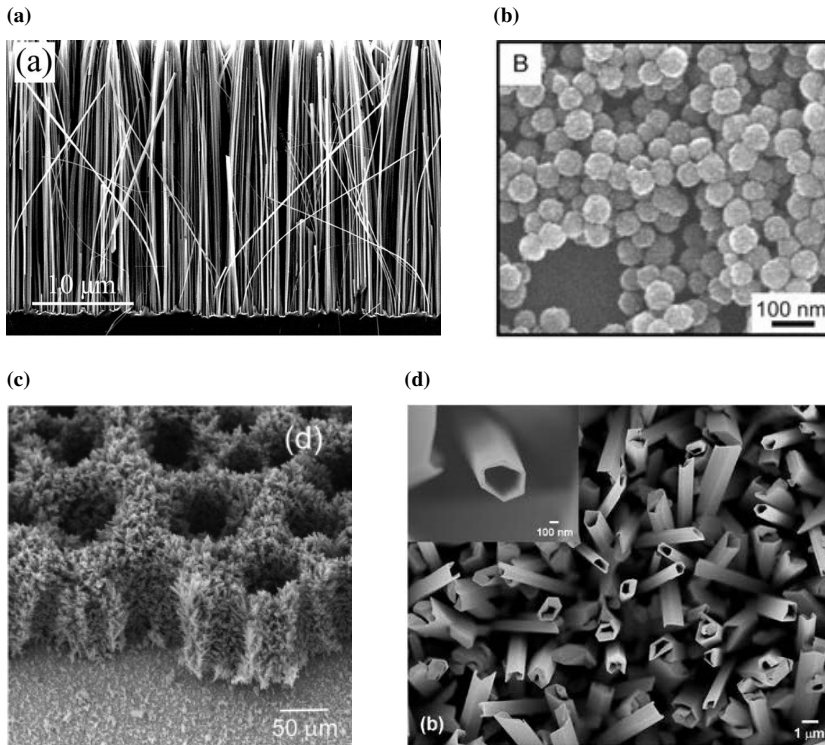


Figure 3.1: Examples of nanostructured material morphology: (a) Silicon ordered nanowires [117]; (b) ZnS porous nanoparticles [118]; (c) Copper foam with nanostructured walls [119] (d) Tellurium nanotubes [120].

and supercapacitors, to satisfy the ever increasing need for efficient energy conversion and storage devices [122, 126].

One specific class of morphologies are micro- and nano-structured foams, gathering particular interest in the high-intensity laser-matter interaction community, for their favorable laser energy absorption properties (the reasons will be explored in more detail in Section 3.3). They are disordered high porosity material, with alternating solid structures and voids. The solid structures may be membranes, wires or nanoparticles of varying dimensions and composition, as shown in the examples of Figure 3.2; this is largely dependent on the synthesis method, as will be discussed in the next Section. Beside having similar properties to other classes of nanostructured materials—making them attractive for the aforementioned electrochemical and catalytic applications—they can reach really low density values, down to a few mg/cm^3 . This is achieved by reducing the size and/or the quantity of solid components, in favour of a void fraction as high as 99.9%, together

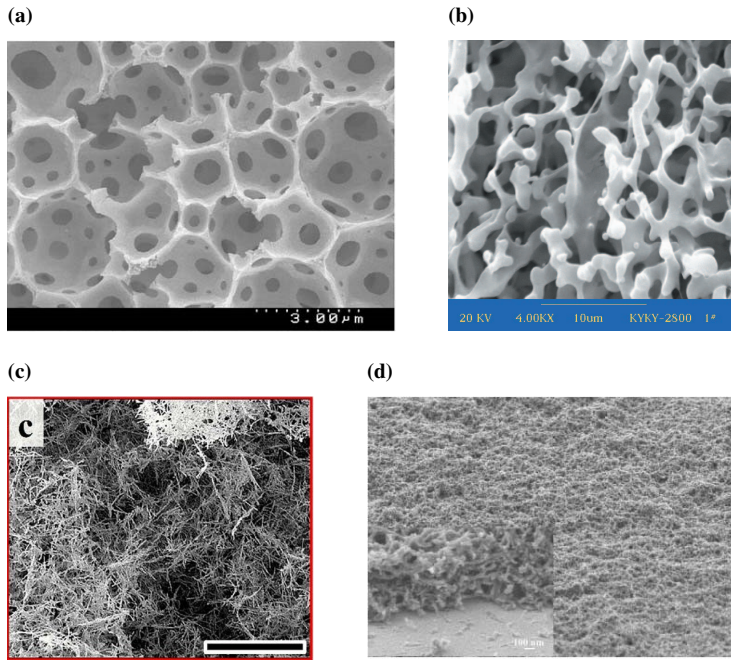


Figure 3.2: (a) High internal phase emulsion polystyrene foam [127]; (b) Deuterated polystyrene foam [128]; (c) Palladium nanowire foam (the scale bar is 30 μm) [129]; (d) Polyaniline nanofiber foam [130].

with the use of low-Z elements (as seen from the examples in figure 3.2, polymers is one of the preferred choices). Foam materials typically present porous morphological features starting at the micrometric scale, with void dimensions in the 1-10 μm range, together with—in most cases—an underlying nanostructure of the solid components of the foam. Their hierarchical structure can often be described as fractal-like, since equivalent morphological features are present at different spatial scales. Starting from these considerations, it is possible to model the average foam density ρ_f as a function of the solid component density ρ_s and dimension b_0 , together with the characteristic spacing between solid elements δ_0 (i.e. pore size) [131]:

$$\rho_f = \rho_s \left(\frac{b_0}{\delta_0} \right)^{\nu+1} \quad (3.1)$$

The parameter ν at the exponent varies depending on the solid elements' morphology: it is equal to 0 for membrane-based foams, 1 for filaments and 2 for clusters [132]. Its meaning is related to the fractal dimensionality, that is a measure of the space filling capability of the fractal structure. As real foams are often a composition of different structures, the actual number can

also fall between two values, and can be thought as a free parameter to be estimated experimentally. This is just one example of the interest in investigating and modeling the material morphology at the different scales, and relate the results to the macroscopic scale properties: it can then be possible to tune the material properties as desired through changes in morphology and composition.

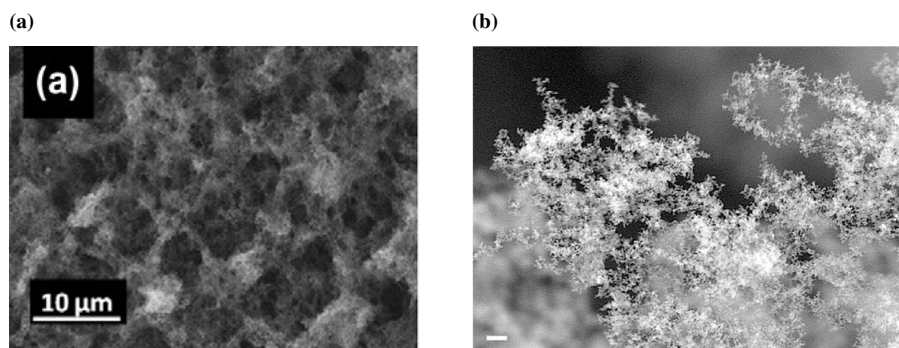


Figure 3.3: (a) Carbon nanofoam structure at the microscale [133]; (b) Detail of the foam structure at the nanoscale (the scalebar is 100 nm) [134].

A last interesting class of nanostructure materials, already under investigation for laser-matter interaction applications [79, 135, 136], are carbon nanofoams [133, 134]. As shown in Figure 3.3, they are nanoparticle-assembled materials, with a web-like structure at the micro and nanoscale emerging from the aggregation of 5-20 nm carbon nanoparticles. Thanks to the high porosity, average densities down to 1 mg/cm^3 can be achieved [133]. The material, depending on the synthesis conditions, can present a varying ratio of sp^3 (diamond-like) and sp^2 (graphitic) carbon.

3.2 Nanofoams synthesis methods

In the same way that material properties arise from the material composition and structure—also at the nanometer scale in the case of nanostructured materials—the process exploited to produce the nanostructured materials is at the foundation their morphology and structure. Therefore, in order to tune the material properties for a specific outcome, the investigation of the many possible synthesis methods and their influence on material properties is of central importance. Indeed, it is often the case that a specific synthesis technique can be exploited to produce a material with a limited range of properties and/or composition, and thus the choice depends on the specific needs of the target application. The techniques currently exploited for the

Chapter 3. Nanostructured materials and nanofoams

synthesis of foam materials are many, and defy simple categorization, due to the often complex procedure involving multiple material science synthesis methods. In general, both top-down and bottom-up approaches are feasible, and the same is true for chemical and physical-based techniques. In the context of nanostructured materials, top-down processes are generally simpler but limited in the achievable range of nanometric structures, while bottom-up approaches can lead to a more precise nanostructure control at a lower scale for the price of a greater complexity.

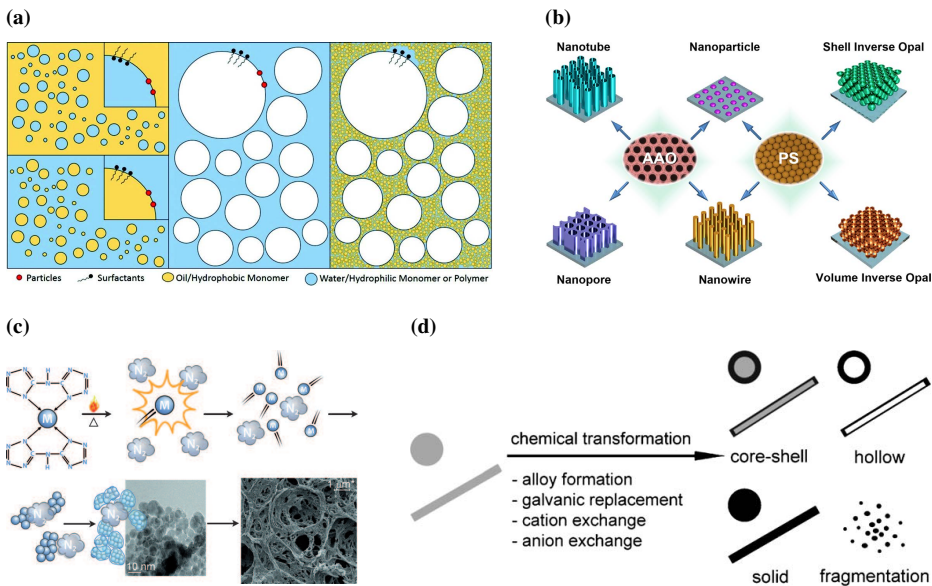


Figure 3.4: Schematic representation for different nanofoam and nanostructured material synthesis methods: (a) Liquid template synthesis [137]; (b) Solid template synthesis [138]; (c) Combustion synthesis [139] (d) Chemical transformations of existing nanostructures [140].

A significant example are polymeric foams—broadly employed outside of the nanotechnology field for multiple applications—obtained through *liquid templating* techniques [137]: by inclusion of a second gaseous or liquid phase (i.e. foams or emulsions, Figure 3.4a) prior to polymerization or solidification of the polymer matrix, a porous material can be obtained. The foam morphology is largely fixed, i.e. a solid matrix with voids in either ordered or disordered structures, characteristic of polymeric foams. A variant of this method, particularly relevant for the field of inertial confinement fusion, is *high internal phase emulsion* (HIPE) polymerization: by increasing the volume of the internal (secondary) phase, a structure with interconnected voids and a void fraction in excess of 90% can be obtained [127, 128, 141].

The pore size in liquid templating can vary significantly, from millimeter and micrometer dimensions to hundreds of nanometers—the limit being the smallest size of second phase/gas bubbles attainable in the templating phase. In order to go beyond this limit, while also enabling a greater morphological variety, other synthesis methods can be exploited. In *solid templating* techniques [142], the polymer can replicate a preexisting template (e.g. silica nanoparticles, mesoporous silica or anodic aluminum oxide, other polymeric nanomaterials) inverse structure, as outlined in Figure 3.4b; the nanostructuring capabilities are still somewhat limited due to the template own structure, but either nanofoam, nanorods or nanotubes morphologies can be obtained. Smaller nanostructures can be formed through *block copolymer self-assembly*, exploiting the self-organization of copolymers with chemically immiscible components, or by *direct synthesis*, where specific polymerization reactions can lead to the retention of solvent inside the polymer, which can later be removed originating the pores [143]. While allowing nanometer scale nanostructuring, the control of the morphology is limited (especially in the direct synthesis method) and less flexibility is allowed in the choice of polymer. This is a common limitation of chemical synthesis techniques: each is exclusive to a specific material, or a limited class of materials if multiple analogous reactions/processes are considered.

The exception are templating techniques, broadly applicable for polymeric, metallic and oxide foams. The difference is in the approach used to grow the foam material on the template: polymerization for polymer foams, electrodeposition for metals, chemical vapour deposition (CVD) or gas phase condensation for oxides [142]. Depending on the desired nanostructure properties, most of these methods can also be exploited directly without the need of a template: the advantages include the simplicity of the approach together with a lower scale nanostructuring potential, as opposed to a more challenging morphology control. Other notable direct synthesis methods are sol-gel techniques [144] and combustion synthesis (Figure 3.4c, applicable to both metals and oxides) or dealloying for metals [139]. As a last remark, chemical techniques can also be exploited to modify the morphology and composition of existing nanostructures through substitution, elimination or addition reactions [140]. Beside enabling the realization of nanostructures with greater compositional variety, it can lead to core/shell or hollow structures, as shown in Figure 3.4d.

On the other side, techniques based on physical processes are in general less common in nanostructured material synthesis, and even more in nanofoam synthesis. Their typical bottom-up approach could be promising to allow a finer control of the nanostructure morphology and properties—while at the same time being cleaner than chemical processes, as no

byproducts are generated and the original material composition is generally retained in the nanostructure—but the greater complexity has thus far hindered their widespread application. One exception could be ultrasound-based techniques, if not for the fact that they most commonly include *sonochemistry*, making it an hybrid technique: the extreme pressure and temperature conditions in the nebulized material are exploited to drive usually inaccessible chemical reaction and produce uncommon nanostructures [145]. Physical based techniques, such as those based on sputtering or laser ablation, are instead common in the production of nanoparticles [146, 147]: the different processes lead to material removal from a target, and the concurrent or subsequent formation of nanoparticles that can be collected on a substrate.

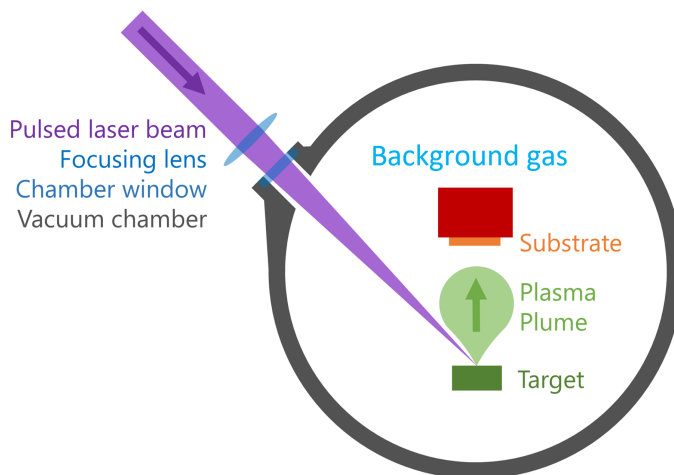


Figure 3.5: Schematic representation of the main components of a Pulsed Laser Deposition (PLD) setup.

These techniques could be particularly relevant for nanoparticle-assembled foam production, and indeed low-density carbon nanofoams were first obtained through Pulsed Laser Deposition (PLD) [134]. In greater detail, PLD is a physical vapour deposition technique, in which a pulsed laser is focused on a target inside a vacuum chamber. The ablation process—discussed with more detail in Section 1.2—leads to the emission of atomic and ionic species as well as cluster and nanoparticles, forming the plasma plume. The energetic ablates species can then travel toward the substrate, in a background atmosphere or in vacuum, leading to film formation. Figure 3.5 shows a schematic of the PLD experimental setup. The main well recognized advantage of PLD is the technique great versatility, resulting from its many tunable parameters and their interplay: laser wavelength, intensity, fluence, pulse duration, repetition rate, background gas composition and pressure,

target and substrate material, target to substrate distance can all be varied, each with its own effect on the deposition process and in turn material structure and properties. All three step of the process, namely the ablation phase, the propagation of the ablated species in the background atmosphere, and finally film growth on the substrate can be influenced by the PLD parameters. As a few relevant examples, the laser wavelength defines the photon energy, therefore a lower wavelength is generally required to successfully ablate high band gap materials. The laser fluence defines the amount of deposited energy per unit area, and is strongly related to the ablation rate and the ablated species energy [21]. The presence of a background gas can slow the ablated species through collision, favouring aggregation and allowing porous film production [133]. The substrate surface structure and its temperature can influence film growth and crystalline phase. Thanks to its flexibility, PLD is exploited to produce a multitude of different classes of material—from compact films to porous foams and nanostructured materials [148]—with thin films and coatings being the most technologically mature (and commercially exploited) application [149]. Most commonly PLD systems employ nanosecond-duration laser based either on Nd:YAG (fundamental wavelength 1064 nm and second harmonic 532 nm) or excimer gases (UV, around 200 nm), with pulse energy of a few Joules and operating fluences in the order of some J/cm^2 [21]. The repetition rate goes from 10 Hz for Nd:YAG up to 1 kHz for excimer lasers.

Considering the synthesis of carbon nanofoams, unconventional deposition conditions were exploited in the first works by Rode and coworkers to obtain carbon nanofoam materials with high sp^3 bonding fraction: high fluence ($120 \text{ J}/\text{cm}^2$), 120 ns pulse duration, high argon pressure (10^4 Pa) and high repetition rate (10 kHz) [134, 150]. Later works exploited more conventional PLD conditions ($0.8 \text{ J}/\text{cm}^2$, 5 ns pulses, 10 Hz) to obtain carbon nanofoams with quite similar properties, beside the lower sp^3 content and predominance of nanocrystalline graphite [133]. By changing the background gas and its pressure (1-1000 Pa of helium or argon) carbon nanostructured films with densities from 1000 down to $1 \text{ mg}/\text{cm}^3$ were obtained through PLD, showing the technique versatility (in Figure 3.6a the density evolution is shown).

Considering its importance in light of material properties and morphology control, it is worthwhile to enter in some detail regarding nanofoam growth dynamics in PLD: the process can be well described by a snowfall-like aggregation model, in which ablated species are slowed to a diffusive regime, aggregate while in flight and finally are deposited on the substrate growing the nanofoam [151]. The ablated species, chiefly in the form of neutral atoms and ions [152] can first aggregate into nanoparticles with di-

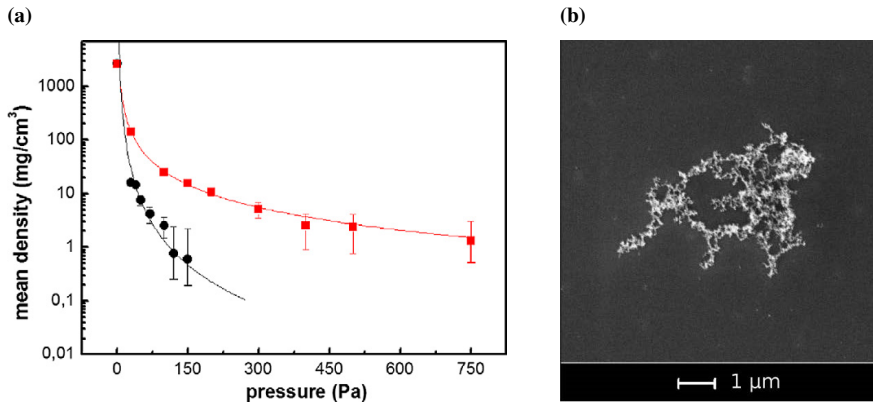


Figure 3.6: (a) Average density evolution of carbon nanofoams and nanostructured films from 1 to 1000 Pa of argon (in black) or helium (in red). Missing data at high pressure is due to substrate partial coverage (from [133]); (b) Typical fractal aggregate composing carbon nanofoams, obtained with a short deposition of just 10 laser shots (adapted from [151]).

mension in the order of ~ 10 nm [133] thanks to the interaction with the background gas—which favours plume confinement and in-plume interactions. The nanoparticles thus formed can themselves be slowed until they reach a diffusive regime, as indicated by an ablation plume shorter than the target-to-substrate distance. The process gives rise to micrometric fractal aggregates with fractal dimension D close to 1.8, typical of diffusion-limited cluster-cluster aggregation [153]. In the theory of fractal aggregate formation, one main distinction is between cluster-cluster aggregation models—typical when a high number of particles are free to move in a certain region of space, such is the case for PLD at high background pressure—and particle-by-particle growth—simpler situation in which the aggregate growth happens by addition of a single particle at a time. This last case can be found in PLD under low gas pressure conditions, where the ablated species are not efficiently slowed and travel linear trajectories, growing the more compact and directional structures characteristic of ballistic aggregation dynamics. A second highly important element in determining the aggregate fractal structure is the growth limiting factor: upon reaching the aggregate, if the nanoparticle sticking probability is high the process is diffusion-limited, leading to more open structures and lower fractal dimension; on the contrary, a near-zero sticking probability is the hallmark of reaction-limited aggregation, giving rise to more compact aggregates (thus characterized by a higher fractal dimension) [154].

Coming back to diffusion-limited cluster-cluster aggregated carbon nano-

3.3. Laser-matter interaction with micro and nanostructured materials

foams, Figure 3.6b depicts a characteristic aggregate, as deposited on the substrate after 10 laser shots. Overall, the nanofoam structure is the ensemble of all the aggregates deposited on the substrate one after the other. A consequence of the snowfall-like aggregation model is that the main parameter defining aggregate size is the aggregation timescale, which has been shown to be dominated by the shot-to-shot time (and thus the laser repetition rate): the shockwave generated from the subsequent laser pulse pushes the aggregates toward the substrate, acting as a hard upper limit on the aggregation time [151].

3.3 Laser-matter interaction with micro and nanostructured materials

As is clear from the discussion in Chapter 2, the enhancement of laser-matter interaction and efficient energy transfer is of fundamental importance in all the foreseen applications, whether the aim is to achieve net positive energy gains in nuclear fusion [81], obtain accelerated ion beam properties of medical relevance [50] or realize a compact tabletop laser-driven accelerator [136]. Among the different explored approaches, micro- and nano-structured materials have gathered considerable scientific interest in recent years—most notably in the field of laser-driven particle acceleration [76, 79, 136, 155] and to a lesser extent inertial confinement fusion [156–159]—owing to the multiple favourable properties that can be exploited in the field of laser-matter and laser-plasma interaction. Notably, their high surface area and porosity permits laser propagation, leading to a more efficient volumetric interaction. At the same time, thanks to the flexibility enabled by their varied morphologies, they are among the few classes of solid (albeit porous) materials able to reach near-critical densities, in the order of a few mg/cm^3 ; the most relevant examples are micro- and nano-structured foams with a substantial void fraction, that are ionized and originate a near-density plasma after interaction with the laser rising edge or prepulse. As anticipated in Section 1.2, laser-plasma interaction is strongly enhanced under these conditions, allowing an efficient energy transfer between laser photons and material electrons, along with other beneficial effects such as self-focusing of the laser pulse in the near-critical plasma. Indeed, conversion efficiency and maximum proton energy enhancements were demonstrated by exploiting laser interaction with near-critical plasmas—created through secondary long duration pulses [70] or proper prepulse control [160].

In the context of nanostructured targets, it should specifically be noted the high relevance of laser pulse properties (contrast, intensity, pulse dura-

tion) in guiding the evolution of laser-nanostructure interaction processes, also in respect to the timescales of material ionization and plasma expansion [136, 161]. And connected to this, the influence that material properties (down to the nanoscale morphology) can have on the process. Considering a high intensity laser interacting with a nanostructured material, one may expect fast ionization, plasma formation and limited memory of the original morphology in the plasma density distribution (i.e. nearly complete homogenization). Indeed it is possible to estimate the nanostructure disintegration timescale, taking into account both hydrodynamic expansion (characteristic velocity equal to the ion sound speed $c_s \sim \sqrt{\gamma Z T_e / m_i}$, where $\gamma = 5/3$ is the adiabatic index of a monoatomic gas) and Coulomb explosion (if all electrons are ejected, the velocity of a single ion originally in the nanoparticle can be estimated as $\omega_{pi} R$ thanks to energy conservation, where $\omega_{pi} = \sqrt{4\pi Z^2 e^2 n_i / m_i}$ is the ion plasma frequency). Considering a light element such as carbon ($Z = 6$, $A = 12$) and reasonable values for the remaining parameters ($T_e = 100$ keV, $n_e = 200n_c$), both velocities are in the order of ~ 1 - 10 $\mu\text{m}/\text{ps}$, resulting in a timescale of ~ 100 fs for nanoscale structures of ~ 10 nm separated by characteristic void sizes of ~ 1 μm [136]. Being the timescale longer or comparable with the duration of ultrafast high-intensity laser pulses, it is in fact possible for the specific nanostructure morphology to have an effect on laser-matter interaction.

The effect was demonstrated through Particle In Cell (PIC)¹ 2D and 3D simulations of homogeneous, foam-like, ordered nanowires and random nanowires plasmas, in a range of plasma density and laser intensity combinations [136, 161]. In Figure 3.7 the main findings are shown: under strongly interacting conditions (i.e. relativistically near-opaque plasmas) all nanostructures showed a substantial enhancement in laser energy absorption if compared to the homogeneous case (e.g. 80% against 20% total energy absorption for $a_0 = 5$, $n_0 = 3n_c$). This is reflected in higher energy absorption by electrons (as expected) but also by ions, due to the electric fields generated by the Coulomb explosion process. At the same time, significant differences between each nanostructure can be found in the hot electron energy spectra, particularly in the number of electrons accelerated up to relativistic energies and the angular distribution of accelerated electrons and ions. The interconnection with the interaction regime was also clearly evidenced: due to relativistic self-induced transparency (described in Section 1.2) the same plasma density can become transparent for higher laser intensities, transitioning from a strongly interacting near-critical plasma to a mostly transparent one, where total absorption is low, but the nanostructure

¹PIC are numerical method allowing a self-consistent kinetic description of plasma dynamics and electromagnetic fields, extensively exploited to model laser-plasma interaction [162].

3.3. Laser-matter interaction with micro and nanostructured materials

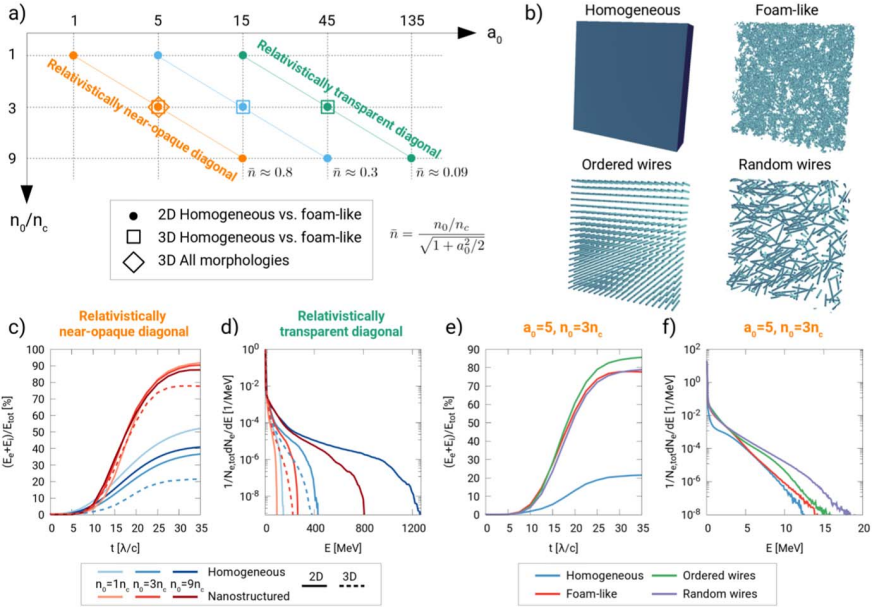


Figure 3.7: Main results of 2D and 3D PIC simulations on a variety of nanostructures, showing the improvement in energy absorption efficiency under a variety of conditions and the influence of the specific nanostructure [136].

enhancement is mostly retained.

Further evidence supporting the effectiveness of nanostructured materials in laser matter interaction applications, even outside the concept of near-critical materials, are the many ion acceleration experiments in which target nanostructuring was successfully exploited. One example is polystyrene nanospheres coated targets [76], where 60% enhancement in proton cutoff energy and 5-fold increase in the number of > 1 MeV protons was demonstrated. Interestingly, the nanoparticle dimension was shown to have a significant role in the effectiveness of the enhancement, with 532 nm nanoparticles giving the best results (compared to the 800 nm laser wavelength). This is further proof of the nanostructure properties importance, and was attributed to the increased surface area available for laser-matter interaction along with collective interaction between electrons belonging to neighboring spheres and the laser field. A second example are target surface modifications like laser induced periodic surface structures (LIPSS) [163], able to enhance laser absorption efficiency in a range of different plasma conditions (e.g. also higher intensity conditions and no plasma mirror for prepulse elimination). In fact, nanostructured targets were always able to increase laser energy absorption into hot electron, but this was not always reflected in enhanced proton acceleration: it was suggested that the improvement occurred

only in non-optimal laser-target conditions, such as too low intensities, target thickness or poor laser temporal shape. Indeed, nanostructured targets can serve as a powerful tool to relax the requirement on the laser-target configuration, limiting the negative repercussions on the process performance.

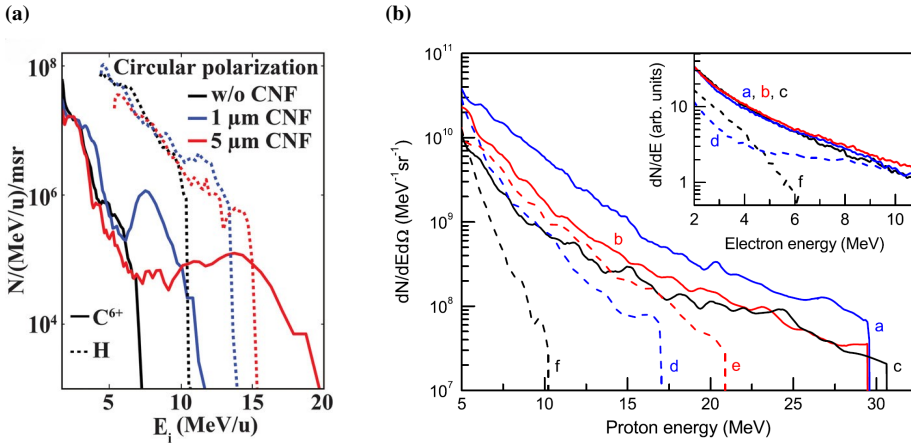


Figure 3.8: Experimental ion spectra showing the enhancement in proton and carbon ion energies exploiting near-critical DLTs. (a) carbon ions (solid lines) and protons (dotted lines) from carbon nanotube foam (CNF) targets (from [155]); (b) proton energy spectra from bare Al targets (dashed lines) and carbon nanofoam DLTs (solid lines) in different polarization conditions (s-, p- and c- in blue, red and black respectively, corresponding electron energy spectra are shown in the inset [164]).

The most common and successful approach, as could be expected, is the combination of the two, that is nanostructured targets of near-critical density. In the framework of ion acceleration, the target configuration is known as DLT (Double Layer Target) [], in which the nanostructured low density layer facing the laser is combined with a conventional thin solid foil. Through this approach, clear improvements in ion acceleration performances were demonstrated: 5 μm carbon nanotube foams on thin nanometric diamond-like carbon foils led to almost tripling the carbon ion energies (Figure 3.8a), attributed to the relativistic self-focusing and pulse front steepening induced in the near-critical density layer [155]. The experiment was specifically aimed at the radiation pressure acceleration regime (RPA), exploiting circularly polarized pulses to suppress TNSA, thus confirming the robustness of the approach in acceleration regimes beyond TNSA. Analogous results were obtained with carbon nanofoam-based DLTs on micrometric Al foils [79, 164], with significant enhancements in accelerated proton energies as shown in Figure 3.8b. Another compelling finding is the polarization independence induced by the presence of the foam layer, along with

3.3. Laser-matter interaction with micro and nanostructured materials

the absence of detrimental effects if the aluminum foil thickness is changed (even doubled), all confirmations of the greater robustness of the DLT approach.

Foam materials—mainly in the form of chemically synthesised polymeric microstructured foams—have also been investigated in the field of inertial confinement fusion. The first applications were actually not related to the foam advantageous laser-matter interaction properties: rather, they were exploited as an internal capsule scaffold permeated with liquid DT, allowing better hotspot control if compared with standard DT ice, or to mimic the behaviour of the DT ice without cryogenic requirements [159, 165]. Their applications as laser-facing components in ICF have also been studied, both for the indirect drive configuration, through the use of foam-lined hohlraums, and direct drive approach, with foam ablaters directly on the capsule external surface. In the first case, the enhanced X-ray generation of foam materials can be exploited, such as with gold foams [158], together with decreased fuel capsule preheating, despite experiments on the NIF with Ta₂O₅ aerogels did not show improvements in implosion symmetry with the chosen foam conditions [166]. In the second case, the foam material can enhance the conversion of laser energy to shock wave energy [157], and even more importantly smooth the laser inhomogeneities and reduce the growth rate of Rayleigh-Taylor instabilities, thanks to the higher ablation velocity and longer plasma density scale length. These effects were observed in both hydrodynamic simulations [156, 167] and experiments [156]. The foam that give the best results for ICF applications are moderately overdense (in contrast with the near-critical or slightly undercritical foams of laser driven ion acceleration), due to the higher laser energy, duration and different overall goal: this is an example of how the aim and laser system influence the desired properties in foams and nanostructured materials for laser-matter interaction applications. Despite the promising results, the approach shows a lower maturity if compared with laser-driven ion acceleration—in no small part consequence of the very limited number of facilities operating laser relevant for ICF experiments, together with the higher complexity and more stringent requirements of ICF—warranting further study.

Similar consideration can be made for the field of proton boron fusion, were in order to promote more fusion reactions (and thus accelerate a high number of alpha particle) picosecond or nanosecond duration lasers are preferred. Even more than for ICF, the application of nanostructured or near-critical material is not common, also due to the low maturity of the field. Some explored possibilities include creation of a boron and hydrogen plasma with long nanosecond lasers [99] and the use of polymeric films on solid boron nitride targets to provide hydrogen [105], but without the specific

Chapter 3. Nanostructured materials and nanofoams

aim of increase laser-matter interaction thanks to nanostructuring. Therefore, further investigation in the application of advanced target concepts to proton-boron fusion is of clear interest—also taking into account their success in other laser-matter interaction applications.

CHAPTER 4

Thesis goals and methods

After having delineated the framework and literature on which this work is based, in this Chapter the objectives of the PhD thesis work are discussed (Section 4.1), together with the chosen methods of nanomaterial production, ns-PLD and fs-PLD (in Section 4.2) and the characterization techniques exploited (Section 4.3): Scanning Electron Microscopy (SEM), Energy Dispersive X-ray Spectroscopy (EDXS) and Raman spectroscopy. Lastly, the laser facilities exploited in the laser-matter interaction experimental campaigns performed in the framework of this thesis work will be introduced in Section 4.4.

4.1 Thesis objectives and personal contribution

In light of the framework delineated in the previous Chapters, the general objective of this thesis work is to investigate low-density nanostructured materials for laser-matter interaction applications, from their production through ns-PLD and fs-PLD to their subsequent characterization, optimization and application in high-intensity laser-driven experimental campaigns.

In order to do so, the first step is an in-depth investigation into nanofoam production through PLD, with the aim to determine how the macroscopic material properties are related to nanoscale morphology, and how they are

influenced by the main deposition parameters governing the aggregation process. The comparison between ns-PLD and fs-PLD can be particularly helpful in giving insight into the underlying mechanisms of nanoparticle aggregation and foam growth, also leveraging the more established knowledge of carbon nanofoam production through ns-PLD in order to study fs-PLD. This is one of the reasons why carbon was chosen for this first investigation, together with its low atomic mass (facilitating the production of near-critical density foams) and previous ion acceleration experiments already confirming its efficacy. In this work, described in Chapter 5, my contribution focused on foam production and most of the characterization and data analysis. Still toward the same aim, the analysis is then expanded to different elements in Chapter 6, exploiting the flexibility of the fs-PLD technique. Similarly to how the comparison between ns-PLD and fs-PLD of the same element can be exploited to draw insights on the deposition process, the study of the synthesis of nanofoams of different elements through fs-PLD can give indications on how the material properties interact with deposition parameters to determine the properties of the nanofoam. For this reason the investigated materials were chosen to span a variety of material properties (density, metallic character, melting temperature etc.) giving precedence to those with significant applicative interest (e.g. gold, boron). I personally performed the nanofoam depositions, characterizations and subsequent data analysis.

The results of the in-depth investigation into the PLD technique and nanofoam production were then put to use toward the last aim: the design and production of nanofoam-based targets, and their test in application-oriented laser-driven experimental campaigns. The first one, addressed in Chapter 7, is performed in collaboration with CLPU (Centro de Laseres Pulsados in Salamanca), on the petawatt-class laser Vega 3. In the framework of laser-driven particle acceleration, the campaign is aimed at investigating proton and secondary neutron generation by exploiting Double Layer Targets (DLTs), composed by freestanding thin substrates produced by magnetron sputtering on which carbon nanofoam is deposited through ns-PLD. Beside participation in the experimental campaign and assisting in data collection, my main contribution was related to nanofoam production and post-mortem analysis of the targets.

The potential application of carbon nanofoams as ablator in ICF, described in Chapter 8, is investigated in collaboration with ENEA Frascati, hosting the high energy nanosecond duration ABC laser. First, in the framework of the master thesis of Vittorio Ciardiello [168], exploratory hydrodynamic simulations are performed, with the aim to define the optimal foam parameters. Carbon nanofoam produced through ns-PLD and fs-PLD are considered: I handled nanofoam production and characterization, and col-

4.2. Nanosecond and femtosecond Pulsed Laser Deposition

laborated to the integration of the nanofoam structure into the hydrodynamic code MULTI-FM. According to the simulation results, I collaborated to the design and production of the carbon nanofoam targets with ns-PLD, experimental activity performed in the framework of another master thesis work (Maria Sole Galli De Magistris [169]). I also participated in the high-energy laser-driven experimental campaign and the subsequent data analysis phase, focusing on the post-irradiation target analysis.

Lastly, in the framework of proton-boron fusion research, the universal character of fs-PLD is leveraged to produce hydrogen-enriched boron nanofoam targets, with the aim to increase the alpha particle yield if compared to a simple solid target. The investigation, reported in Chapter 9, is performed in the framework of a master thesis work (Alessandro Milani [170]) and in collaboration with the research group of the TARANIS laser. I was in charge of target production and characterization for the experiment, and participated to the high-intensity laser-matter interaction experimental campaign at the TARANIS laser.

4.2 Nanosecond and femtosecond Pulsed Laser Deposition

The foundation of the research activity performed in this thesis work, dealing with nanofoams and nanostructured material production, is the Pulsed Laser Deposition (PLD) technique. As previously described in Chapter 3, it is a physical vapour deposition technique exploiting a pulsed laser to ablate material from a target, in the form of atoms, ions or clusters. The ablated species can travel in a controlled background atmosphere, and grow a film on a substrate placed in front of the target.

Most commonly, nanosecond duration lasers pulses are exploited, that cause atoms and ion emission through heating and vaporization processes. The ns-PLD system exploited in this work is based on a Q-switched Nd:YAG laser (frequency doubled to $\lambda = 532$ nm), with 5-7 ns pulse duration, 10 Hz repetition rate and 1 J maximum pulse energy. As introduced in Chapter 1, the predominant laser-matter interaction processes can significantly differ depending on pulse duration, and indeed considering femtosecond duration pulses leads to the strong reduction of thermal effects and a predominantly electronic ablation mechanism. Particularly relevant for the production of nanoparticle-assembled nanostructured materials is the direct synthesis of nanoparticles, with the potential for an improved nanostructure control. Moreover, the specificity of each ablation mechanism results in a significant enhancement in the total available parameter space—and thus greater flexibility in nanomaterial synthesis—if both techniques are considered. The temporal evolution of the ablation phenomena and the resulting

Chapter 4. Thesis goals and methods

plasma plume in the two case are shown in Figure 4.1, as an indication of the differences in ablated species properties and thus behaviour (such as energetics and angular distribution) in ns-PLD and fs-PLD.

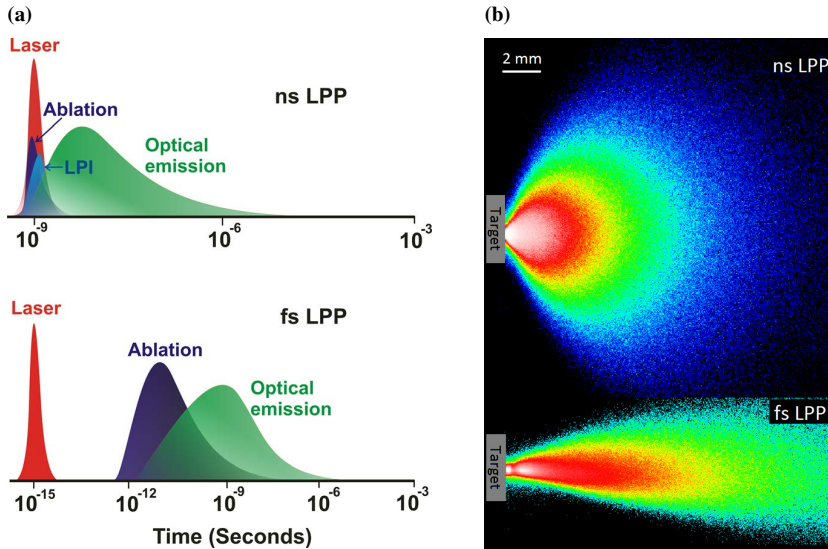


Figure 4.1: (a) Qualitative comparison of the timescale of nanosecond and femtosecond ablation processes and (b) two-dimensional image of laser-produced plasma (LPP) plumes for the two regimes, as captured by an ICCD (gated intensified camera, wavelength range 350-900 nm, 2 μ s integration time). The self-emitted light intensity is shown by color code from white to blue (from [171]).

The fs-PLD system at Politecnico di Milano, installed as a part of the ERC ENSURE project [172] financed by the European Union, consists of a vacuum chamber coupled with a commercial ultrashort laser (Coherent Astrella). The laser is based on the chirped pulse amplification technique, allowing 80 fs pulses with 5 mJ maximum energy at a repetition rate of 1 kHz. The laser medium is a Ti:Sapphire crystal, with a central wavelength of 800 nm. In both cases, the laser is focused on the PLD target at 45° incidence through suitable lenses, allowing variation of the fluence and intensity by changing the laser spot size.

4.3 Nanofoam characterization techniques

Considering the aims of this thesis work, the most important characterization is related to the morphological analysis of the nanostructured produced, from the micro to the nanoscale. Scanning Electron Microscopy (SEM), thanks to its high resolution and flexible magnification, is especially suited for that

4.3. Nanofoam characterization techniques

purpose. A scheme of a typical SEM is shown in Figure 4.2: the electrons produced from a filament (through thermionic effect) are collimated and focused on the sample, and can be collected after the interaction to reconstruct the sample morphological features. Two main detectors are exploited for electron microscopy: one for the backscattered electrons, placed near the electron source (close to the target normal) and one for secondary electrons, at higher angles.

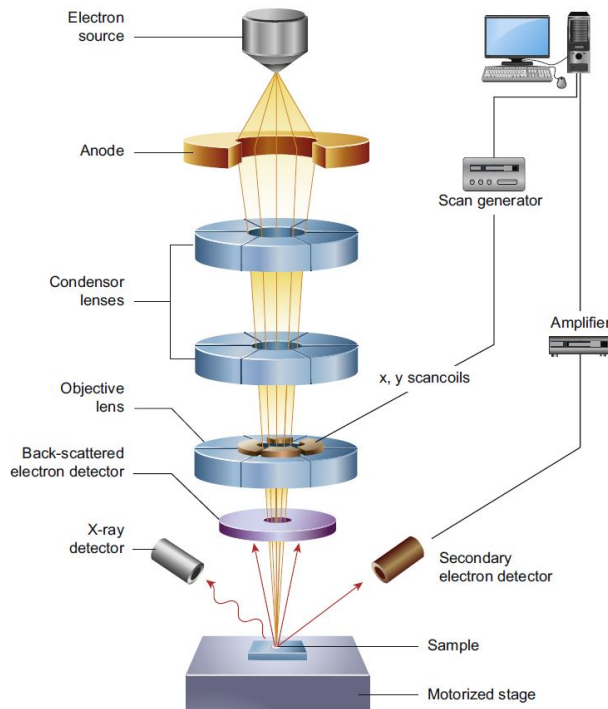


Figure 4.2: Schematic representation of all components of a scanning electron microscope (from [173]).

Both are useful since they provide different physical information: secondary electrons, emitted due to the inelastic scattering of SEM electrons with the target electrons, have low energy, therefore they can escape the material only if they are close to the surface. The secondary electron image is thus a faithful representation of the surface morphology of the sample, with depth perception due to shadowing effects. On the contrary, the backscattered electrons are the original SEM electrons undergoing elastic collisions, which depend on the atomic number, therefore they can give qualitative indications on the sample composition. It should be noted that only conductive material can be characterized by SEM, since insulating ones retain the elec-

trons on the sample surface and charge it, leading to unwanted deflections of any subsequent electron.

In this thesis work, a Zeiss Supra 40 field emission scanning electron microscope is exploited, with accelerating voltage ranging from 5 to 30 KV.

Compositional analysis is almost as important as morphological investigation for this thesis work, in order to determine eventual contaminants present in the material and—even more importantly—checking the composition of multielemental films. This can be done by exploiting the SEM electrons to perform Energy Dispersive X-ray Spectroscopy (EDXS) analyses, by adding a proper X-ray detector and readout system to the SEM setup. The technique is based on the emission of characteristic X-rays after the excitation and de-excitation of atomic transitions, stimulated by the incoming SEM electrons. By exploiting proper models, a quantitative estimation of sample composition is possible, since the X-ray intensity is proportional to the concentration of the specific element (under the hypothesis of homogeneously distributed samples).

SEM and EDXS together can also be exploited to determine one of the most relevant macroscopic property related to laser-plasma interaction, that is the average density of the nanostructured film: cross section SEM measurements can be exploited to measure the geometrical thickness, while EDXS can give quantitative information on the film mass thickness: by measuring the X-ray intensity of both film and substrate, along with a proper model of the electron transport and X-rays emission, the mass thickness of the film can be evaluated (EDDIE method, described in detail in [174]). With independent knowledge of geometrical and mass thickness, the average material density is simply their ratio.

Finally, information on the bonding structure is also quite relevant in relation to material properties, specifically for the case of carbon nanofoams, due to the many carbon hybridization states. These properties can be probed through vibrational spectroscopy, such as Raman spectroscopy, giving complementary insight if compared with the previous characterization techniques: monochromatic laser photons are exploited to interact inelastically with the target material, and specifically with its vibrational states, leading to measurable shifts in the photons energy. This probes the material properties at the atomic and nanometric level, which is indeed complementary with the SEM morphological analysis.

4.4 Introduction to the laser facilities of this thesis work

One of the main points of interest pertaining to this thesis work is related to the experimental test of the produced nanostructured materials under quite

different laser parameters, and thus laser-matter interaction conditions. As explained in Chapter 2, depending on the target application, the requirements on laser systems may differ: highly energetic nanosecond pulses are needed to drive capsule compression in ICF, while short high-intensity femtosecond pulses can create the highest fields and efficiently accelerate ions. At the same time, investigating the behaviour of nanostructured materials interacting with such a variety of laser systems can allow a deeper understanding into the effects of the nanostructure over laser-matter interaction, also in relation to the laser pulse properties.

The first laser system, exploited in the experimental campaign for particle acceleration described in Chapter 7, is the VEGA 3 laser at CLPU (Centro de Laseres Pulsados) [175], Salamanca, Spain. It is a Petawatt-class laser, based on Ti:Sapphire technology: thanks to Chirped Pulse Amplification (CPA) and multiple amplification stages, it is able to provide 30 fs pulses with 30 J per pulse at $\lambda = 800$ nm, and up to 1 Hz repetition rate. Ultrahigh intensities up to 10^{20} W/cm² can be reached, depending on the focalization conditions, with a high contrast ratio of 5×10^{-12} .

At the opposite side of the spectrum the ABC laser is found, part of the ENEA Frascati laboratories [176] near Rome, Italy. The laser design includes two counterpropagating identical beams, and was designed and built with the aim to investigate laser-driven material compression in conditions relevant for ICF. It is based on Nd:glass-phosphate active media, and able to deliver two 3 nm pulses (FWHM) of 100 J each at 1054 nm in nominal conditions. Intensities in the order of 10^{14} - 10^{15} W/cm² can be achieved. Due to the longer pulse duration—itself in the nanosecond range—and the lower peak intensity, the contrast ratio is a parameter not generally considered for long pulse lasers. This is the laser exploited in the investigation of carbon nanofoams as ICF ablator materials in Chapter 8.

Lastly, the TARANIS laser system [177, 178] of Queen's University Belfast (UK) can be thought as a middle ground between the two previous options. It is also based on a CPA scheme, but exploits a hybrid Ti:Sapphire-Nd:glass system, respectively for the oscillator/first amplification and for the main amplification stages. Energies up to 20 J per pulse can be achieved, with tunable pulse duration in the hundreds of femtoseconds/picosecond range, leading to a 20 TW peak power. The central wavelength is 1053 nm, and ultrahigh intensities in excess of 10^{19} W/cm² are within the laser capabilities (depending on pulse duration and focalization conditions). The TARANIS laser system is not optimized for high-contrast operation, presenting a 1.5 ns pedestal with a contrast ratio of 5×10^{-7} . The experiment regarding proton-boron fusion in nanostructured targets is performed on this laser, as described in Chapter 9.

Part II

**Experimental investigation on
nanofoam production with Pulsed
Laser Deposition**

CHAPTER 5

Carbon nanofoam production through ns-PLD and fs-PLD

In this first result Chapter, the investigation on carbon nanofoams and nanostructured films production through PLD is performed, considering both the established ns-PLD technique and the innovative fs-PLD. The effect of the main deposition parameters is investigated: the laser fluence, the background gas pressure in the chamber and the pulse duration (nanoseconds or femtoseconds). Considering the nanofoam aggregation mechanism, for which fractal aggregate are formed while in flight, it is of particular interest to investigate the early film growth stages, to characterize the aggregates and the variation of their properties as a function of the aforementioned process parameters. 30 seconds depositions are performed with these aims, and the results reported and discussed in Section 5.1. In Section 5.2, the analysis is expanded to fully grown nanofoam (10 minutes deposition time), exploring their morphology at different spatial scales, also in relation to the aggregate properties. Section 5.3 is dedicated to the investigation of the carbon bonding structure, complementary to the morphological investigation and useful in support of the previous results. Finally, the nanofoams average density is characterized in Section 5.4, exploiting the previous analysis to propose a model to link the nanofoam density with the corresponding ag-

gregate properties. The results of this investigation have been published in the *Applied Surface Science* journal with the title “Pulsed laser deposition of carbon nanofoam” [179].

In order to draw meaningful comparisons between ns- and fs-PLD, both the fluence and the average laser power delivered on target are kept constant. Since the repetition rate is one hundred times greater for fs-PLD (1 kHz against 10 Hz) the pulse energy was reduced accordingly to compensate. The same fluence is kept by changing the spot area, which has to be 100 times lower in fs-PLD. The fluence is varied from 180 to 520 mJ/cm² (spot size is 8 mm for ns-PLD and 0.8 mm for fs-PLD, along with a laser energy of 130 to 520 mJ for the former and 1.3 to 3.9 mJ for the latter) leading to an average power of 1.3 to 3.9 W¹. The laser intensities reached—about 10¹² W/cm² for fs-PLD and 10⁷-10⁸ W/cm² for ns-PLD—reflect the differences in pulse duration, moderated by the higher energy per pulse of the nanosecond laser. Argon was chosen as background gas due to its inert properties, along with the higher atomic mass compared to most common alternatives (e.g. helium) providing a greater efficiency in slowing down the ablated species. Vacuum conditions (< 10⁻³ Pa) up to 300 Pa are investigated. The target to substrate distance is kept constant at 7 cm, and (100) single-crystal silicon wafers are employed as substrates throughout the whole deposition campaign.

5.1 Fractal aggregate analysis

In the SEM micrographs of Figure 5.1, the effect of the background argon pressure on the fractal aggregates is shown, from 25 to 200 Pa. In vacuum conditions (not shown) no aggregates nor nanoparticles were visible. Starting from 25 Pa, single nanoparticles are present, while aggregates start to appear at 50 Pa for both ns- and fs-PLD. With increasing pressure, the aggregates gradually increase in size, most notably for fs-PLD. Despite these similarities, a significant difference between the two techniques is shown in the higher magnification bottom panels of figure 5.1: between 50 and 100 Pa in fs-PLD there is the coexistence of larger micrometric aggregates with a background of smaller aggregates/single nanoparticles, tens or hundreds of nanometers in dimension. As above, the aggregate size increases with pressure, and interestingly for 200 Pa only the larger micrometric aggregates survive. Therefore, in contrast to the single aggregate population typical of ns-PLD, a double population is a characteristic feature of fs-PLD at intermediate pressures. A potential interpretation of the general pressure

¹For the case of ns-PLD, 720 mJ/cm² is also investigated, corresponding to 520 mJ. Due to the limitation to 5 mJ per pulse for the femtosecond laser, the corresponding point for fs-PLD cannot be included, as it would require 5.2 mJ.

trend comes from the effect of a higher background gas pressure, able to both slow down the ablated species to a diffusive regime and promote an increased plume confinement, both favouring the aggregation process. In this picture, the background population of fs-PLD corresponds to the more energetic ablated species, that the background gas is not able to slow to a diffusive regime.

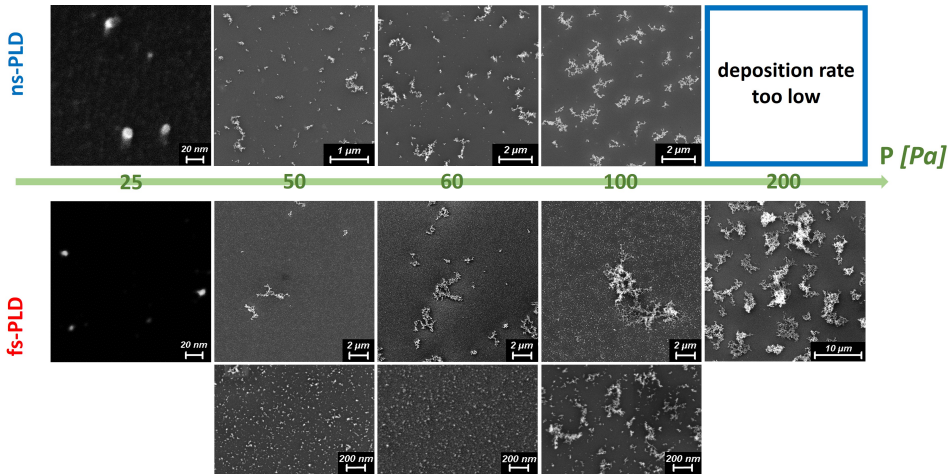


Figure 5.1: SEM images of the fractal aggregates composing the foam, obtained with 30 seconds deposition time, showing their pressure evolution (at 360 mJ/cm^2 constant fluence). The top row micrographs refer to ns-PLD, the bottom two to fs-PLD (lower magnification in the middle row and higher magnification for the bottom row).

The laser fluence effect, as shown in Figure 5.2, appears to be less prominent: in ns-PLD, aggregate dimensions do not vary significantly, and the main fluence effect is to increase the number of aggregates, due to the higher ablation rate. The exception is 720 mJ/cm^2 , for which the aggregate size is much larger. Also for fs-PLD, the large aggregate size is not significantly influenced by the fluence, but interestingly the contrary is true for the background aggregate population (bottom panels of Figure 5.2): with increasing fluence, their size decreases down to single nanoparticles at 540 mJ/cm^2 . Considering the constant argon gas pressure, together with the origin of the background aggregate population in fs-PLD as the most energetic ablated species, the interesting conclusion is that a higher fluence leads to a higher ablated species energy in fs-PLD, as demonstrated by the lower aggregate size. This is not the case for ns-PLD, where the ablated species energy seems to be substantially independent from the laser fluence.

In order to perform a more detailed quantitative analysis on the aggregate properties, their main properties are considered, taking advantage of the

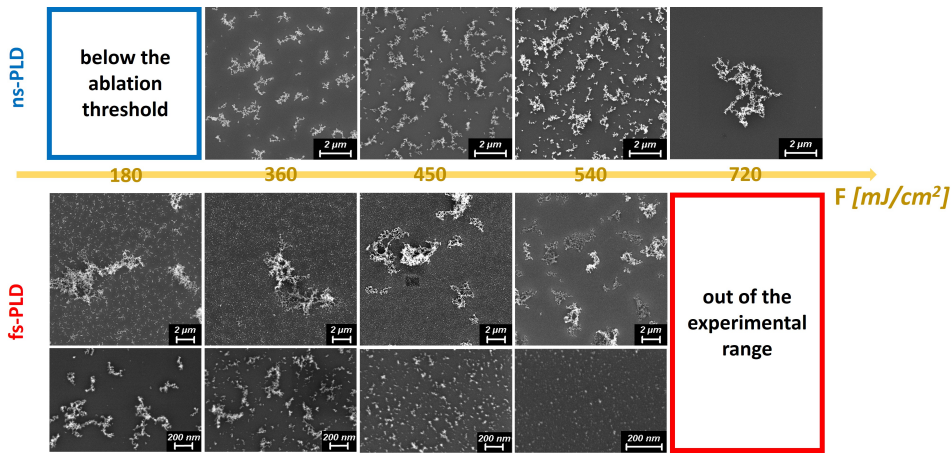


Figure 5.2: SEM images of the fractal aggregates composing the foam, obtained with 30 seconds deposition time, showing their fluence evolution (for a fixed 100 Pa argon pressure). The top row micrographs refer to ns-PLD, the bottom two to fs-PLD (lower magnification in the middle row and higher magnification for the bottom row).

fractal description. A nanoparticle-assembled fractal aggregate can be accurately described by only three parameters: the nanoparticle diameter d_{np} , the fractal dimension D_f and the gyration radius R_g , schematically depicted in Figure 5.3d. The fractal dimension describes the space-filling capabilities of the structure, or equivalently the different scaling in respect to the space where the structure is embedded; the gyration radius is one of the possible parameters related to the size of the fractal aggregate, and is defined as the equivalent radius at which the total aggregate mass would have to be placed to have the same moment of inertia of the original aggregate. The three parameters are linked in the well-known fractal scaling law [154],

$$N \propto \left(\frac{2R_g}{d_{np}} \right)^{D_f} \quad (5.1)$$

where N is the total number of nanoparticles composing the aggregate.

The nanoparticle size can be directly estimated from 2D SEM images: despite the potential electronic and post-processing effects that may distort nanoparticle size in SEM micrographs, the cross validation through a second method—based on the two-dimensional pair correlation function of binarized images [180]—confirms the validity of the approach. The estimation of D_f and R_g is instead more complicated, since they are inherently three-dimensional parameters and information loss is inevitable while transitioning to a 2D SEM image. Therefore, a method to relate the real 3D D_f and R_g of the aggregates with the value obtained from the corresponding 2D images

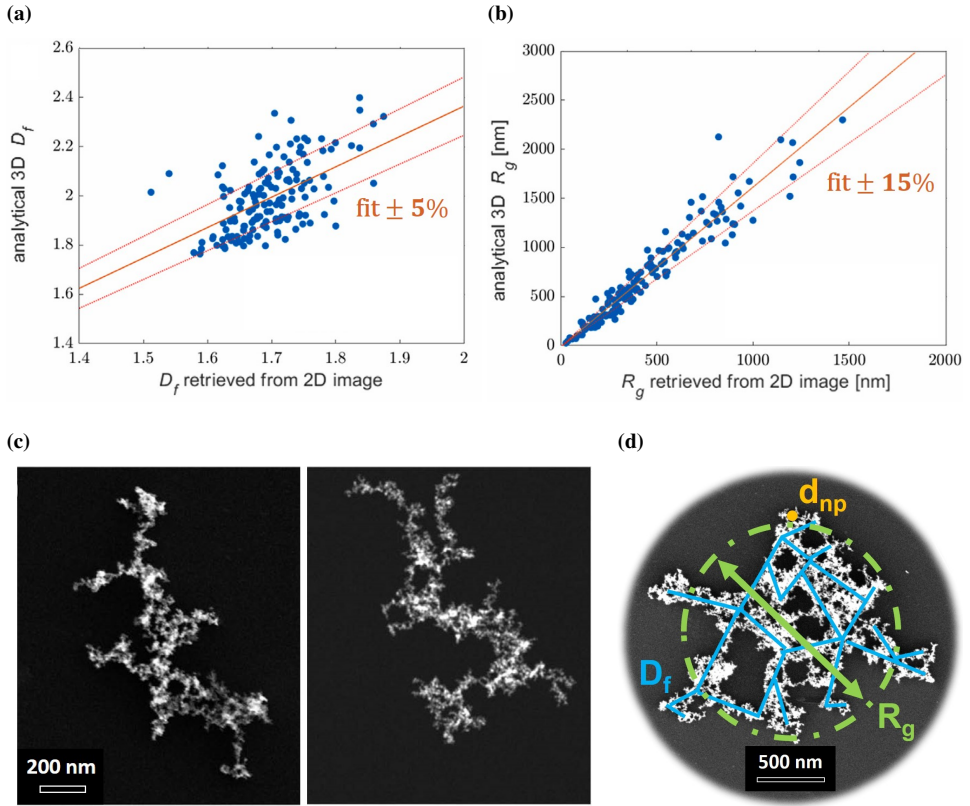


Figure 5.3: Calibration curves for the simulated aggregates for both D_f (a) and R_g (b), relating the analytical 3D aggregate properties with those derived by the corresponding 2D aggregate image; (c) Real aggregate SEM micrograph (left) and simulated aggregate image (right), highlighting the great visual similarity; (d) Visual representation of the three main fractal aggregate properties: d_{np} , R_g and D_f .

is devised: exploiting the knowledge of the aggregation mechanism [151], three-dimensional fractal aggregates are simulated, for which D_f and R_g can be computed analytically on one side and estimated from their 2D images (mimicking the SEM image acquisition process) on the other. The corresponding calibration curves obtained are shown in Figure 5.3a and 5.3b, while Figure 5.3c depicts side by side real and simulated aggregates. For fractal dimension determination from 2D images, a box counting method is employed (after image binarization) [181]: relating the number of nanoparticles in each cell to the size of the cell it is possible to estimate the self-similarity of the structure at different spatial scales, which is the definition of a fractal. The gyration radius is calculated as the equivalent radius of a circle with area equal to the aggregate area, again obtained from the bina-

Chapter 5. Carbon nanofoam production through ns-PLD and fs-PLD

rized SEM images. Exploiting the calibration of Figure 5.3a and 5.3b, the 2D values are traced back to an estimation of the real 3D value.

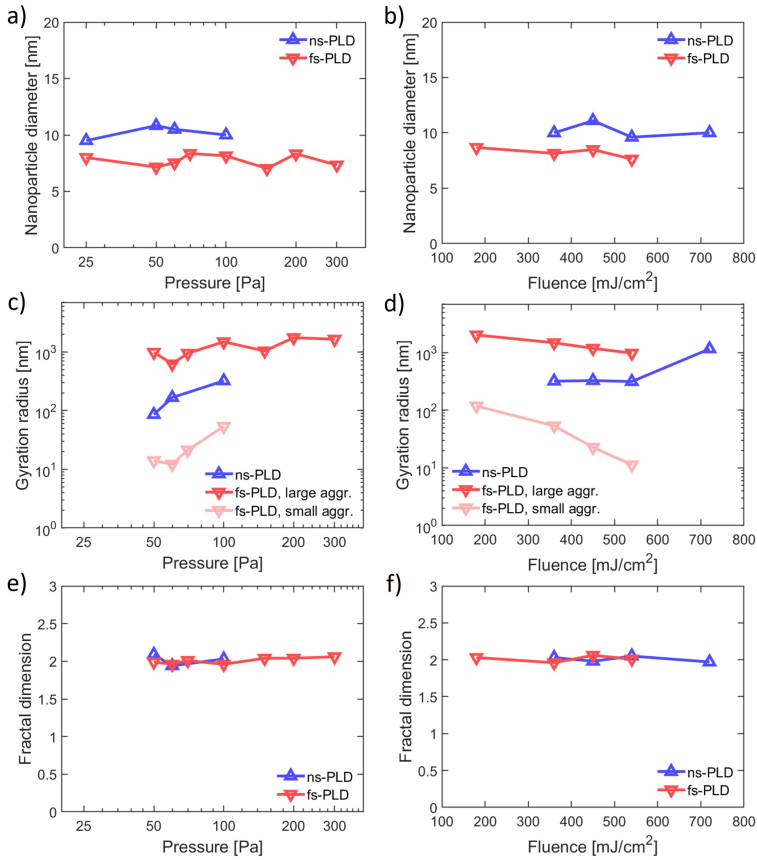


Figure 5.4: Results of the quantitative aggregate analysis over nanoparticle diameter (a, b), gyration radius (c, d) and fractal dimension (e, f). On the left (a, c, e) they are plotted as a function of the argon pressure, with a constant fluence of 360 mJ/cm²; on the right, as a function of the fluence (at a pressure of 100 Pa). For fs-PLD, the larger micrometric aggregates and the smaller background aggregates are plotted separately. Only single nanoparticles are present at 25 Pa, therefore no data on gyration radius or fractal dimension is reported. The uncertainty can be estimated as 10% for n_p , 15% for R_g and 5% for D_f .

The results of the quantitative aggregate study, obtained through analysis of the respective SEM images, are reported in Figure 5.4, investigated in relation to laser fluence, argon pressure and ablation regime. From the top panels, it is clear that no substantial dependence of the nanoparticle size on the investigated parameters is found, hinting at an independent nanoparticle formation mechanism. Only the ablation regime leads to a consistent

difference, with a d_{np} around 10 nm for ns-PLD and 8 nm for fs-PLD. An interesting effect is the absence of nanoparticles in vacuum conditions, which is indeed expected for ns-PLD (nanoparticles are formed thanks to the interaction with the background gas) but surprising for fs-PLD, for which the direct emission of nanoparticles and large atomic cluster is a well-known behaviour.

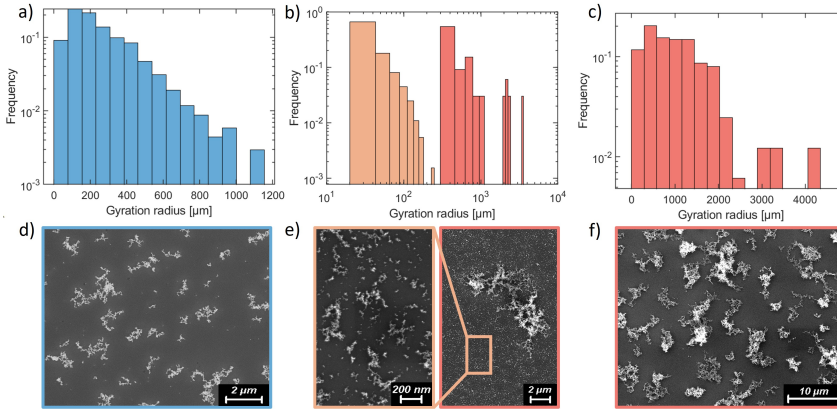


Figure 5.5: Characteristic distributions of aggregates gyration radii (a, b, c) shown with the corresponding SEM micrographs (d, e, f). In (a, d) the exponential distribution typical of ns-PLD is shown; in (b, e) the corresponding fs-PLD sample under the same deposition conditions (360 mJ/cm² and 100 Pa) highlights the presence of a double aggregate population. The last kind of observed aggregate distribution, peaked instead of exponential, is shown in (c, f). All distributions are normalized (each one independently in the case of the double population case).

Regarding the gyration radius, it is worthwhile to consider in greater detail the possible variations in its distribution (Figure 5.5): ns-PLD samples generally show great variability in sizes, well described by an exponential distribution (a, d), while for fs-PLD two separate population are found, large micrometric aggregates along a background of smaller aggregates (b, e). It should be noted that the background population of fs-PLD is itself exponential, hinting at similarities in the aggregation mechanism with ns-PLD. The last kind of distribution observed (c, f) is typical of fs-PLD at higher pressures or ns-PLD at high fluence, with reduced variability in gyration radius and thus peaked distribution.

In the middle panels of Figure 5.4, the average of the whole distribution is reported, separating multiple population where appropriate. The results consolidate the qualitative analysis of Figure 5.1 and 5.2: the main effect of argon pressure is to increase aggregate size, both for ns-PLD and the background population of fs-PLD, while the effect is less clear for the large

micrometric aggregates of fs-PLD. The laser fluence has no effect on the ns-PLD aggregates gyration radius excluding 720 mJ/cm^2 , where a sharp increase is observed. On the contrary, both aggregate populations in fs-PLD show a decrease in gyration radius with increasing fluence, more evident for the background aggregate population.

The fractal dimension, as demonstrated by the bottom row of Figure 5.4, is essentially constant regardless of pressure, fluence or ablation regime. Moreover, the specific value $D_f \approx 2$ is in-between the two well-known regimes of diffusion-limited cluster-cluster aggregation (DLCA, $D_f \approx 1.8$) and reaction-limited cluster-cluster aggregation (RLCA, $D_f \approx 2.1$) [182]. Therefore, a hybrid RLCA/DLCA mechanism could be well suited to describe the experimental results, in the whole range of investigated deposition parameters.

5.2 Morphological analysis

After having performed a detailed investigation into the aggregate properties, it is of certain interest to study the corresponding nanofoams—obtained by increasing the deposition time to 10 minutes—and the influence of pressure, fluence and ablation regime on their properties. The same set of deposition conditions are exploited, allowing a direct comparison between aggregates (Figure 5.1 and 5.2) and grown nanofoams (Figure 5.6 and 5.7 respectively).

In the case of depositions performed under vacuum conditions ($< 10^{-3}$ Pa), coherently with the previously highlighted absence of nanoparticles, compact near-bulk density films are obtained with both ns and fs-PLD (not shown). Without a background atmosphere, the ablated species are free to travel unrestricted toward the substrate, reaching it with high energy and giving rise to a compact film. The presence of a background gas, instead, can slow the ablated species through collisions, favouring their aggregation and reducing their energy upon reaching the substrate, both of which lead to the emergence of increasingly porous structure as the pressure increases. At 25 Pa (first column of Figure 5.6) the pressure is not high enough to effectively slow the ablated species, which reach the substrate mostly in the form of nanoparticles (first column of Figure 5.1), thus nanoparticle-assembled compact films are grown. By increasing the pressure, a sharp transition to a foam-like morphology is seen in ns-PLD, already evident from the 50 Pa sample. In the case of fs-PLD the transition is gradual instead, with a brief pressure interval in which compact structured and foam-like aggregates co-exist in the same film (at 50 Pa for instance). This peculiar morphology can be explained in light of the double aggregate population of fs-PLD, with the smaller background aggregates arriving on the substrate as energetic single

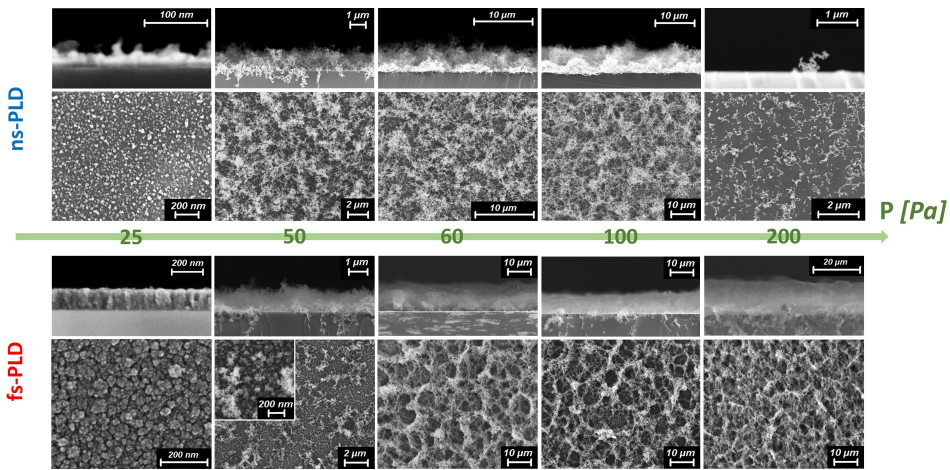


Figure 5.6: SEM images of the nanostructured films obtained at different pressure conditions, for both ns-PLD (upper panels) and fs-PLD (lower panels). The fluence and deposition time are the same for all samples (360 mJ/cm^2 and 10 minutes respectively). For each sample both a plane view (below) and a cross section (above) are depicted. A higher magnification inset is included for the fs-PLD sample at 50 Pa to highlight its peculiar morphology.

nanoparticles (or small nanoparticle clusters) together with the larger micrometric fractal aggregates. When the pressure reaches 60 Pa, mixed deposits give way to proper nanofoam, despite the continuous presence of the double aggregate population up to 100 Pa (Figure 5.1): as the pressure increases, the fraction of ablated species reaching the substrate as single nanoparticles reduces significantly, as demonstrated by the increase of background population aggregate size in these conditions. Interesting to note is the overall difference in morphology between the two techniques: ns-PLD leads to sponge-like structures, while the fs-PLD foam structure is web-like with larger voids. The fs-PLD sample at 200 Pa appears as an exception, with a structure closer to that of ns-PLD, and indeed it corresponds to a single population of larger fractal aggregates (Figure 5.1), leading to the hypothesis that the web-like structure of fs-PLD is caused by the double aggregate population. Within fs-PLD, no other variation in foam morphology is evidenced, while for ns-PLD an interesting feature appears: the increase of background gas pressure leads to analogous morphological features, but at a longer spatial scale (evident in the shortening of the scalebar from the 50 Pa to the 100 Pa sample). This effect can be correlated to the increase in aggregate size, and possibly also to the larger foam thickness observed for the higher pressure samples. For a pressure of 200 Pa, no film is grown on the substrate, and only single aggregates are present. The cause is probably

Chapter 5. Carbon nanofoam production through ns-PLD and fs-PLD

found in the complex ablated species motion along the background gas flux, that can hinder their ability to reach the substrate. The issue is absent for fs-PLD, since the depositions were carried out in static vacuum.

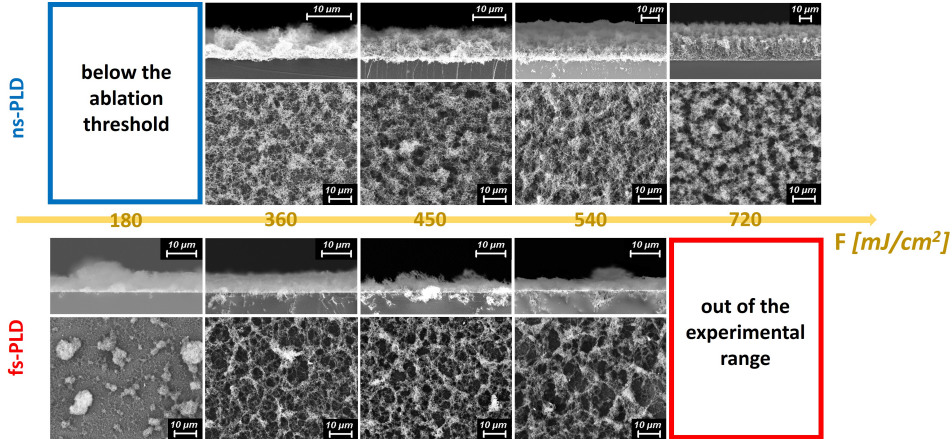


Figure 5.7: SEM images of the nanostructured films obtained at different fluence conditions, for both ns-PLD (upper panels) and fs-PLD (lower panels). The argon pressure and deposition time are the same for all samples (100 Pa and 10 minutes respectively). For each sample both a plane view (below) and a cross section (above) are depicted.

In Figure 5.7 the investigation in regard to the fluence is reported, showing a generally limited effect on the nanofoam morphology. The most significant impact is seen at 180 mJ/cm^2 : the fluence is below the ablation threshold for ns-PLD, and close to the ablation threshold for fs-PLD. The ensuing high instability in these deposition conditions leads to a strongly non-uniform film, with aggregates as large as 10 μm . The difference between the sponge-like morphology of ns-PLD and web-like structure for fs-PLD is confirmed.

In order to complete the morphological investigation, mass thickness maps of characteristic nanofoam samples were obtained, by exploiting the EDXS setup together with a theoretical electron and X-ray transport model (EDDIE [174]). Compared to the simple SEM images, mass thickness maps are useful to retrieve clear physical information, devoid of electron transport phenomena or post-processing that influence the intensity value of each SEM image pixel. Two nanofoam samples with the same average mass thickness ($\sim 5 \mu\text{g/cm}^2$) and density ($\sim 6 \text{mg/cm}^3$) are considered, one obtained with ns-PLD and the other through fs-PLD. The fluence is fixed at 360 mJ/cm^2 for both, while the argon pressure has to be higher for fs-PLD in order to achieve the same density than ns-PLD (200 Pa and 60 Pa are chosen respectively). The results are shown in Figure 5.8a, highlighting the different morphologi-

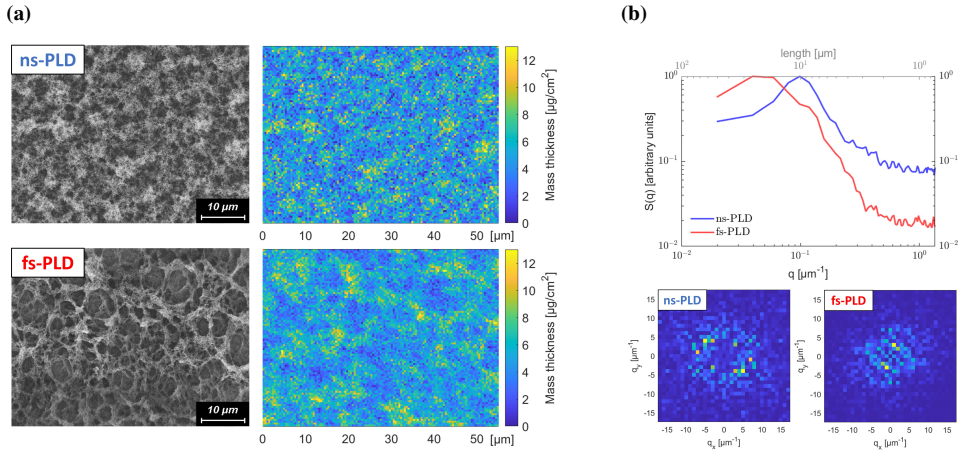


Figure 5.8: (a) Mass thickness maps (on the left) along with the corresponding SEM images (on the right), for ns-PLD (top row) and fs-PLD (bottom row) samples with analogous properties ($\sim 5 \mu\text{g}/\text{cm}^2$ average mass thickness and $\sim 6 \text{mg}/\text{cm}^2$ average density); (b) Central region of the Fourier transform of the mass thickness maps (bottom squares) and corresponding structure factor $S(q)$ (top graph) for both techniques.

cal features in the two regimes, such as the larger voids of the fs-PLD sample and the higher uniformity of the ns-PLD one. In order to retrieve quantitative information related to the structure uniformity at different spatial scales, the Fourier transform of the EDXS mass thickness images can be computed. From those, the structure factor $S(q)$ (where q is the spatial frequency) is the most relevant parameter to be extracted, being a quantitative measure of the most relevant spatial periodicity present in the image. $S(q)$ is equal to the square of the Fourier transform of the number density function, meaning that in this specific case it can be obtained as the squared Fourier transform coefficient of the mass-thickness maps averaged over the radius. Indeed, the nanofoam structure is disordered and non-uniform, with no preferential orientation, making the radial average a sound approach in determination of the structure characteristic periodicity. Considering the meaning of the structure factor, the frequency q corresponding to the maximum of $S(q)$ —or better, its reciprocal length $l = 1/q$ —can be taken as a measure of uniformity, being the most prominent length scale in the nanostructure mass distribution. With this interpretation, a longer l corresponds to a less uniform sample, and vice-versa. From Figure 5.8b, showing the results of this analysis, it is possible to retrieve the characteristic length scale, which is around $10 \mu\text{m}$ for ns-PLD and $20 \mu\text{m}$ for fs-PLD. This quantitative result confirms the qualitative observation of a higher uniformity for the ns-PLD nanofoam.

5.3 Raman analysis

Complementary to the morphological investigation, Raman spectroscopy can give information on the bond structure, particularly rich in the case of carbon. As for the previous analysis, the effect of argon pressure, fluence and ablation regime are investigated. The obtained spectra are reported in Figure 5.9, with arbitrary vertical offset for ease of visualization. The spectra present the typical features of disordered carbon materials, such as the broad G peak (around 1500 to 1600 cm^{-1}) and D peak ($\approx 1350 \text{ cm}^{-1}$) originated from the stretching of sp^2 bonds and breathing mode of the carbon atom rings respectively. Basing the analysis on the well-established interpretation proposed by Ferrari and Robertson [183], from the position of the G peak and the ratio between the D and G peak (I_D/I_G) it is possible to infer the structural disorder and clustering of the sp^2 phase, following a three-phase *amorphization trajectory* from crystalline graphite to tetrahedral amorphous carbon. (I) from bulk to nanocrystalline graphite the G peak upshifts toward 1600 cm^{-1} , and the D peak start to appear, both with relative narrow bands; (II) from nanocrystalline graphite to sp^2 amorphous carbon, with low sp^3 content ($< 10\%$), characterized by a softening of the G peak to $\approx 1510 \text{ cm}^{-1}$ and decreased I_D/I_G from ≈ 2 to ≈ 0 ; (III) transition from amorphous carbon to tetrahedral amorphous carbon (high sp^3 content, up to 85%) where the G peak comes back to $\approx 1580 \text{ cm}^{-1}$ with $I_D/I_G \approx 0$.

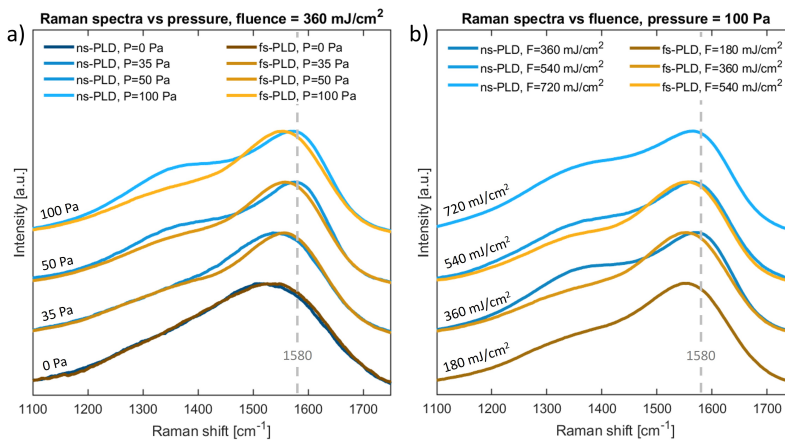


Figure 5.9: Normalized Raman spectra of ns-PLD samples (blue/cyan lines) and fs-PLD samples (orange/brown lines). The dashed grey line is in correspondence with the G peak of graphite ($\approx 1580 \text{ cm}^{-1}$). (a) Investigation into the effect of the pressure, with fluence fixed at 360 mJ/cm^2 ; (b) investigation into the fluence effect, with a constant argon pressure of 100 Pa .

In order to retrieve the peak parameters, the Raman spectra were fitted (after background subtraction) with the sum of a Lorentzian function (for the D peak) and a Breit-Wigner-Fano function (for the asymmetric G peak), and the results on G peak position and peak ratio are reported in Figure 5.10. The films obtained in vacuum present very similar spectra for both techniques, with I_D/I_G close to zero and G peak around 1520 cm^{-1} . This corresponds to a typical sp^2 amorphous carbon, at the limit between stage (II) and (III). This is consistent with the presence of highly energetic ablated species, giving rise to an amorphous structure far from the thermodynamically stable allotrope (i.e. graphite). By increasing the pressure, the D peak grows in intensity and the G peak moves toward higher frequencies, coherently with increased ordering and the presence of graphitic sp^2 domains. In the conditions in which a nanofoam is obtained (above 60 Pa), the G peak position and I_D/I_G parameters stabilize around 1575 cm^{-1} and 0.5 for ns-PLD, and 1565 cm^{-1} and 0.35 for fs-PLD. This corresponds to a network of topologically disordered, almost pure, sp^2 graphitic domains. These results further support the nanoparticle formation mechanism proposed, in which the ablated species condensate and aggregate under the influence of the background gas. This is expected for ns-PLD, but the opposite is true for fs-PLD, where direct nanoparticle emission is generally considered the main mechanism. Consistently with the aggregate and morphological characterizations, the laser fluence has a minor influence on the material properties, as both G peak position and peak ratio are essentially constant in respect to fluence.

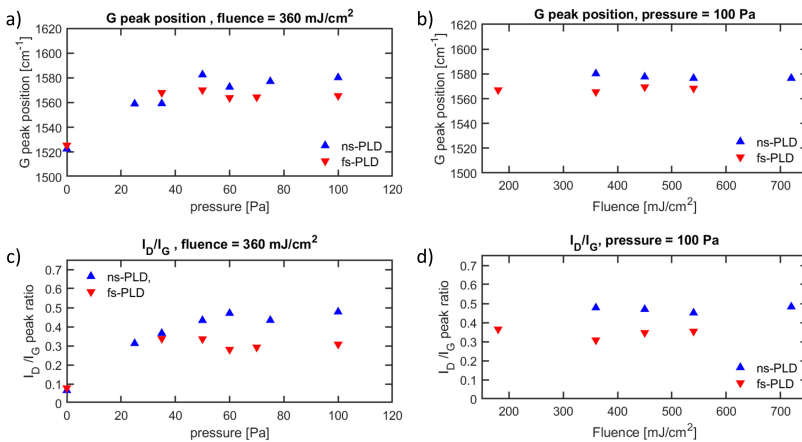


Figure 5.10: Position of the G peak (top) and intensity ratio of D peak over G peak (bottom) as a function of background argon pressure (left) and laser fluence (right).

Overall, comparing the results for the two techniques, fs-PLD present a consistently lower I_D/I_G ratio and lower frequency position of the G peak,

indication of a less topologically ordered structure than ns-PLD. Exploiting the relation proposed in [183], the average coherence length of sp^2 domains L_a can be estimated, as a function of the I_D/I_G ratio:

$$\frac{I_D}{I_G} = C'(\lambda_{exc})L_a^2 \quad (5.2)$$

C' is a proportionality constant depending on the excitation wavelength, equal to 0.0055 for 514 nm. The results are $L_a \approx 1nm$ for ns-PLD, and $L_a \approx 0.8nm$ for fs-PLD, in both cases exactly one order of magnitude lower than the typical nanoparticle size (10 and 8 nm respectively). This correlation can be explained with the hypothesis that the same number of sp^2 domains are present in each nanoparticle, suggesting that nanoparticle size is controlled by its local ordering and crystalline structure.

5.4 Average density characterization

The average density is one of the main macroscopic nanofoam characteristics, which through the PLD technique can be tuned in a wide experimental range. The density measurement is performed by combining the average mass-thickness retrieved from the EXDS data (with the aid of a X-ray transport model and the EDDIE method [174]) with the geometrical thickness measured through cross section SEM images. The results, showing the density dependence on argon pressure and fluence in both deposition regimes, are depicted in Figure 5.11. For the compact carbon films obtained in vacuum, the density is close to the bulk one as expected ($\approx 2.2 \text{ g/cm}^3$), for both techniques. As the pressure is increased, the reduction in density follows the morphological evolution, as the greater film porosity is the main driver for density reduction. At 25 Pa, where the films are still compact and nanoparticle-assembled, the density does not decrease significantly. From 30 Pa and onwards, however, a sharp decrease in density (emphasis on the log-log scale of Figure 5.11a) corresponds to the sharp morphological transition to foam-like structure, after which the density stabilizes around typical foam values (a few mg/cm^3). Comparing ns-PLD and fs-PLD, it can be noticed the shift toward higher pressures of the fs-PLD curve, coherently with the higher energy of ablated species and thus higher pressure conditions needed to obtain analogous morphologies (and thus densities).

A further observation is related to the sharp density transition in the intermediate regime: such a strongly nonlinear behaviour can find its origin in the aggregation mechanism, and specifically in the balance between ablated species energy and slowing efficiency of the background gas. If one predominates over the other, compact films or nanofoams are obtained re-

5.4. Average density characterization

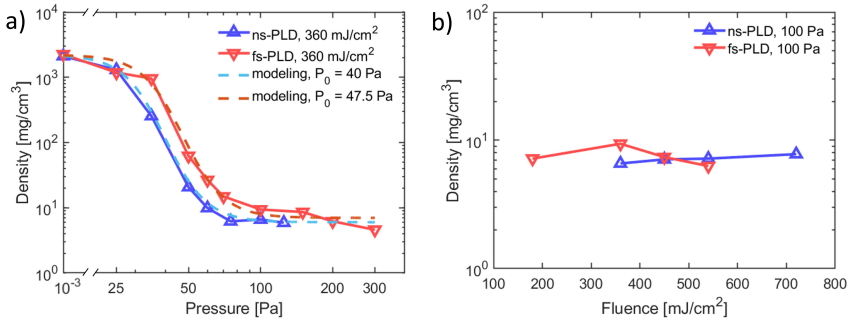


Figure 5.11: Average density of the carbon films and nanofoams deposited with ns-PLD (in blue) and fs-PLD (in red). (a) Density evolution over argon pressure, at 360 mJ/cm²; the dotted lines are obtained via Equation 5.3. (b) Density evolution over laser fluence, at a pressure of 100 Pa.

spectively, when virtually no ablated species or all of them are slowed to a diffusive regime (and thus the pressure dependence is weak). Only when the two are closely balanced, even slight pressure variation can have great effect on the film porosity and density. Considering the similarity of the pressure behaviour between ns and fs-PLD, a model for the average film density evolution as a function of the pressure is proposed. Due to the steep density gradient, a sigmoidal function in logarithmic scale is chosen, with the aim to fit the experimental behaviour:

$$\rho(P) = \rho_b \exp \left[-A \frac{P^k}{P^k + P_0^k} \right], \quad A = \ln(\rho_b / \rho_f) \quad (5.3)$$

where ρ_b is the graphite bulk density, P_0 is the characteristic pressure value at which the transition from compact films to nanofoams takes place, k a fit parameter accounting for the steepness of the transition, and ρ_f the foam density obtained in high pressure conditions. The dotted lines corresponding to Equation 5.3 in Figure 5.11 show excellent agreement with the experimental data points, if the suitable parameters are chosen: $P_0 = 40 \text{ Pa}$, $\rho_f = 6 \text{ mg/cm}^3$ for ns-PLD, $P_0 = 47.5 \text{ Pa}$, $\rho_f = 7 \text{ mg/cm}^3$ for fs-PLD, with $\rho_b = 2.2 \text{ g/cm}^3$ and $k = 5$ in both cases.

On the other hand, as evidenced by Figure 5.11b, the laser fluence has no significant effect on the nanofoam density for either technique, consistently with all previous results.

Taking advantage of the aggregate analysis of Section 5.1, and considering they are the building blocks of nanofoam materials, it is certainly worthwhile to investigate whether it is possible to connect the aggregate properties to the nanofoam density. The simplest way to do so is to relate the nanofoam

density to the aggregate density, which can be expressed as a function of the three main aggregate properties (d_{np} , R_g and D_f) exploiting the fractal scaling law (Equation 5.1):

$$\rho_{th} = \rho_{np}k \left(\frac{d_{np}}{2R_g} \right)^{3-D_f} \quad (5.4)$$

where ρ_{np} is the nanoparticle density and k a proportionality factor depending on many contributions, including the way the aggregate pack together in the foam structure and the details of the aggregation physics. In light of the results on the aggregate analysis in Section 5.1, both the fractal dimension and aggregate size do not significantly vary within the range of parameters considered, therefore the main parameter governing the foam density is the gyration radius.

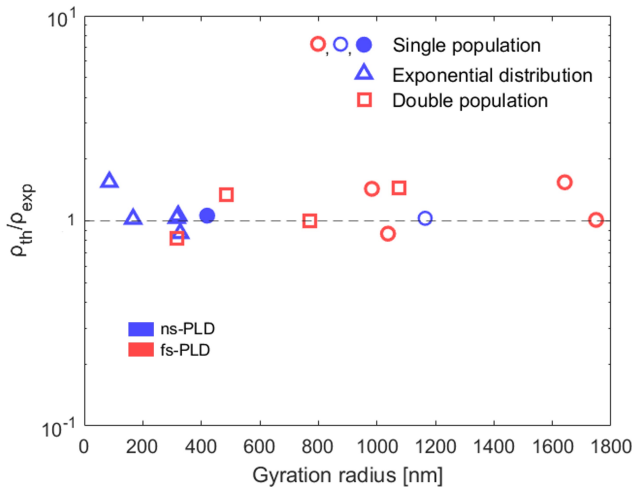


Figure 5.12: Relation between the theoretical carbon nanofoam density (calculated from the aggregate properties thanks to the fractal scaling law) and the experimentally measured value, represented as a function of the gyration radius. ns-PLD samples are reported with a blue color, and fs-PLD ones in red. The shape of the marker distinguishes the aggregate R_g distributions: triangles for exponential distribution (left column of Figure 5.5), circles for peaked single population distributions (right in Figure 5.5) and squares for double population (center panels in Figure 5.5). The filled circle refers to a carbon nanofoams from a previous work [151], obtained under 1.2 J/cm² and 700 Pa.

In Figure 5.12 the ratio of the theoretical density thus calculated over the experimental value is shown for many nanofoam samples obtained under a variety of conditions (ρ_{np} is estimated as equal to the graphite bulk density, 2.2 g/cm³). For the samples with a narrow aggregate distribution (nearly monodisperse population, corresponding to the circles in the image)

a value of $k = 1$ leads to a great agreement between theoretical prediction and experimental value. Notably, this holds also for samples obtained in quite different experimental conditions (1.2 J/cm² and 700 Pa from a previous work [151]), shown as a solid blue circle in the image. This is consistent with the hypothesis of a foam density well approximated with the aggregate density in these conditions. The same is true for the double population samples (squares in the image) if the gyration radius is calculated as the arithmetic mean between the value corresponding to each population. In the case of an exponential population, instead, a good agreement is found for $k = 0.18$, significantly different from unity: this means that in this case the aggregate density is no longer a good approximation for the foam density, likely due to the great variability in aggregate size and the effect that this has on their aggregation while growing the nanofoam. In summary, while Equation 5.4 can be exploited to relate the aggregate properties (nanoparticle radius, gyration radius and fractal dimension) to the nanofoam density, Equation 5.3 describes the density evolution depending on the background argon pressure. Therefore, the two can be combined to a single expression, able to derive the nanofoam density from the properties of the corresponding aggregates ($d_{np,f}$, $R_{g,f}$ and $D_{f,f}$):

$$\rho(P) = \rho_b \left(\frac{d_{np,f}}{2R_{g,f}} \right)^{(3-D_{f,f}) \frac{P^k}{P^k + P_0^k}} \quad (5.5)$$

In conclusion, through an extensive investigation on the pulsed laser deposition of carbon nanofoam, together with a complete characterization of the resulted material, the role of the main process parameters (background gas pressure, fluence and pulse duration) is highlighted. Thanks to the characterization of both aggregate and nanofoam properties, insights into the aggregation mechanisms were obtained, showing how the nanofoam structure is determined by the fractal aggregate properties. The aggregate themselves are composed of nanoparticles close to 10 nm in size independently on fluence and pressure, constituted of ≈ 1 nm topologically disordered nearly pure sp² domains. The background gas pressure is the deposition parameter with the greater influence on nanofoam morphology and properties, being also the parameter controlling the fractal aggregates gyration radii. Significant differences in the aggregate size distribution between ns-PLD and fs-PLD are evidenced, with an exponential distribution for the former and a double population for the latter. Despite the differences in ablation processes, the aggregate fractal dimension was found to be ≈ 2 under all conditions, evidence of an analogous aggregation mechanism: a hybrid diffusion-limited and reaction-limited cluster-cluster aggregation process taking place

while the ablated species are travelling toward the substrate. The average nanofoam density is derived from the fractal aggregate properties in a range of experimental conditions, and its evolution depending on the background gas pressure is described. Moreover, the nanofoam uniformity is characterized thanks to a 2D Fourier transform method, showing the greater uniformity of ns-PLD nanofoams. This paves the way for the production of nanofoams with controlled properties, such as density and uniformity, as required by applications. fs-PLD can represent a suitable complementary technique to ns-PLD, able to enlarge the parameter space (in terms of density, morphology and spatial uniformity) further consolidating the versatility of PLD approaches in growing finely tuned nanostructured materials.

CHAPTER 6

Versatile nanofoam synthesis through fs-PLD

The study of carbon nanofoams of Chapter 5 was of certain interest as a first step for testing the capabilities of the unconventional fs-PLD technique, basing the investigation on a well-known material (carbon) and exploiting the comparison with the well-established ns-PLD technique. In this Chapter, the potential of fs-PLD is explored for what concerns the synthesis of nanofoams of different elements, exploiting the universality of the ultrafast ablation mechanism. Boron (B), silicon (Si), copper (Cu), tungsten (W) and gold (Au) are investigated, chosen for their wide range of physical properties—both metals and semiconductors, low-Z and high-Z, with varied densities and melting temperatures—as well as their applicative interest: boron for laser-driven proton-boron fusion, gold for inertial confinement fusion, tungsten for plasma-wall interaction studies in magnetic confinement fusion, gold and copper for catalytic applications. Moreover for some of these elements (i.e. boron and metals) the production of nanostructured foams of low density and high thickness is especially challenging or not feasible with other techniques, including conventional ns-PLD.

As the background pressure has been identified as the parameter with greater effect on film morphology and density in the case of carbon nano-

foams, the first step is the study of its effect on morphological evolution for the different elements, to identify the optimal conditions for nanofoam growth. A detailed morphological investigation on a subset of the explored elements (i.e. boron, copper and tungsten) is performed, with the results reported in Section 6.1. Exploiting the insights obtained from this first analysis, low density nanofoams of all the elements are successfully produced, with special attention to their morphology both at the micro and nanoscale, uniformity, thickness, growth rate and oxygen content (Section 6.2). The nanofoams average density characterization, of significant interest also in view of laser-matter interaction applications, is described in Section 6.3, along with its evolution in function of the background pressure. A model of the behaviour based on the interplay between nanoparticle properties and slowing efficiency of the background gas is also proposed, coherently with the film morphological features and their link with the average density. The results are finally compared with the case of carbon, highlighting its unconventional behaviour. This work has been published in the *Small Structures* journal with the title “Versatile Synthesis of Nanofoams through Femtosecond Pulsed Laser Deposition” [184].

The fs-PLD setup is the same previously exploited for carbon nanofoam production, described in Section 4.2. The laser fluence is fixed at a value of 110 mJ/cm^2 for all samples, obtained through 3.8 mJ pulse energy on target on a 0.88 mm spot diameter. (100) silicon wafers are exploited as substrates, and the target to substrate distance kept fixed at 3 cm. Argon is used as background gas, and every deposition (except those in vacuum conditions, $< 10^{-3} \text{ Pa}$) is carried out in static vacuum, from 50 to 5000 Pa.

6.1 Morphological characterization

Considering the specific conditions needed for the nanofoam morphology to arise—namely ablated species slowed down to diffusive conditions, thus able to aggregate in fractal structures while in flight—it is of certain interest to test whether this can happen regardless of the material considered, and under which conditions. Boron (low-Z), Copper (mid-Z) and Tungsten (high-Z) are chosen for this first morphological analysis, two metal and a metalloid (boron) with a range of physical and chemical properties. Figures 6.1 and 6.2 report the result of the morphological investigation, as plane view and cross section SEM images respectively (the deposition time is 10 minutes for all samples). The film average density, investigated in detail in Section 6.3 is also reported here. A first observation is that nanoparticle-assembled films are obtained in all pressure conditions, from vacuum ($< 10^{-3} \text{ Pa}$) to hundreds of thousands of Pa of argon; at the same time, the general morpholog-

6.1. Morphological characterization

ical evolution is similar for all elements, going from compact nanoparticle-assembled films to tree-like structures and finally to nanofoams.

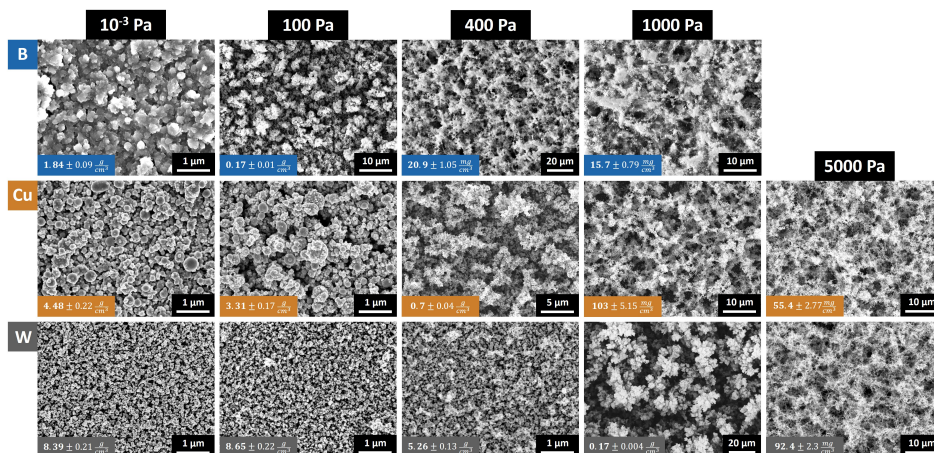


Figure 6.1: Top-view SEM micrographs of boron (top row) copper (middle row) and tungsten (bottom row), showing their morphological evolution with increasing background argon pressure (from vacuum conditions up to 5000 Pa). The average film density is also reported (refer to Section 6.3 for more details). Take note that the magnification is not homogeneous among all the samples, rather the most appropriate magnification to highlight each sample's morphological features was chosen.

In vacuum conditions the morphology is compact nanoparticle-assembled films in all cases, consistently with the direct nanoparticle synthesis typical of fs-PLD. The nanoparticles themselves are close to spherical for copper and tungsten, with partially melt appearance (particularly clear from the cross-section images), while more irregular in shape for boron. This leads to an apparently more compact morphology in this last case. The size of the nanoparticles is also different, being noticeably smaller for the case of tungsten. Considering the compact morphology, the material density is expected to be not so far to the bulk one, reduced only by the porosity inherent to a nanoparticle-assembled film. Indeed, the boron film density is 1.84 g/cm^3 (corresponding bulk density 2.3 g/cm^3), while for copper and tungsten the film density is about half of the bulk (4.48 and 8.39 g/cm^3 respectively). When a small amount of argon is introduced in the deposition chamber, such as 100 Pa for copper and tungsten, minor but noticeable morphological changes can be evidenced: while the material density is not changed substantially (slightly decreased for copper and slightly increased for tungsten) the average nanoparticle dimension is decreased, and the smaller nanoparticles are found decorating the surface of larger ones.

Chapter 6. Versatile nanofoam synthesis through fs-PLD

This is especially evident in the case of copper, leading to a larger porosity and thus explaining the lower density. The small density increase in the case of tungsten (while inside the experimental uncertainty) could be explained by the tighter packing allowed by a lower nanoparticle size, together with the absence of an increased porosity.

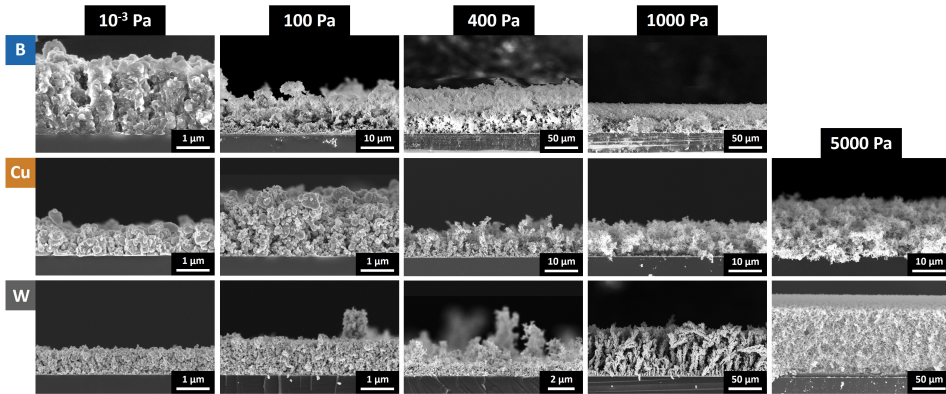


Figure 6.2: Cross section SEM micrographs corresponding to the same samples of Figure 6.1, depicting the morphology evolution of boron (top row) copper (middle row) and tungsten (bottom row) samples obtained with increasing background argon pressure (from vacuum conditions up to 5000 Pa). As above, the magnification is not homogeneous, but chosen to highlight each sample's morphological features.

Further increasing the background pressure leads to substantial morphological changes, as highlighted in the films obtained at 100 Pa for boron, 400 Pa for copper and 1000 Pa for tungsten. As seen from both top-view and cross section images, the film growth is highly directional, with tree-like or cauliflower-like structures, with substantial porosity and significantly lower density (in the order of 0.1-1 g/cm³). Considering the high growth directionality, the higher deposition rate of tungsten can be the origin of the apparently different morphology seen in the cross section of the 1000 Pa sample. At the same time, the plane view of the three films present analogous morphological features, despite at different spatial scales (note the different scale bars). Finally, a last substantial morphological transition takes place by further raising the pressure, above 400 Pa for boron, 1000 Pa for copper and 5000 Pa for tungsten, with the emergence of the nanofoam morphology. As the top views of Figure 6.1 demonstrate, the void fraction increases dramatically, bringing the density down to 10-100 mg/cm³. An interesting observation is connected to the appearance of the nanofoam morphology: only when the pressure is high enough to promote nanofoam formation, significant light emission/scattering along the laser path can be seen, similar to what happens

when light travels in a dusty environment or through vapour. This could be an indication of a high concentration of nanoparticles and aggregates in the deposition chamber atmosphere, enough to absorb a small fraction of the laser energy and re-emit through de-excitation. No samples for boron at 5000 Pa is reported, since in those conditions the plume confinement is too high, strongly reducing the deposition rate and not allowing the growth of a film—indeed, most of the ablated species redeposit in the vicinity of the target (a similar effect was evidenced in the case of carbon nanofoams in the previous Chapter).

Comparing the different element behaviour, it is interesting to note the analogous morphological evolution in all three cases, from nanoparticle-assembled compact films to tree-like/cauliflower-like morphologies and finally nanofoams. The main differences are related to the pressures corresponding to these morphological transitions, lower for boron, intermediate for boron and higher in the case of tungsten. This can be visualized by realizing the morphological similarities in the upper-left lower-right diagonals of Figure 6.1, such as the 100 Pa boron, 400 Pa copper and 1000 Pa tungsten samples.

Another morphological information that can be derived from Figure 6.1 is related to the nanostructure uniformity at the nano and microscale. In the previous investigation of carbon nanofoams (Chapter 5), EDXS maps and image analysis methods based on Fourier transform were exploited, which were nevertheless in great agreement with the qualitative morphological investigation. For the scope of this analysis, the qualitative description is more than adequate. For the nanoparticle-assembled films obtained in vacuum conditions, the uniformity is a direct consequence of the nanoparticle size, leading to a higher uniformity for tungsten films (smaller nanoparticles). The intermediate tree-like and cauliflower-like films are the most varied, with also the possibility of presenting mixed morphologies: the 100 Pa boron film is an example, with a tree-line morphology near the substrate and cauliflower-like structures on top of it (Figure 6.2). In these conditions, the uniformity is strongly related to the film morphology: the 400 Pa copper sample is the most uniform, due to the more compact structures, followed by the mixed morphology of the 100 Pa boron sample; finally, the strongly anisotropic growth of the 1000 Pa tungsten sample leads to the lower uniformity. This uniformity variation is reflected into the chosen magnification for the three samples in Figure 6.1, able to display the most significant morphological features: 10000 X for copper, 5000 X for boron and 2000 X for tungsten. Finally, nanofoams present the lowest uniformity, due to the large-scale structures and wide voids. No great uniformity variation with increasing pressure or among the different elements are evidenced, indication

of an analogous aggregation and growth mechanism.

6.2 Thickness evolution and deposition rate

Exploiting the in-depth morphological investigation of Section 6.1, it was possible to produce nanofoam films from a variety of different elements, adding silicon and gold to the boron, copper and tungsten previously considered. Beside their applicative interest, silicon and gold (a low-Z semiconductor and a high-Z noble metal) were chosen to widen the investigated parameter space as far as material properties are concerned. As clearly demonstrated in Figure 6.3, highly porous nanofoams can be obtained in all cases, with analogous morphology composed by disordered fractal-like structures, with nanoparticles as their basic constituents. The corresponding pressure condition necessary, as demonstrated also by the previous morphological analysis, range from 400 Pa for boron to 1000 Pa for copper and gold, and 5000 Pa for tungsten. Silicon and gold nanofoams were also obtained with 1000 Pa of argon.

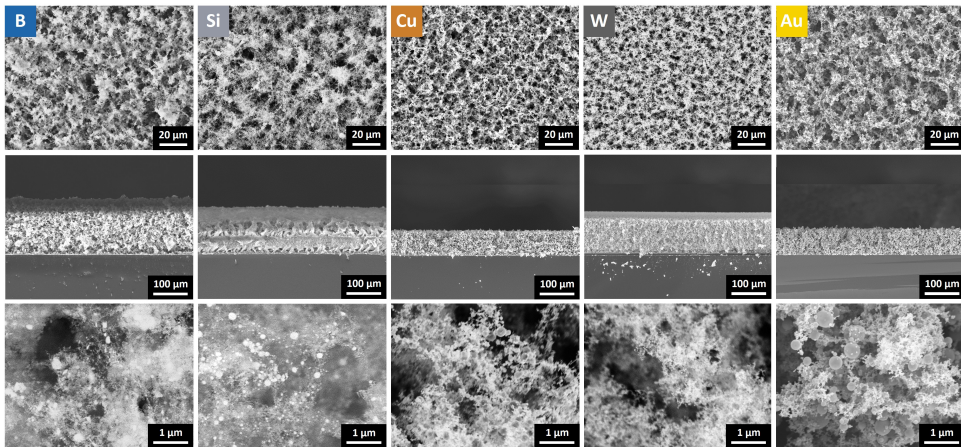


Figure 6.3: SEM micrographs of nanofoams of different element, obtained with fs-PLD (laser fluence 110 mJ/cm^2). Each column correspond to a different element, with the top-view in the upper panels, corresponding cross section in the middle and high magnification of the foam structure on the bottom. Note the nanofoam thickness, close or surpassing $100 \mu\text{m}$ for all elements. The background argon pressure is 400 Pa for boron, 1000 Pa for silicon, copper and gold, and 5000 Pa for tungsten.

Despite the same web-like morphology typical of the nanofoams at the multi-micron spatial scale (top panels of Figure 6.3) significant variations can be found in the nanostructure of the foam, both in nanoparticle size and their short scale (\sim nanometer) aggregation structure. Copper and gold

6.2. Thickness evolution and deposition rate

nanoparticles are spherical in shape, with a predominance of larger size nanoparticles (50-200 nm in diameter) particularly evident in the case of gold. The nanoparticles are arranged in chain-like structures or small compact aggregates. The nanoparticle dimension is smaller on average for boron and silicon, in the range of 10-50 nm, with most of the material in the form of small nanoparticles. They are connected in thin strands and fractal like aggregates, leading to the retention of the nanofoam structure (self-similarly) even at the nanometer spatial scale, giving the SEM image the typical hazy appearance due to electronic effects. Tungsten features are intermediate between the previous two: while the nanostructure is similar to that of copper and gold, the nanoparticles are smaller and more uniform in size, all below 50 nm.

An interesting notable feature is the possibility to obtain nanofoams of very different materials under the same fluence conditions (all samples of Figure 6.3 are obtained with 110 mJ/cm^2), confirming the universality and versatility of the fs-PLD technique. Moreover, the effective ablation threshold¹ of B, Si, Cu, W and Au is found to be quite similar: $\approx 18 \text{ mJ/cm}^2$ for copper and tungsten, $\approx 24 \text{ mJ/cm}^2$ for boron and $\approx 26 \text{ mJ/cm}^2$ for silicon.

As shown in Figure 6.4, the nanofoam thickness can be easily tuned by changing the deposition time accordingly, since the deposition rate is constant in time and no significant changes in density or morphology take place—of course, this is not valid for the earliest deposition stages, where only single aggregate are present on the substrate and no complete film is obtained. A significant consequence is the minimum nanofoam thickness achievable, which is the condition in which a full film is grown, and thus determined by the largest aggregate size: if the foam thickness is a couple of times higher than the largest aggregates (of micrometer size at most), a 5-10 μm uniform film with satisfactory coverage can be obtained. No hard cap over the maximum foam thickness is present, since an increase of deposition time leads to a linear increase in thickness. As shown by the cross sections of Figure 6.3, 100 μm can be readily reached for all elements considered. Nevertheless, the nanofoam structure does not possess great mechanical rigidity, making it prone to morphological rearrangements under external stresses. The issue worsens for higher thickness foams, thus a soft upper limit on achievable foam thickness (in the order of some hundreds of micrometers) is expected.

One of the advantages of the fs-PLD technique is its high deposition rate, thanks to the ultrafast ablation mechanism. From Figure 6.4, boron, silicon and tungsten all present a high deposition rate, in the order of 8-10 $\mu\text{m}/\text{min}$,

¹Operatively, the fluence at which an ablation plume starts to appear on the target in vacuum conditions.

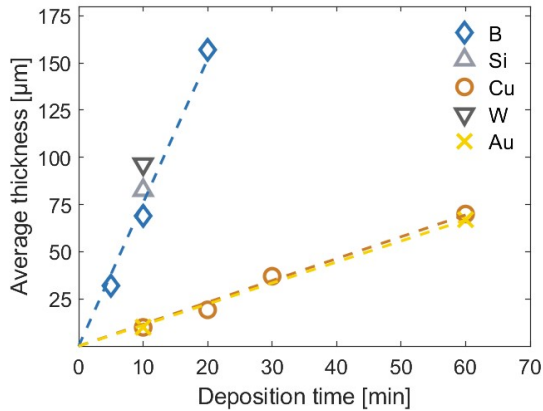


Figure 6.4: Deposition rate for the nanofoams of Figure 6.3, showing the whole thickness evolution for boron, copper and gold (along with a linear fit). A single data point for silicon and tungsten (10 minutes deposition time) is also reported as a comparison.

while it is lower for copper and gold (close to 1.1 $\mu\text{m}/\text{min}$). This is reflected in the deposition time necessary to obtain the nanofoam of Figure 6.3: 10 min for silicon and tungsten, 20 min for boron (resulting in a higher thickness) and 60 min for copper and gold.

One of the drawbacks of the production of highly porous nanostructured materials through PLD is the inevitable incorporation of oxygen, due to the substantial surface area of the foams. This is especially true for materials that can undergo oxidation (tungsten, copper, silicon) or are an efficient oxygen getter (boron). Through EDXS measurements, the oxygen content was close to 30% in atom for boron, silicon and tungsten foams, lower than 10% for copper and virtually absent in gold nanofoams. This considerations are also supported by the oxygen content of the more compact films obtained at lower pressure, where a much lower oxygen incorporation is demonstrated. No special care was taken in this work to avoid nanofoam air exposure, which could be one avenue to limit this issue for applications where high sample purity is required.

A final point worth mentioning is related to the nanofoam films macro-scale uniformity, that is the variation of film thickness over the deposition area in the case of larger substrates. Due to the higher directionality of the plasma plume, fs-PLD generally leads to lower uniformity films in respect to ns-PLD. In the case of nanofoams, however, the high plume confinement resulting from high background gas pressure conditions significantly mitigates the issue, allowing satisfactory uniformity on 5×5 up to 10×10 mm substrates. To completely negate the issue and uniformly coat large ar-

eas, appropriate substrate/target motion routines can be exploited, with the drawback of a lower total film growth rate.

6.3 Average density characterization and modeling

Considering the great importance of the nanofoams average density, and its correlation to the material morphology (as anticipated in Figure 6.1) its pressure evolution is reported in Figure 6.5. For the three elements investigated in more detail in the previous Sections (boron, copper and tungsten) the whole evolution is shown, while only the data corresponding to the nanofoam of Figure 6.3 is reported for gold and silicon. The data for carbon nanofoam from Chapter 5 is also shown to enrich the elemental analysis. The density is calculated as the ratio of mass thickness over geometrical thickness (measured from the cross-section SEM images). The mass thickness is obtained through the EDDIE method [174] based on EDXS data, except for silicon and tungsten samples: in the case of silicon, it is not possible to distinguish the X-ray coming from the film to those originating in the silicon substrate, both required for the EDDIE method. Similarly, the substrate X-ray are shielded by the high-Z (tungsten) foam, and are thus unable to reach the detector. To circumvent this issue, weight measurements of the films are exploited, by weighting the substrate before and after deposition. The density evolution is modeled with the same function exploited for carbon nanofoam, a sigmoidal function in log-log scale able to follow the steep density gradient:

$$\rho(P) = \rho_0 \left(\frac{\rho_f}{\rho_0} \right) \left[\frac{P^k}{P^k + P_0^k} \right] \quad (6.1)$$

The fitting parameters are the compact film density ρ_0 , the foam density ρ_f , the pressure corresponding to the center of the sigmoid P_0 (i.e. where the main morphological transition takes place) and the k parameter, measure of the steepness of the transition (a large k corresponds to greater density variations in a lower pressure range). In figure 6.5 the fit are shown as dashed lines in the graph on the left—showing excellent agreement with the experimental data—while the differences in the fit parameters among the elements are highlighted on the right. Thanks to the analysis of different elements, it is possible to better correlate the fitting parameters (and therefore the function behaviour) to the film morphological properties, but before doing that it is worthwhile to discuss more in detail the film growth process and its effect on material morphology.

In order to better interpret the morphological and density evolution with the background pressure, and the observed differences among elements, it

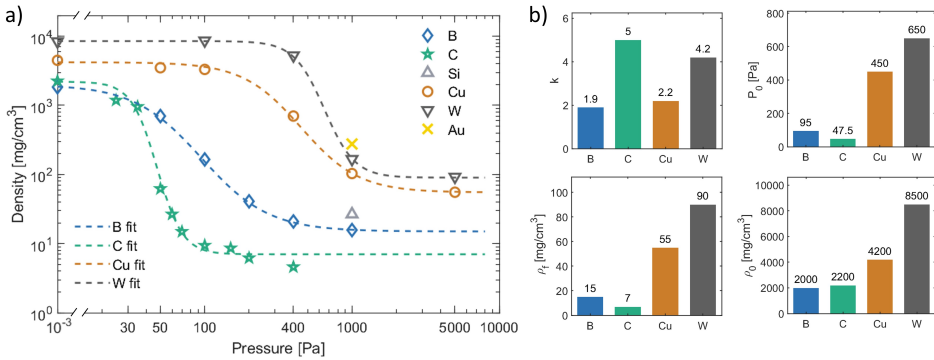


Figure 6.5: (a) Density evolution of the nanostructured film as a function of the background gas pressure for the different elements (for the sake of comparison, the data for carbon from the previous investigation is also included). The relative uncertainty on the data is estimated as 5% for tungsten, 8% for silicon and 10% for all the other elements. The dashed lines are the fit from Equation 6.1; (b) variation of the fit parameters (k , P_0 , ρ_f and ρ_0) among the different elements.

is of particular interest to consider a simple model of the process. As well-established from literature [185, 186] and confirmed by the observation of nanoparticle-assembled films in vacuum conditions, the ultrafast ablation process of fs-PLD leads to the direct production of cluster and nanoparticles, with sizes ranging from a few to a few hundreds of nanometers. It is then possible to model the ablated species as solid spheres of radius R and density ρ , emitted with a certain initial velocity v depending on the details of the ablation process. The effect of the background gas atoms or molecules, present in the deposition chamber, can be modeled as successive collision events, explaining the overall slowing down effect. Under the hypothesis of elastic scattering events, simple force balance considerations demonstrate a drag-like effect proportional to the initial velocity (in agreement with the more rigorous derivation of Epstein's relations [187]):

$$\dot{v} = -\gamma v, \quad \gamma \propto \frac{P}{R\rho v_t} \quad (6.2)$$

In this description, the drag factor γ is a measure of the slowing efficiency of the background gas, which is directly proportional to the pressure and inversely proportional to the radius and density of the nanoparticles. The last parameter is v_t , the thermal velocity of the background gas, which can be considered constant under the experimental conditions considered.

In vacuum conditions, the compact nanoparticle-assembled films are a consequence of the high energy and velocity of the ablated species, which

6.3. Average density characterization and modeling

are free to travel without interaction toward the substrate. The high energy of ablated species can be the reason for the partially melt appearance of the metallic films (Figure 6.2, and the more prominent effect for copper in respect to tungsten can be attributed to the lower melting temperature. Instead, the peculiar morphology of the boron film can be attributed to a different behaviour of metalloids compared to metals under ultrafast ablation. When a background gas is introduced in the deposition chamber, according to Equation 6.2, the nanoparticles start to be slowed, an effect that is greater for smaller nanoparticles with a lower density. While the density can be approximated to be the same for all nanoparticles (equal to the target density, considering the ultrafast ablation mechanism), the ablated species are emitted with a wide size distribution (see the bottom panels of Figure 6.3 for instance). This has important consequences on the whole process, since different nanoparticles will be slowed differently depending on their size, with influence on the resulting morphology. When a low argon pressure is present, it will not be sufficient to slow all the ablated species, but can have a higher effect on the smaller nanoparticles, which can then aggregate to each other or on the surface of the larger nanoparticles. The ablated species energy remains high, giving rise to a compact film, but with the first features of aggregation, as seen in the copper and tungsten films at 100 Pa of Figure 6.1 and 6.2. As the background pressure is raised further, most of the ablated species can be sufficiently slowed, while retaining a significant velocity component in the direction of the substrate. This gives rise to a ballistic aggregation mechanism [154, 188], with the characteristic directional growth and tree-like morphologies. At the same time, the smallest nanoparticles could be slowed to a diffusive regime at the same pressures, leading to larger aggregate formation. This can explain the wider morphological variation in this regime—including tree-like, cauliflower-like, and mixed morphologies with foam-like aggregates—but also the gradual morphological transition and the high sensitivity to small changes in background gas pressure. At the same time, the morphological transition can become sharper in the case of a mostly monodisperse nanoparticle size, as all nanoparticles would be slowed to a certain regime under the same pressure conditions. This can be the case for tungsten, where the more uniform nanoparticle size distribution (Figure 6.3) leads to the strongly directional tree-like morphology at 1000 Pa, in contrast with the mixed morphologies of 100 Pa boron or 400 Pa copper. By further raising the background pressure, a diffusive regime is finally reached for all nanoparticles, a condition in which the growth of larger fractal aggregates is promoted, and the porous foam morphology arise in the film as a result. Despite the many approximations of the model of Equation 6.2, it was especially useful in defining the most important parameters influencing

the ablated species dynamics—background gas pressure, nanoparticle size and density—that in turn are the foundation of the nanostructured material morphology and properties.

After all this considerations, it is possible to discuss more in detail the density evolution, and the differences between the elements considered, exploiting the fit parameters of Equation 6.1 in a quantitative description. The first point worth mentioning is the possibility to model the density evolution of all elements through the same function, indication of universal aggregation and film growth mechanisms. Thus, the general behaviour of the density evolution is the same in all elements considered, from high density compact films to porous low-density nanofoams, through a sharp density transition. This is mirrored on the morphological features of the films, going from compact films to tree-like or cauliflower-like morphologies to porous nanofoams. The link is not surprising, since the nanostructured material average density is the consequence of the nanoparticle density (that can be approximated with the material bulk density) together with their size and organization in space (i.e. the films morphology, determining the void fraction).

Despite presenting the same general behaviour, important differences can be highlighted between the different elements, quantitatively exploiting the value of the fit parameters shown in Figure 6.5b. Considering the P_0 parameter, it details the pressure at which the density (and morphological) transition takes place, thus can be taken as a measure of how easily the ablated species can be slowed down to comparable conditions by the background gas. More specifically, it is the center point of the sigmoid, corresponding to the pressure value able to at least partially slow down most of the ablated species. Considering the previous discussion, the nanoparticle size, velocity and density would have the most influence over the value of P_0 . Indeed, the larger nanoparticle size of copper corresponds to a higher P_0 in respect to boron, and the smallest nanoparticles of carbon result in the lowest P_0 . For the case of tungsten, P_0 is moderately higher than copper: the higher density and likely higher energy of ablated species (qualitatively demonstrated by a longer and more directional ablation plume at comparable pressure conditions) would go into the direction of a higher P_0 , partially moderated by the opposite effect of a smaller nanoparticle size. Secondly, all materials are composed by nanoparticles, therefore analogous morphologies formed by different elements would present different average densities in proportion to the single nanoparticle density. The different nanoparticle size is also a factor to be considered: even if the large-scale morphology is the same (e.g. nanofoam) larger nanoparticles would imply changes in the nanoscale morphology, leading to an increase in the average density. As an example, the smaller nanoparticle size of tungsten in respect to copper and gold

6.3. Average density characterization and modeling

can explain the moderate increase in average density from the copper to the tungsten samples at 5000 Pa, despite the great difference in bulk densities (8.96 against 19.3 g/cm³ respectively), and also the higher density of the gold foam at 1000 Pa despite the similar bulk density (19.32 g/cm³). Overall, the nanofoam density is a property emerging from the combined effect of nanoparticle size, their density and distribution in space (i.e. morphology). Indeed, the nanofoam density (as represented by the parameter ρ_f) changes among the different elements, mainly according to the variations in bulk density. The behaviour is thus similar to that of P_0 (clearly seen in Figure 6.5b), since they both depends in a similar fashion on the nanoparticles size and density. Finally, the k parameter defines the slope of the curve, with higher values corresponding to a sharper density transition. In light of the previous discussion, this can be linked to the ablated species size and energy uniformity: monodisperse nanoparticle populations will all be slowed in similar pressure conditions, leading to sharper gradients and a higher k . On the other hand, the presence of a wide distribution in nanoparticle sizes and/or velocities promotes the formation of intermediate morphologies and gradual morphological transitions. The lower k value of copper and boron, correlated with the emergence of intermediate morphologies, can be attributed to the wide nanoparticle size distribution, while the more uniform size distribution of tungsten and carbon is reflected in a higher k .

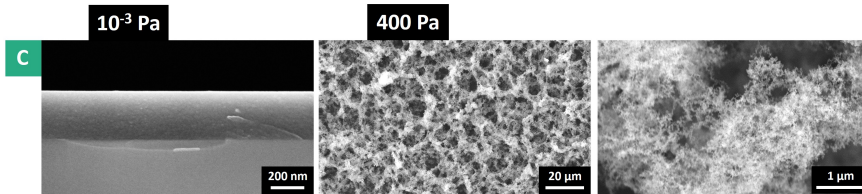


Figure 6.6: In the center panel, carbon nanofoam produced with fs-PLD at 400 Pa are shown, with higher magnification details on the right panel to highlight its nanoscale morphology. A cross section of the carbon compact film obtained in vacuum conditions is shown on the left.

The comparison with carbon, beside the previous considerations, is of particular interest for what concerns film obtained in vacuum conditions: while the general density behaviour is the same, and so is the nanofoam morphology (shown in the center and right panels of Figure 6.6) a substantial difference in respect to the other materials is seen in the film obtained under vacuum conditions. As shown in the cross section SEM image on the left of Figure 6.6, compact uniform films are obtained, instead of the nanoparticle-assembled films for all other elements. This is also reflected in the ρ_0 parameter, which is higher for carbon and equal to its bulk density

(Figure 6.5). This can be related to the nature of ablated species, which are not nanoparticles but atoms, ions or small clusters, uniquely for carbon if compared with the well-established direct nanoparticle emission typical of the ultrafast ablation mechanism. This could be related to the specific properties of the material, such as the absence of a liquid phase at normal temperature and pressure conditions, also in light of the partially melt appearance of the metallic nanoparticle-assembled films in vacuum. Thus, uniquely for carbon, the nanoparticles are not directly produced in the ultrafast ablation process but result from the interaction with the background gas, such as is the case for the ns-PLD technique.

In conclusion, fs-PLD is shown as a flexible tool for the production of nanostructured materials and nanofoams in particular, from a variety of elements with different characteristics. The background pressure is the main parameter that can be used to tune the material morphology, due to the interplay between the aggregate properties (dimension, density and velocity) with the slowing effect of the background gas (due to the gas pressure and thermal velocity). Low-density, high-void fraction web-like nanofoams can be consistently obtained under sufficiently high pressure conditions, regardless of the element, under the same fluence condition. This confirms the universality of the ultrafast ablation mechanism and paves the way to the production of mixed elemental films by codeposition.

Part III

Target production for laser-matter interaction experiments

CHAPTER 7

Carbon nanofoam Double-Layer Targets for particle acceleration

This first Chapter on the applications of nanostructured materials to high-intensity laser-matter interaction experiments focuses on nanofoam-based double layer targets (DLTs) for laser-driven particle acceleration. The experimental activity is performed in collaboration with the research group in charge of the VEGA 3 laser at the CLPU laboratories. The laser facility, along with the experimental setup and the aims of the experiment are described in Section 7.1. Section 7.2 is dedicated to target design and production, exploiting magnetron sputtering and PLD to entirely produce DLTs with the desired properties. Finally, preliminary results of the particle acceleration experimental campaign are reported in Section 7.3, with special attention to the target performance and future optimization, of great relevance for this thesis work.

7.1 VEGA 3 laser facility, experimental setup and goals

The experimental campaign at CLPU has multiple aims, the main one being the performance testing of single and double-layer targets on a petawatt-class laser for proton acceleration, in comparison with commercially available tar-

Chapter 7. Carbon nanofoam Double-Layer Targets for particle acceleration

gets. At the same time, other objectives are the test of a novel real-time proton detector prototype, and the production and detection of neutrons generated by the reaction of the laser-accelerated protons with a lithium-fluoride converter. As the most relevant for the topics of this PhD thesis work, this Chapter focus will be on the first and main objective.

During the experiment the VEGA 3 laser was able to provide 20 J pulses at 30-50 fs, with a laser spot size of 12 μm and resulting intensity exceeding 10^{20} W/cm². Another relevant laser feature, not always common in high intensity lasers, is the possibility to operate with high repetition rate, in the order of 300 shots a day. This has definite implications on the targets' requirements, as will be clear in the following Sections, as a multiple target design (or a single target able to withstand multiple shots) are needed. Generally, perforated target holders are employed, with two separate pieces (front and back) fastened together with the thin foil target in the middle.

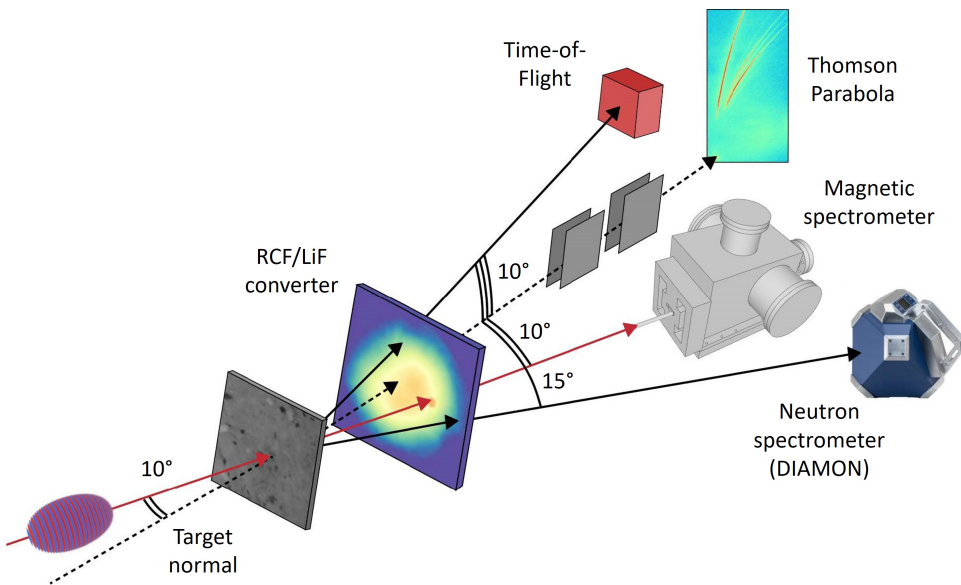


Figure 7.1: Scheme of the setup inside the VEGA 3 target chamber. The position of the time-of-flight, Thomson parabola, magnetic spectrometer and neutron detector (DIAMON, from the Raylab company) are shown. Right after the target, radiochromic films (RCF) or a lithium fluoride p-n converter can be placed (courtesy of Francesco Mirani).

Considering the aim of the experiment, proton diagnostics are fundamental: a time-of-flight detector and a Thomson parabola are always active, along with the magnetic spectrometer prototype. At the cost of invalidating all the other diagnostics, RCF stacks can be installed to obtain the proton spatial distribution, along with a rough energy spectrum. A neutron spec-

trometer (DIAMON, from the Raylab company) is exploited for the neutron data. The relative position of all the diagnostics is shown in Figure 7.1.

7.2 Target design and production

In light of the experimental aims, different combinations of substrate and foam thickness are investigated, with the help of preparatory PIC simulations to determine the theoretical optimal conditions in respect to the laser properties. The commercial aluminum substrates considered are 0.75, 1.5, 2.4, 6 and 13 μm , and the magnetron sputtering ones—from the same material—are 0.75, 1.6, 2.4, 3.1 and 5 μm (the focus was on the most interesting conditions, i.e. thinner foils). The 1.6 μm magnetron sputtering film, along with the 1.5, 6 and 13 μm commercial ones are chosen for the DLT, each with 9, 18, 36 or 54 μm of carbon nanofoam.

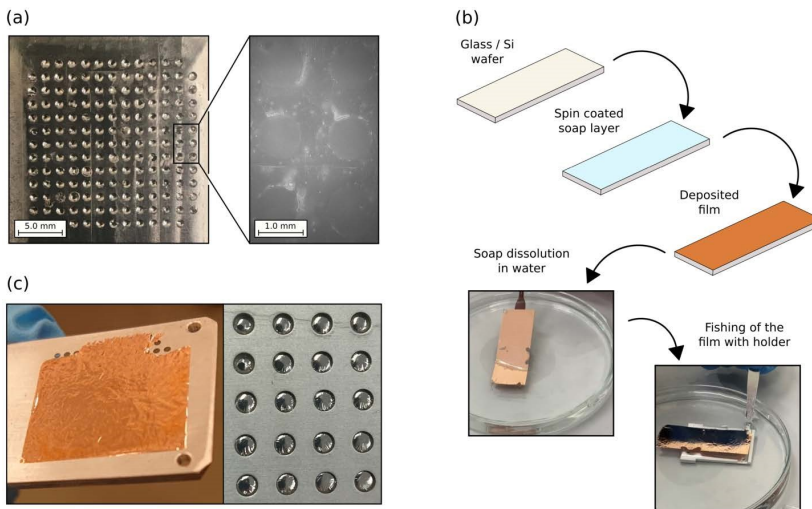


Figure 7.2: Scheme of the procedure for obtaining freestanding films on perforated holders. The steps of the process are shown in (b): spin coating of a thin soap layer on a substrate, magnetron sputtering deposition of the film, dissolution in water of the soap and film detachment, and final fishing of the film directly on the perforated holder. In (a) and (c) the final result is shown. Adapted from [189].

In Figure 7.2, the procedure for the production of the aluminum freestanding films is shown: first a substrate with a smooth surface (glass or silicon wafer) is coated with a thin layer of soap through spin coating; then the magnetron sputtering technique is exploited to grow the compact film; the soap layer is dissolved in water, separating the film, which can finally be fished directly on the perforated holder to be used in the experiment [189]. One

Chapter 7. Carbon nanofoam Double-Layer Targets for particle acceleration

important point to be noted is the quality of the film compared to the commercial ones of similar thickness: thanks to an EDXS map analysis, based on the same principles as the mass thickness maps of nanofoam materials, the actual thickness of the film can be determined, along with its uniformity. The commercial substrates, and particularly the thinner ones, showed deviations up to 40% between the real and nominal thickness, and local thickness variations as high as 25%. In contrast, the films deposited through magnetron sputtering can be precisely tuned in thickness, with local variations of only 5%.

ns-PLD is then exploited to grow the carbon nanofoams layer: this allows to have nanofoams uniform in thickness over a large area (which is needed considering the \sim cm dimensions of the target holders) together with a satisfactory microscale uniformity, even at the low thickness of $9\ \mu\text{m}$ (since the nanofoams need to be homogeneous over the $12\ \mu\text{m}$ laser spot). In order to obtain a low density nanofoam ($\sim 6.4\ \text{mg}/\text{cm}^3$, close to the critical density) and high uniformity, the depositions have been carried out with a fluence of $720\ \text{mJ}/\text{cm}^2$, 500 mJ laser energy, and 200 Pa of argon pressure.

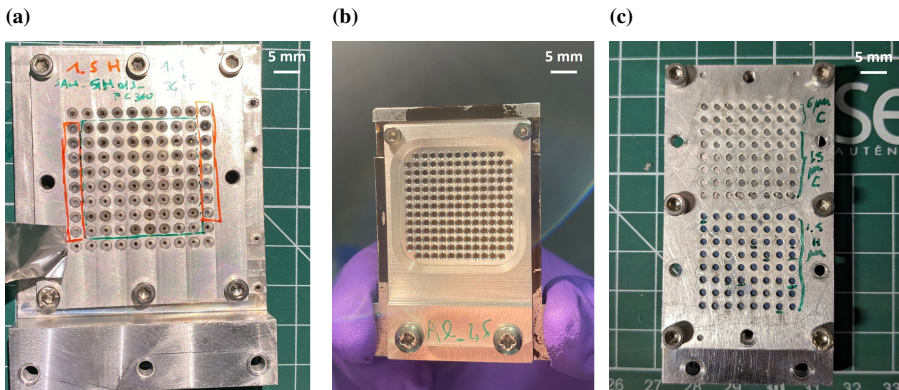


Figure 7.3: Different perforated holders exploited in the laser-driven particle acceleration experiment on VEGA 3. The left holder (a) is depicted post irradiation, thus the holes left by the laser in the substrate can be seen. The holder (b) shows a DLT, while single foils are present in holder (c).

Three different perforated holders were exploited in the experiment on VEGA 3, as shown in Figure 7.3, with varying hole dimension, distance between the holes and clamping mechanisms. As the preliminary results of Section 7.3 indicate, the holder choice is very much relevant for the target performance, especially when high repetition rate operation is required.

7.3 Preliminary results

As previously mentioned, the considerations related to targetry are of central importance for this thesis work, therefore will be considered first. Over the course of the experimental campaign, where more than one thousand laser shots were performed, it was possible to gather many valuable insights. A first one is related to the potential damage to the target in holes adjacent to the one being shot: in general, it was shown how the magnetron sputtering films were substantially more resistant, with a reduced fraction of missed shots due to first neighbours' damage. This could be connected to the higher quality of the produced films in respect to commercial foils: the higher thickness uniformity leads to the absence of excessive local thickness reductions, which—especially for the thinner foils—can undermine the film mechanical properties and promote its rupture. Moreover, the controlled magnetron sputtering film growth could lead to improved mechanical properties (e.g. due to grain size difference or reduced number of defects). No definite conclusion can be drawn at this time, and further investigations are planned to confirm these hypotheses. Not surprising, also the holder is demonstrated to have an influence, with the holders in Figure 7.3 (c) giving the best results. This could be related to the tighter fit between the two holder halves, together with the smaller holes (if compared to holder (a)) and higher distance between them (if compared to (b)), more effectively isolating each part of the freestanding foil from the effect of laser shots on neighbouring positions.

The effect of the laser shot on the neighbouring holes is significantly more relevant for the case of nanofoam DLTs, as shown in Figure 7.4: after a single laser shot (circled in blue in the figure) the nanofoam is removed significantly from the neighbouring holes (orange circle), up to a distance of three/four holes from the central one (corresponding to 5-6 mm). Further analysis of the targets after irradiation show that the foam removal effect is larger for thinner nanofoams, and is absent in the part of the target which is clamped between the two holder sides. Therefore, the most likely explanation for the foam removal is a mechanical effect, where the substrate vibrates after laser impact and the foam is detached. As a consequence, it is not surprising that the holder has again an impact, with the larger holes (and less tight clamping) of holder (a) in Figure 7.3 giving the worst performance. On the contrary, the small and well separated holes in (c) show again the least detrimental effects.

This behaviour of the DLTs has been taken into account in the data acquisition phase of the experimental campaigns, ensuring sufficient distance between one shot and the next, with the drawback of reducing the available number of shots from 50-100 per holder in the case of solid foils to 5-10 per



Figure 7.4: Post irradiation optical microscope image of a section of a target with holder (b) (refer to Figure 7.3). The target is composed by a $6\ \mu\text{m}$ commercial foil with $36\ \mu\text{m}$ of carbon nanofoam. The blue circle indicates the shot hole, while the larger orange circle highlights the surrounding area in which the foam has been damaged.

holder for DLTs. The limited number of available shots is the reason for the larger error bars for the foam sample in respect to the bare substrate (0 foam thickness) in Figure 7.5.

Nevertheless, the obtained preliminary results are promising as far as the nanofoams capability to enhance the acceleration process is concerned. Figure 7.5a reports the maximum proton energy in function of the foam thickness, showing the best performance (an enhancement of about 2 MeV) for the DLT with foam thickness of $18\ \mu\text{m}$. The existence of an optimum foam thickness depending on the laser and foam properties (such as laser intensity, spot size, foam density) is well known [190], and can be explained in light of the self-focusing effect: as described in Chapter 3, a high-intensity laser propagating in a near-critical density medium will be focused during propagation, with a consequent enhancement in intensity, laser energy absorption and hot electron generation peaking when the focalization is maximum. Therefore, the optimal foam thickness in a DLT is expected to be around the self-focusing length, which through a simple estimation ($l_f \approx w_0/\sqrt{\bar{n}}$, where $\bar{n} = n_e/\gamma_0 n_c$ is the foam transparency factor) is indeed found to be close to $18\ \mu\text{m}$ in this specific case. The number of protons is also increased

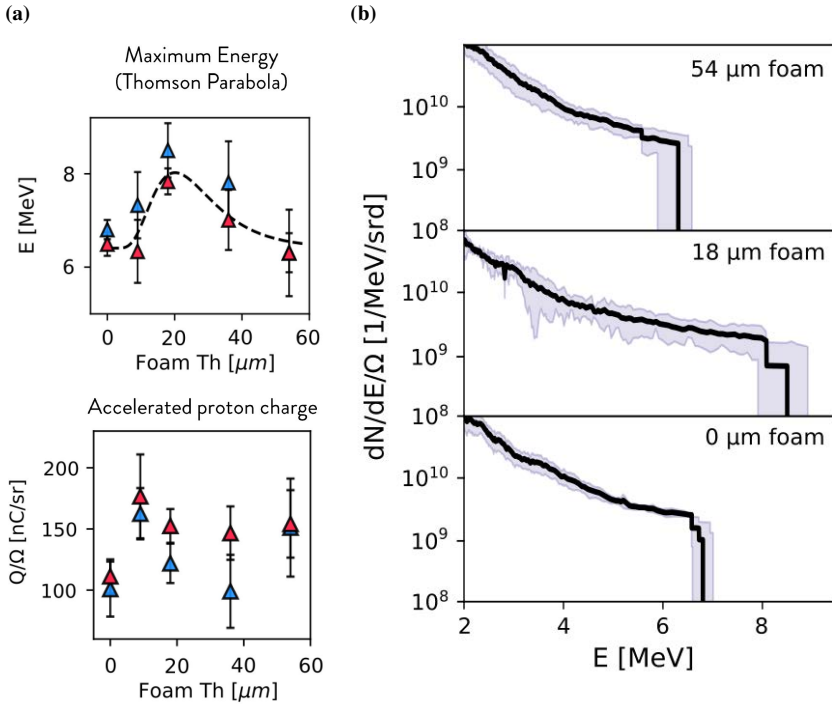


Figure 7.5: (a) Evolution of the proton maximum energy (top) and accelerated proton charge (bottom) as a function of the nanofoam thickness, for 1.6 μm deposited substrates (in blue) and 6 μm commercial ones (in red); (b) respective proton energy spectra for three foam thickness cases, for 1.6 μm deposited substrates (courtesy of Francesco Mirani).

by a factor of $\sim 70\%$, as demonstrated in the graph below. Analogous conclusions can be drawn from the proton energy spectra depicted in Figure 7.5b.

To conclude, DLTs are demonstrated to be promising candidates for enhancing laser-matter interaction, thus leading to a more efficient proton acceleration. For this reason, further investigations into the optimization of the targetry setup are certainly worthwhile, and would be fundamental in avoiding or mitigating the issue related to foam detachment, also in high repetition rate operation.

CHAPTER 8

Carbon nanofoams as ICF ablaters

In this Chapter, the investigation into the use of carbon nanofoam materials as ablaters for inertial confinement fusion applications is discussed, for their potential in increasing laser absorption and smooth laser inhomogeneities. The work has been performed in collaboration with the ENEA Frascati group in charge of the ABC laser facility, on which the experimental activity has been performed. The laser facility, along with the experimental setup, diagnostics and aims of the experiment are described in Section 8.1. As a preparatory activity, the potential of carbon nanofoams as ICF ablaters is investigated through hydrodynamic simulation, in the framework of a Master Thesis (Vittorio Ciardiello [168]). The main results, described in Section 8.2, were also published in the *Laser and Particle Beams* journal with the title “Numerical study of carbon nanofoam targets for laser-driven inertial fusion experiments” [191]. Exploiting the insights, the carbon nanofoam target production through PLD is carried out, in the framework of another master thesis (Maria Sole Galli De Magistris [169]) as described in Section 8.3. Lastly, in Section 8.4 a choice of promising preliminary results is presented (the data analysis is still ongoing).

8.1 ABC laser facility, experimental setup and goals

Starting from the considerations of Section 2.2, it is clear how the enhancement of laser energy absorption and its conversion into mechanical loading (i.e. pellet compression) are fundamental avenues of improvement in ICF. The same can be said for instability mitigation, and foam materials are particularly promising for both aims, as introduced in Section 3.3. Microstructured plastic foams (made with chemical methods) are the most investigated for ICF application, while at the same time mid-Z materials (such as high-density carbon) have demonstrated promising properties in reducing laser-plasma instability. This Chapter reports a first investigation into the behaviour of nanostructured carbon foams under irradiation by ICF-relevant lasers, with the aim to assess their feasibility as ICF ablator materials. The experiment has been carried out at the ABC laser facility at the ENEA Frascati laboratories [176], introduced in Section 4.4. For this experimental campaign, the laser energy was set to 40 J, that together with the 3 nm pulse duration (FWHM) and 100 μm focal spot diameter leads to an intensity on target of about $2 \times 10^{14} \text{ W/cm}^2$. A planar target irradiation geometry is used, exploiting only one of the two laser beams of the ABC laser, as depicted in the experimental setup scheme of Figure 8.1.

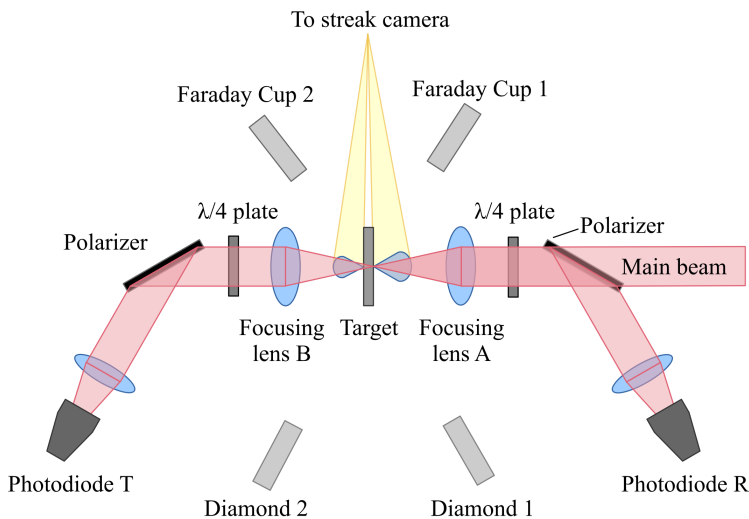


Figure 8.1: Scheme of the sample irradiation setup at the ABC laser facility. The laser comes from the right, focusing on the target in the center, while two photodiodes are set up to collect the reflected and transmitted light. Some of the main diagnostics are also shown, such as faraday cups and diamond detectors both toward the front and the back of the target, and a streak camera looking from the side.

8.2. Preparatory hydrodynamic simulations

Being a high-power laser based on flashlamp pumping, the ABC laser allows only one or at most two shots a day, considering also the time to achieve a sufficiently high vacuum after the interaction chamber is opened to replace the target. Therefore, the simultaneous presence of many diagnostic equipment is fundamental, with the aim to completely characterize each interaction. Some of the main diagnostics are shown in Figure 8.1: two photodiodes to measure transmitted and reflected light, a streak camera looking at the side of the target to see the plasma evolution in time, and both Faraday cups and time-of-flight diamond detectors to detect the presence of accelerated particles. Shadowgraphy, Schlieren and interferometry measurement of the interaction from the side are also acquired, with the aid of a second harmonic probe beam synchronized with the laser main pulse. Integrated visible spectrometry measurements of the interaction site complete the main diagnostics available, together with a time-gated X-ray detector (SLIX). Since the data analysis is still ongoing, the focus of this Chapter will be on the target design and production, with a limited selection of promising preliminary results in Section 8.4.

8.2 Preparatory hydrodynamic simulations

Thanks to the tunability of the PLD technique, especially considering both ns and fs-PLD, different carbon nanofoam morphologies and densities can be obtained, as investigated in detail in Chapter 5. Considering also the limited shots available in the ABC experimental campaign, and the novelty of nanostructured carbon foam in ICF applications, it is of particular interest to investigate which nanofoam characteristics are the most interesting for ICF through simulations.

Series	Deposition method	Density ρ_p [mg/cm ³]	δ_0 [μ m]	b_0 [nm]
A	ns-PLD	6	10	30
B	fs-PLD	6	20	60
C	ns-PLD	18	5	45
D	fs-PLD	18	10	90

Table 8.1: Carbon nanofoams on which the numerical investigation is based on, together with the respective properties. Corresponding SEM micrographs and EDXS mass-thickness maps are shown in Figure 8.2 and 8.3.

In order to do so, four category of carbon nanofoams are considered, as shown in Figure 8.2 and Table 8.1, with varying density (6 or 18 mg/cm³) and morphology. The lower density is the lowest one achievable for PLD-

produced nanofoams, while the higher one is the higher density for which the nanofoam morphology is not altered significantly toward more compact structures. In general, the nanofoam morphology and density are coupled parameters, however by exploiting both ns-PLD and fs-PLD it is possible to obtain nanofoams with the same average density but different morphology. As evidenced in Chapter 5 and clearly seen from Figure 8.2, the ns-PLD nanofoams (A and C) are more uniform than the respective fs-PLD ones (B and D), which present larger voids.

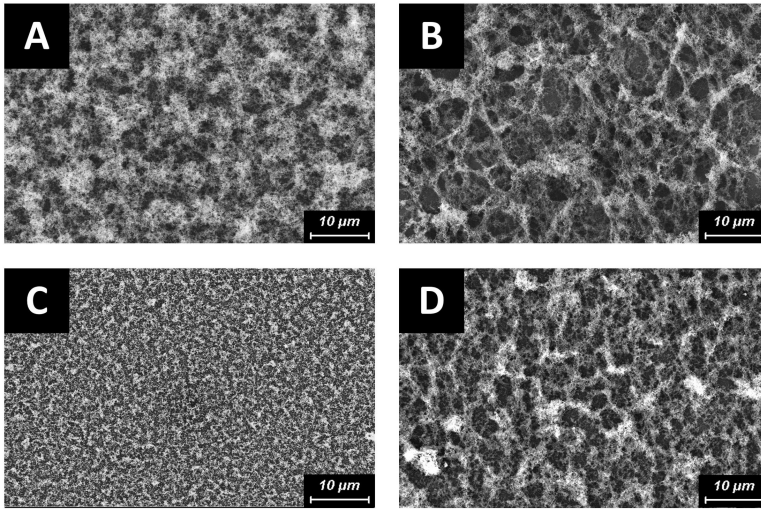


Figure 8.2: Four categories of carbon nanofoams produced with ns-PLD (A, C) and fs-PLD (B,D), with lower (A, B) or higher (C, D) density. The corresponding nanofoam parameters are reported in Table 8.1.

The simulations are performed with the 1D MULTI-FM hydrodynamic code [132], which specifically includes the effect of porous materials through a model of the foam expansion and homogenization under laser irradiation. The model accounts for the presence of both solid elements and voids in the foam structure, exploiting a specific parameter describing the degree of homogenization of the foam in the evolution of the system from an inhomogeneous foam toward a homogeneous plasma. Throughout the process, both thermal conduction and mechanical forces are limited by the homogenization parameter, accounting for the inhomogeneous distribution of electrons and ions in the foam material (further details are reported in [132]). The equation of state for carbon is obtained from the SESAME library. The code is validated for the more established plastic foams, well described as solid elements of size b_0 alternating with pores of size δ_0 , generally in the micrometer range. Together with the density of the solid parts ρ_s and the

8.2. Preparatory hydrodynamic simulations

fractal parameter α , the average density of the porous material is expressed in the following form (introduced in Section 3.1, with $1/\alpha = \nu + 1$):

$$\frac{\rho_p}{\rho_s} = \left(\frac{b_0}{\delta_0} \right)^{1/\alpha} \quad (8.1)$$

Compared to plastic foam, carbon nanofoams present a more complex morphology, with nanoparticles as the basic constituents and self-similarity at different spatial scales, making the determination of the foam parameters to provide to the code—namely, b_0 , δ_0 and α —a far from obvious task. In order to do so, it is possible to compare the model in Equation 8.1 with the quite similar density fractal scaling valid for carbon nanofoams, relating the nanofoam density to the aggregate properties d_0 , R_g and D_f (nanoparticle diameter, aggregate gyration radius and fractal dimension):

$$\frac{\rho_p}{\rho_s} = k \left(\frac{d_{np}}{2R_g} \right)^{3-D_f} \quad (8.2)$$

Considering the meaning of the two fractal parameters, α and D_f , it is reasonable to expect them to be independent of the other parameters, leading to $\alpha = (3 - D_f)^{-1} \approx 1$. The relationship between b_0 , δ_0 , d_0 , R_g and k is less obvious, but if it were possible to compute the pore dimensions δ_0 independently, the last parameter could be easily derived by inverting Equation 8.1: $b_0 = [(\rho_p/\rho_s) \cdot \delta_0]^\alpha \approx (\rho_p/\rho_s) \cdot \delta_0$.

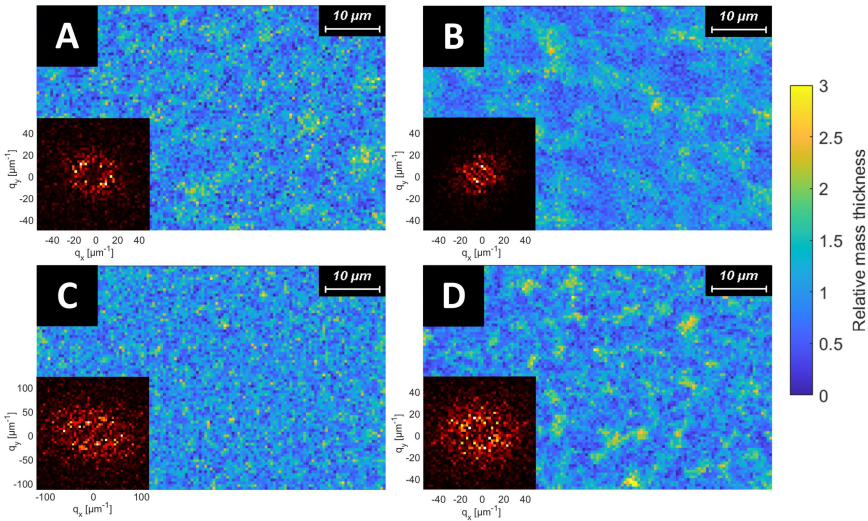


Figure 8.3: Mass thickness maps of the nanofoams of Figure 8.2, with their Fourier transform in the bottom-left inset.

Indeed, the pore size can be estimated on physical grounds on the basis of the nanofoam morphology, as the size of the larger voids part of the foam structure. To do this quantitatively, it is possible to exploit the mass thickness maps of the nanofoams—or more specifically, their Fourier transform analysis—to determine the uniformity spatial scale. This is indeed a measure of the large-scale voids in the foam structure, corresponding to the most predominant spatial frequency in the mass distribution inside the nanofoam.

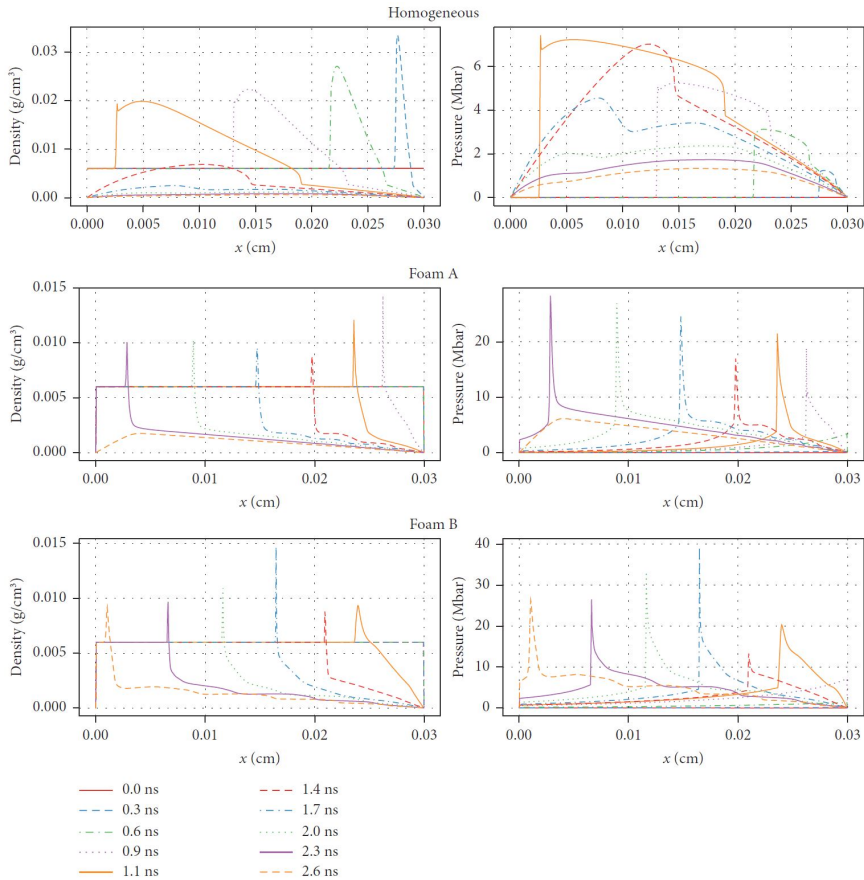


Figure 8.4: Density and pressure evolution of the low density A and B foams (the laser comes from the right). An equivalent density homogeneous medium is shown as a reference.

As seen in the insets of Figure 8.3, where the center of the image Fourier transform is shown, A and D foams present similar pore size, while δ_0 is larger for B (smaller size of the figure in the Fourier domain) and smaller for C (note the different scale of the inset). The exact values resulting from the analysis are reported in Table 8.1, together with the last parameter b_0

8.2. Preparatory hydrodynamic simulations

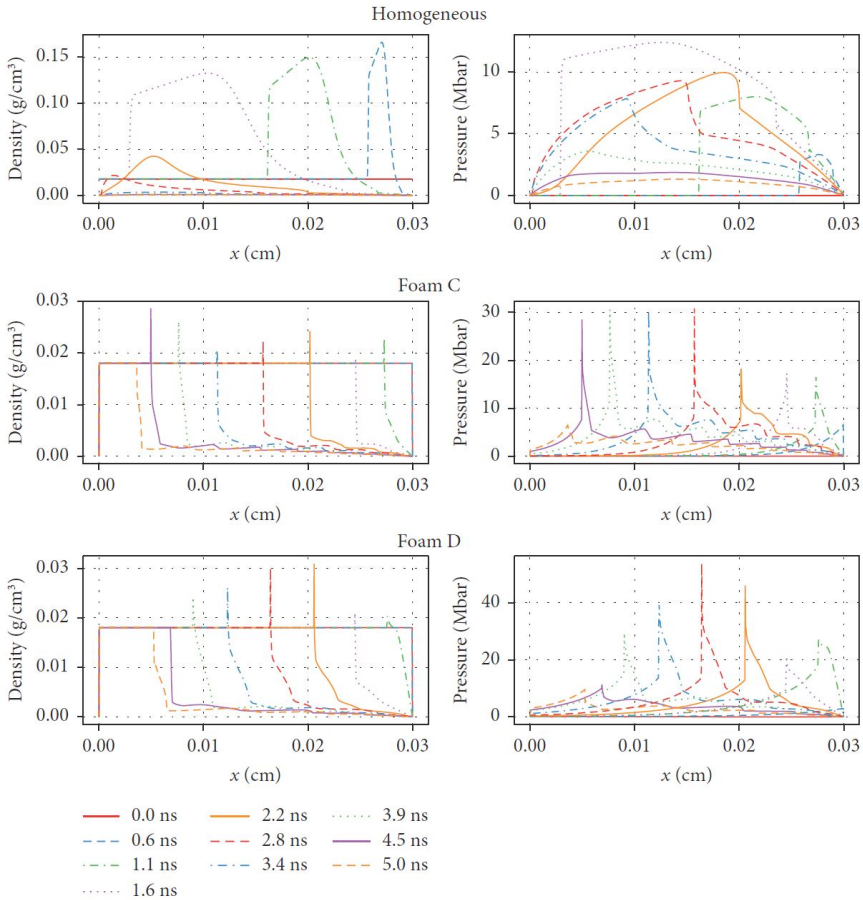


Figure 8.5: Density and pressure evolution of the high density C and D foams (the laser comes from the right). An equivalent density homogeneous medium is shown as a reference.

calculated from Equation 8.1 (ρ_s is fixed at 2.0 g/cm^3). With this description, the results for b_0 (some tens of nanometers) appear reasonable: considering a nanoparticle dimension close to 10 nm, the solid parts can be interpreted as the strands/aggregates of nanoparticles forming the microstructure of the nanofoam. The model can thus be considered representative of the foam microstructure, while blind to the specific nanostructure at a lower scale.

In the simulations, the laser parameters are chosen to be representative of the ABC laser facility: 3 ns pulses at 1054 nm, with an on-target intensity of 10^{14} W/cm^2 . This leads to a plasma critical density in the order of 3 mg/cm^3 , making all the investigated foams overcritical.

The simulation results for the low density case (6 mg/cm^3) are reported in Figure 8.4, with 10 and 20 μm pore size for the A and B case respec-

tively. Compared to a homogeneous media of the same density, both foams show significantly lower shockwave propagation, due to the time needed to homogenize the material. As could be expected, the higher pore size in B leads to a slower shockwave, due to the longer homogenization time. The pressure at the shockfront is also substantially enhanced for the nanofoams, effect that can be attributed to the lower thermal conduction and inhibited hydrodynamic motion of porous materials.

For the high density case (18 mg/cm^3), 5 and $10 \text{ }\mu\text{m}$ pore size for C and D respectively, the shockwave is even slower than in the previous cases. While the smaller pore size would push in the direction of a lower homogenization time, the higher density has an opposite effect, making the homogenization time substantially equivalent. The slower shockwave can then be explained as purely due to the higher density of the foam. The significant enhancement in the pressure at the shockfront is confirmed, exceeding 20-30 Mbar, and even higher than the lower density foams.

While limited in scope and predictivity due to the simplicity of a 1D hydrodynamical model, the simulations indicate a promising enhancement in ablation loading and shockfront pressure for carbon nanofoam materials, highlighting the higher density samples (C and D) as the best performing. In these conditions, the peak pressure happens after a time equal half the laser duration, i.e. when the laser intensity is at its maximum. As a consequence, the ideal foam thickness leading to the highest shockfront pressure can be estimated, resulting in the order of $150 \text{ }\mu\text{m}$.

8.3 Target design and production with PLD

Considering the limited number of laser shots available in the experimental campaign, as anticipated in Section 8.1 (in the order of 10/13), a choice had to be made regarding which carbon nanofoam properties to investigate. Moreover, different substrates could be interesting for different aims: bulk solid substrates can be exploited to study the crater left by laser-mater interaction, as an effective estimation of the ablation loading on the substrate; at the same time, thin substrates allow full characterization of the interaction by the many diagnostics, with different line of sight requirements (which would be partially blocked by a bulk substrate). Taking into account the results of the simulations from the previous Section, the higher density nanofoam display the best performance, with the effect of the pore size (ns vs fs-PLD) being minor. Therefore, the density is chosen as the main parameter to be investigated, and all nanofoams have been produced through ns-PLD. This present other practical advantages, such as higher thickness uniformity on large samples, even for compact films and the higher thickness required.

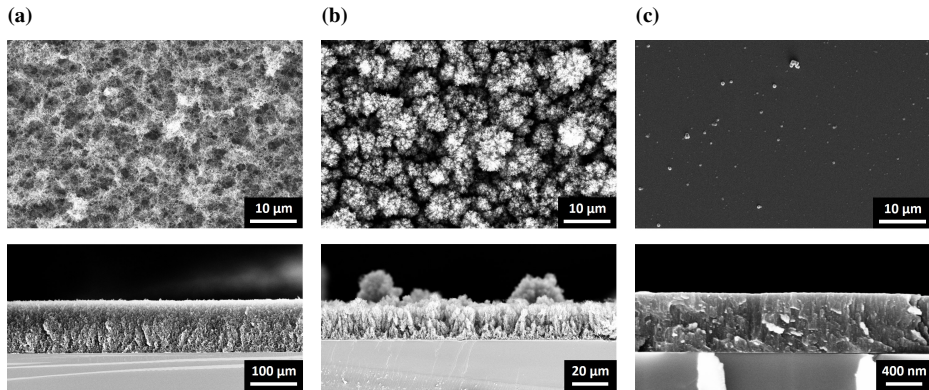


Figure 8.6: Carbon nanofoams and films produced as ablator candidates, to be tested in the ABC experimental campaign: (a) carbon nanofoam, (b) tree-like film, (c) compact carbon film. Plane views are shown on the top, and the respective cross-sections on the bottom.

Three density values, each corresponding to a different morphology, have been investigated: 6 mg/cm^3 carbon nanofoams, 26 mg/cm^3 tree-like films, and 2000 mg/cm^3 compact amorphous carbon films. The morphology of the different materials is shown in Figure 8.6. The PLD depositions are performed with high energy and a large laser spot on the target, leading to moderate fluence conditions (720 mJ/cm^2 with 500 mJ laser energy), optimal conditions to obtain a uniform films and a high reproducibility of results. 200 Pa of argon are used for the nanofoams, 50 Pa for the tree-like films and 5 Pa for the compact ones. Two film thickness values are considered for each sample, the highest corresponding to a mass thickness of 1600 mg/m^2 and the smallest to half that value (800 mg/m^2). This comparison for equal mass thickness led to $267\text{-}133 \text{ }\mu\text{m}$ nanofoams, $60\text{-}30 \text{ }\mu\text{m}$ treelike films and $0.8\text{-}0.4 \text{ }\mu\text{m}$ compact carbon films.

The carbon nanofoams and films were deposited on three different kind of substrates: (I) thick bulk aluminum substrates, able to withstand the laser impact to allow the investigation of the crater and its volume post-irradiation; (II) 1 mm square frames holding 100 nm thick CH freestanding films (Figure 8.7a), so thin as to not influence the laser-matter interaction—and thus leading to conditions comparable with a freestanding foam; (III) $1 \text{ }\mu\text{m}$ aluminum freestanding foils on specifically designed C-shaped holders, balancing the need for a thin substrate with the diagnostic line of sight requirements (Figure 8.7b).

For the first kind of targets, the bulk substrate does not allow to exploit the diagnostics on the back of the target, as their line of sight to the interac-

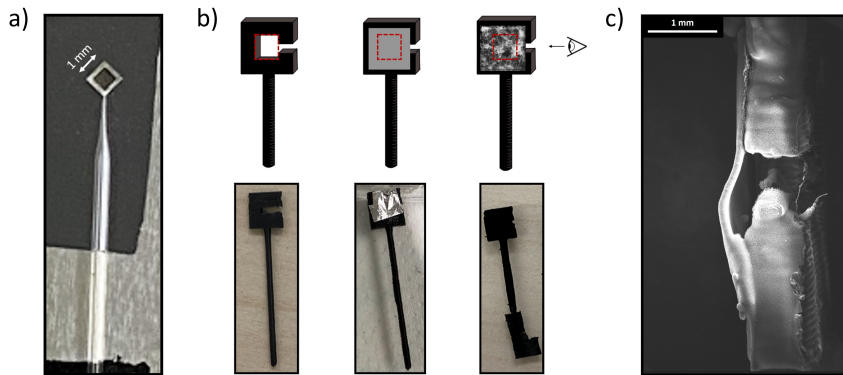


Figure 8.7: (a) 10 nm CH freestanding substrate with the square holder and glass stalk; (b) schematics of the 1 μm aluminum freestanding substrates, mounted on the C-shaped holders; (c) side view of a complete target formed by the c-shaped holder (top and bottom) along with the thin aluminum film on which the nanofoam is deposited (left).

tion region is blocked by the target itself. Moreover, the practical difficulties in properly aligning a target of a larger size leads to uncertainties in the diagnostics looking at the interaction from the side (such as the visible streak camera and shadowgraphy): a slight target tilt could partially shadow the interaction zone, reducing their reliability. The second targets, due to the really thin substrate (100 nm), allow data acquisition also from the rear side (e.g. particle detectors and transmitted light), but also in this case the presence of a thicker frame all around the substrate hinders the visible streak camera and shadowgraphy from the side, creating a large shadow over the interaction region. For this reason, the C-shaped substrate were designed and produced, combining a thin aluminum foil with a 3D printed holder, as depicted in Figure 8.7b. The absence of the holder on one side of the substrate allows a free access to the interaction region from the side, as shown in Figure 8.7c.

The deposition of the PLD carbon nanofoams and films on the different substrates was not completely free from difficulties: the 100 nm CH film of Figure 8.7a was quite fragile, therefore only the nanofoam samples were deposited successfully. In all other cases the fracturing of the substrate was observed, likely due to the higher ablated species energy of the tree-like and compact films. The compact carbon film showed some issues on both thick aluminum substrates and thin aluminum foils, leading to partial delamination of the carbon film in the first case and wrinkling of the freestanding substrate in the second. Both can be attributed to the high stress state, common in PLD compact films. The issue was not always present for the thick substrates, likely due to the slight differences in surface roughness, and the wrinkling of thin foils was mitigated by firmly attaching them on the holders. Therefore,

functional targets were obtained for both.

8.4 Experimental campaign results

Among the many diagnostics employed, some of the most interesting results are related to the study of the ablation craters post irradiation, whose volume can be related to the conversion efficiency of laser energy into target compression: while an indirect measurement, the energy to sustain phase transition (i.e. laser ablation) behind the front of the propagating shockwave in the solid target can be directly linked to the total ablated volume [157]. The approach was successfully exploited in multiple experiments to determine the shockwave energy resulting from laser ablation of the target [157, 192, 193]. Exploiting a Leica DMI5000 M Inverted microscope, equipped with the LAS Montage module, the crater volume was measured for the case of a nanofoam coating and a tree-like film of maximum thickness (267 and 60 μm respectively). Compared to the value for the bare aluminum substrate ($3.41 \times 10^7 \mu\text{m}^3$), the crater volume was moderately increased for the nanofoam-coated sample ($3.97 \times 10^7 \mu\text{m}^3$), and almost doubled for the tree-like target ($6.02 \times 10^7 \mu\text{m}^3$).

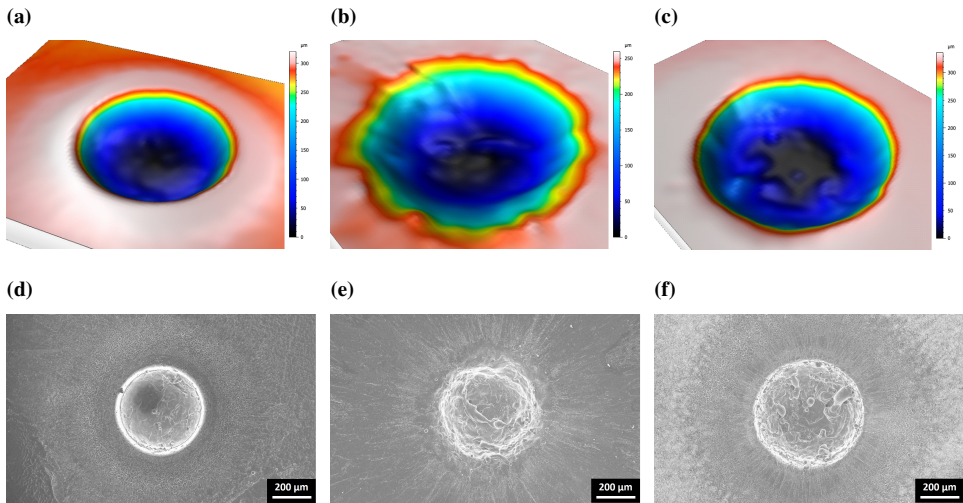


Figure 8.8: Analysis of the ablation craters post-irradiation, with the microscope reconstructed surface on the top (a, b, c) and the respective SEM micrographs on the bottom (d, e, f). (a, d) are the craters on the bare aluminum substrate, (b, e) the nanofoam samples and (c, f) the tree-like ones.

It is also of particular interest to note the morphological features of the different craters, as depicted in Figure 8.8: the bare aluminum crater presents

a precise circular shape with sharp edges, as the footprint of the laser spot size shape. On the contrary, the nanofoam-coated sample presents a slightly larger crater with jagged edges, and disordered structures on the bottom of the crater. The tree-like sample—beside the evident increase in size—shows features which are between the other two, with mostly clear-cut edges and some structures on the crater bottom. A possible explanation can be derived considering the different effect of the two film morphologies on the laser-matter interaction: on one side the nanofoam, leading to an increased scattering of the laser pulse energy due to its disordered nature, while the more compact (and higher density) tree-like film is able to enhance the laser absorption and more efficiently transfer the energy to the substrate. Interestingly, during the experiment it was found that the carbon nanofoam, despite being overcritical on average, is substantially transparent to the laser light (at intensities much lower than the ionization one). This is due to the porous void-rich structure of the material, and can be a useful element in explaining the observed results.

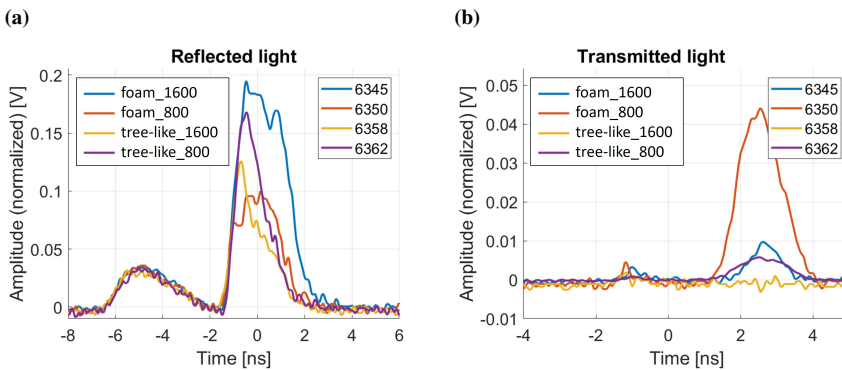


Figure 8.9: Reflected (a) and transmitted (b) light in function of the time, as measured by photodiode R and T respectively (Figure 8.1. Time 0 corresponds to the instant where the laser peak reaches the target. The first low peak in (a) is the reflection from a window, exploited as a reference for time calibration.

By exploiting the thin aluminum substrates on the C-shaped holders, the data from other diagnostics can be exploited to give further insight into the interaction of the laser with the carbon materials, and support the previous findings. Two examples are the reflected and transmitted light of Figure 8.9 and the streak camera results of Figure 8.10.

Regarding the first one, considering the relationship between reflection, transmission and absorption, a confirmation of the previous findings can be drawn. In Figure 8.9, the transmitted and reflected laser light for the nanofoam and tree-like samples of different thickness are compared. It can

8.4. Experimental campaign results

be seen how the thick nanofoam sample is the more reflective, which can be attributed in part to the foam own reflectivity and in part to its transparency and subsequent reflection from the aluminum substrate. Part of the light is also transmitted, indicating the failure of the substrate within the laser pulse duration. The reflectivity is similar for the thin tree-like sample, while being shorter in time, alongside an analogous transmission. The higher reflectivity and transmission are coherent with a lower absorption for the thinner targets. On the contrary, the total absence of transmission and lower reflectivity of the thick tree-like film is indication of a higher absorption, coherently with the higher crater volume. The high transmission and low reflection of the thin foam sample can be due to the foam transparency: the laser can reach the substrate and starts to be reflected, but as the substrate breaks the transmission increases significantly and the reflection is reduced.

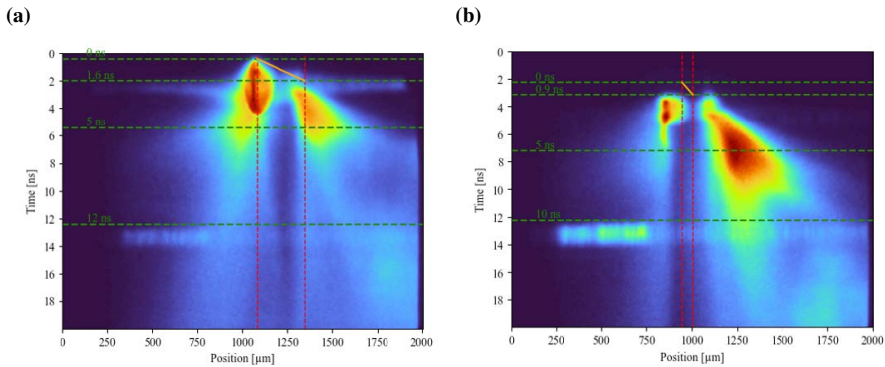


Figure 8.10: Streak camera images for the thick foam sample (a) and thick tree-like sample (b), corresponding to shot #6345 and #6358 of Figure 8.9. The laser comes from the left.

The streak camera images of Figure 8.10, corresponding to the thick nanofoam and tree-like samples respectively, confirm the previous results: for the tree-like sample, the light emission in the back of the target is much stronger, coherently with a higher laser energy transfer to the substrate. On the contrary, the larger emission for the nanofoam could be linked with the foam transparency and laser reflection from the substrate.

Despite the data analysis is still ongoing, the results are particularly encouraging, especially considering the great enhancement in ablation loading obtained with tree-like carbon films. This, together with the consideration on nanofoam transparency, corroborate the claim that the material structure and morphology is of fundamental importance in laser matter interaction experiments. In light of the positive results of this first investigation, the interest

Chapter 8. Carbon nanofoams as ICF ablators

in further experiments on carbon-based nanomaterials as ablators in ICF is confirmed.

CHAPTER 9

Hydrogen-enriched boron nanofoams for proton-boron fusion experiments

This last Chapter describes the experimental activity performed in the framework of proton-boron fusion research, with the aim to exploit the potential of fs-PLD to produce boron-based nanofoam targets to be tested in laser-driven fusion schemes. The activity is carried out in collaboration with Queen's University Belfast, where the high intensity laser TARANIS is located. Following the scheme of the previous Chapters, first the laser facility and setup are described in Section 9.1, together with the general aims of the experiment. The experimental activity carried out on fs-PLD for target production and characterization is addressed in Section 9.2, and finally some promising preliminary results are presented in Section 9.3. The activity is also part of a Master Thesis work (Alessandro Milani [170]).

9.1 TARANIS laser facility, experimental setup and goals

The field of laser-driven proton-boron fusion, as introduced in Section 2.3, would indeed take advantage of improvements in target design to enhance the process, considering the low cross section of the reactions and the standard targets routinely used in p-B fusion experiments (i.e. boron nitride solid

Chapter 9. Hydrogen-enriched boron nanofoams for proton-boron fusion experiments

targets). Moreover, the ability to control the target composition (and specifically its hydrogen content) is of clear interest to maximize the fusion reaction rate. In this Chapter a first investigation into the application of boron-based nanofoam and nanostructured materials for proton-boron fusion is reported.

The proton-boron fusion experiment is performed on the TARANIS laser, at the laboratories of Queen's University Belfast. During the experiment, the 10 J, 1053 μm , 800 fs laser pulse is focused on a 5.5 μm spot on the target, leading to an intensity exceeding 10^{19} W/cm². These conditions, while approaching those typical of laser-driven particle acceleration experiment, are characterized by a longer pulse duration (and thus a lower intensity), with potential implication on the laser-matter interaction dynamics. Considering the aim to promote fusion reaction by accelerating protons and/or boron ions to suprathermal conditions, a longer pulse duration could be beneficial in increasing the total amount of alpha particle produced per shot.

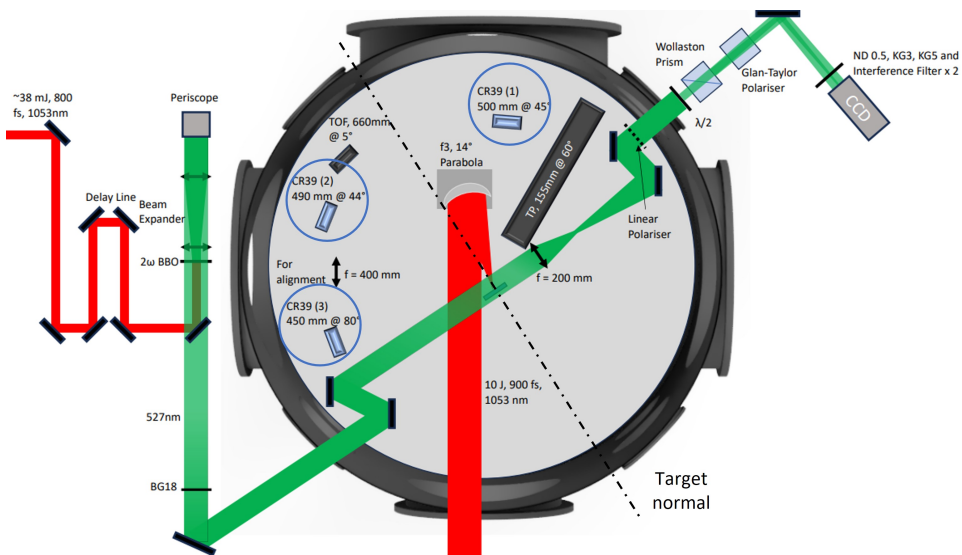


Figure 9.1: Scheme of the irradiation chamber setup at the TARANIS laser facility. The positions of the main alpha particle diagnostics employed, i.e. CR39 nuclear detector, are highlighted. Other particle diagnostics (Thomson parabola and time-of-flight detector) are shown, along with the interferometry setup.

Considering the alpha particle production as the main indication of target performance, the experimental scheme was chosen to allow their detection: the alpha particle range in solid density materials is limited, therefore all the diagnostics were placed in the front side of the target, at different angles. The complete setup is shown in Figure 9.1, including CR-39 track detectors, an interferometry setup, and other particle detectors such as a Thomson

parabola and a time-of-flight detector.

Indeed, the main issue in laser-driven proton-boron fusion experiments is the alpha particle detection, and in particular their discrimination from the protons and other heavy ions that can be produced during laser-matter interaction, which is why multiple ion diagnostics are especially useful. Nuclear track detectors, such as CR-39, are the most common technique used for alpha particle detection: they are passive detectors, based on the damage induced in the material by each ionizing particle. They can be read after an etching phase, thanks to which the tracks become visible. While not always possible or convenient, a discrimination between protons, alpha particles and heavier ions can be made on the basis on the track area, as the higher energy deposition of alphas and high-Z ions leads to larger tracks. In order to do so, the most common approach exploits differential filtering, where micrometric metallic foils of varying thickness—on top of CR-39 detectors—can aid in discriminating charged particles from one another in virtue of their stopping power. After calibration, the alpha particle number and spectral data can be obtained with sufficient accuracy, in agreement with Thomson parabola measurements [194, 195]. An analogous approach has been applied in this experiment, with different filters in front of the CR-39 (able to also increase the energy range of the measured ions): 6.5, 10, 14, 20 and 28 μm thick aluminum foil were used, corresponding to minimum alpha energies of 2, 2.8, 3.7, 4.8, 6.0 MeV.

9.2 Boron-based targets design and production with fs-PLD

Taking into account the laser characteristics and the experimental setup, targets of sufficiently high thickness (in the order of 100 μm) and density (50-100 mg/cm^3) were required: in order to efficiently promote fusion reaction in the foam, a high enough mass thickness of "fuel" is needed; at the same time, low target densities would quickly lead to plasma formation and target expansion, significantly reducing proton-boron collisions and thus fusion reactions.

Additionally, one the most interesting target features is their hydrogen (and thus proton) content, to achieve a H:B ratio close to 1, instead of simply exploiting the impurities in the target as proton sources. Indeed, one of the main objectives of the PLD experimental campaign was to devise a way to produced hydrogen-enriched boron-based targets. The proposed approach is to consider hydrogen-rich polymeric materials (such as polyethylene or polypropylene) as abundant source of hydrogen, with the drawback of the unwanted presence of carbon in the target.

Taking advantage of the results of Chapter 6, the fs-PLD technique is

Chapter 9. Hydrogen-enriched boron nanofoams for proton-boron fusion experiments

exploited to produce boron nanofoams of the desired properties: 100 μm thick nanofoams of 50 or 100 mg/cm^3 density are obtained through 180 and 300 Pa of background argon pressure respectively (an example of the lower density nanofoam is shown in Figure 9.2a). The same fs-PLD technique could be also exploited to produce nanofoams and nanostructured materials from hydrogen-rich polymers. Multiple possibilities are investigated, with some difficulties due to the transparency of many polymers to the laser radiation, only partially mitigated by the nonlinear high-intensity effects taking place in fs-PLD. Between polymethyl methacrylate (PMMA, not ideal for the lower hydrogen content and oxygen presence), polypropylene (PP) and high density polyethylene (HDPE), the last material gave the best results: with a fluence of 110 mJ/cm^2 and 5000 Pa of argon as background gas, nanoparticle-assembled films with a tree-like morphology and ~ 120 mg/cm^3 density are obtained (example shown in Figure 9.2b).

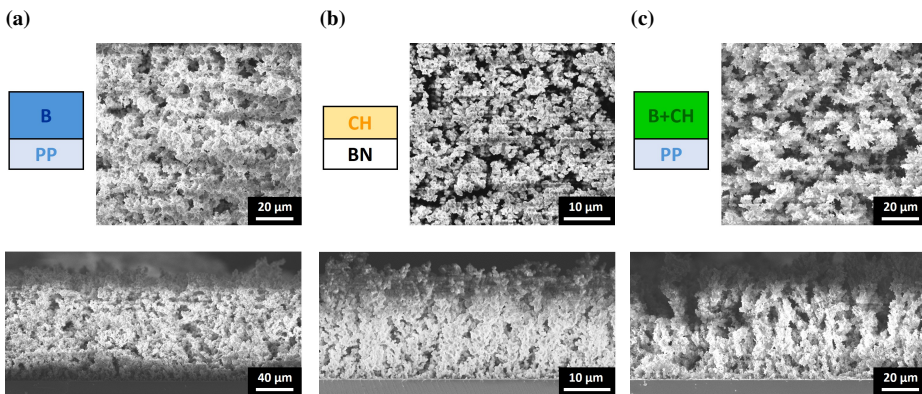


Figure 9.2: SEM micrographs and schematics of the boron-based targets exploited in the proton-boron fusion experimental campaign. On the first row the top-view SEM images are shown, together with the corresponding target scheme on the left. On the bottom the cross-sections are shown, to highlight the material morphology. (a) boron nanofoam, 50 mg/cm^3 ; (b) CH nanofoam from HDPE ablation, 120 mg/cm^3 ; (c) hydrogen-enriched boron nanofoam, codeposition of boron and HDPE, 80 mg/cm^3 .

The versatility of the fs-PLD is then capitalized to produce mixed boron-CH films, through codeposition of boron and HDPE. A small HDPE target is mounted in the center of the larger boron PLD target, such that the laser ablates alternatively one or the other during the deposition. The resulting morphology obtained at 180 Pa is shown in Figure 9.2c, with an average density near 80 mg/cm^3 . One first difficulty in the codeposition could result from the different pressure conditions needed to slow the ablated species in the case of boron (few hundred of Pa) and HDPE (5000 Pa). In practice,

however, keeping the pressure used for the boron case proved sufficient, with only a slight increase in average density in the film. A more significant issue is instead connected to the film homogeneity in thickness and composition: the ablation plume for the case of boron is not perpendicular from the target as usually in PLD, but shifted toward the laser, leading to a deposition of boron nanofoam on the substrate which is peaked at a certain distance from the center. On the contrary, the CH deposition from HDPE is peaked in the substrate center, as the plume is perpendicular from the target. This issue is addressed by performing the depositions with a static substrate, and placing it in the position where the two deposited material distributions overlap.

Different kind of targets were produced for the experimental campaign on the TARANIS laser: first, a boron nitride (BN) target was used as a reference, being the most common target exploited in p-B fusion experiments. Regarding the boron-based nanofoam targets, they were deposited on 1 mm polypropylene (PP) substrates, a material devoid of boron to ensure any fusion reaction took place in the foam region. Boron nanofoams of 50 and 100 mg/cm³ and 100 μm thickness are considered, where protons for fusion could be provided by impurities only (Figure 9.2a). The second kind of targets are hydrogen-enriched boron nanofoams on the same polypropylene substrates, obtained through boron and HDPE codepositions, with a density of 80 mg/cm³ and a 60 μm thickness (Figure 9.2c). The third kind of targets considered a different approach: promote an enhancement of the fusion reaction happening in a boron nitride target through a thinner (20 μm) front layer of nanostructured CH, produced by fs-PLD of HDPE (Figure 9.2b).

The determination of the targets average density was performed through the same method detailed in the previous chapters, exploiting the EDXS data for the different elements to derive the mass thickness (through the ED-DIE method [174]) and combining it with the geometrical thickness to compute the density. Regarding the results of the EDXS composition analysis, it should be noted the oxygen incorporation in the boron foams (since boron is an efficient oxygen getter) up to 10-15% in atoms, and the presence of < 1% of magnesium arising from the boron target impurities. Regarding the hydrogen-enriched boron targets, the composition was estimated to be 41% H, 27% B, 21% C, 10% O and 1% Mg. The hydrogen content, which cannot be determined through EDXS, is estimated from the carbon content, under the hypothesis that the c:H ration in the film is the same as in the HDPE target. While a more detailed analysis would be needed to confirm the hypothesis, this a reasonable assumption considering the ablation regime of fs-PLD, where direct nanoparticle production is the main ablation mechanism. The outcome is a H:B ratio greater than unity, in the order of 1.5.

9.3 Experimental campaign results

The most interesting preliminary results from the experiment are obtained from the analysis of the CR-39 detectors, allowing an estimation of the alpha particle yield for the different kind of targets. They are reported in Figure 9.3, differentiating the results at low angles (45°) with those at high angles (80°), since the notable differences between the two can give valuable insights into the laser-matter interaction and subsequent alpha particle production.

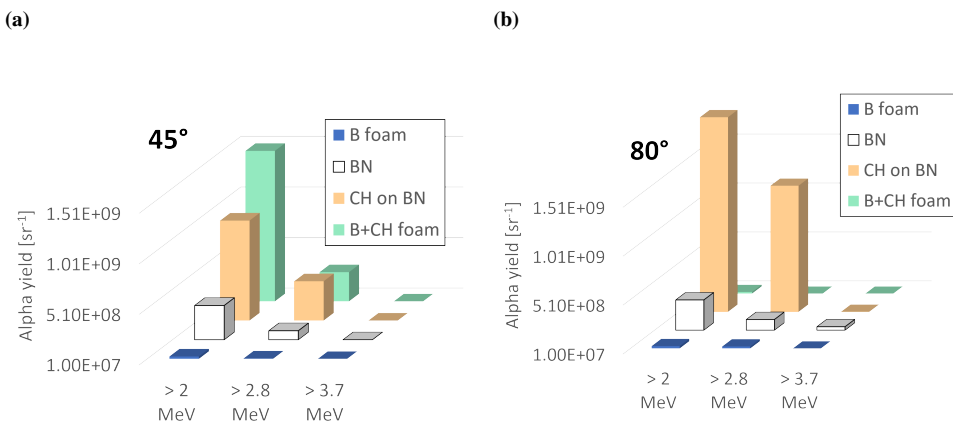


Figure 9.3: Alpha particle yield per shot for each sample category at different energy intervals, obtained from the analysis of CR-39 with different shielding thickness. The data at low angles (45°) is shown in (a), and at high angles (80°) in (b).

In the case of boron nanofoam, regardless of the angle, only a small number of alpha particles are found, close to the minimum detection threshold of 10^7 sr^{-1} or lower. This confirms the need for hydrogen enrichment, since the hydrogen impurities present in the foam are not sufficient to promote a relevant number of p-B fusion reactions. The results for the bare boron nitride targets are in accordance with literature data [97, 104, 195] when the yield is normalized to the laser energy—in the order of $5 \times 10^7 \text{ sr}^{-1} \text{ J}^{-1}$. For this specific material, a few % hydrogen impurities due to the fabrication process are believed to be the origin of the protons to sustain the fusion reactions. Interestingly, in this case similar results are obtained at low and high angles, in contrast with the foam samples. Moreover, this is the target presenting the higher fraction of alpha particles at higher energies, likely due to a TNSA-like field created at the front of the target that is able to accelerate the alpha particles. This mechanism is suppressed by the presence of a gradual den-

sity gradient in front of the target, which could be the reason it is not seen for the foam targets. A substantial increase in alpha particle production (up to $5 \times 10^8 \text{ sr}^{-1}$, or $5 \times 10^7 \text{ sr}^{-1} \text{ J}^{-1}$) is seen when a low-density nanostructured CH layer is deposited in front of the BN target, especially at high angles. This can be attributed to an efficient proton acceleration from the foam into the boron-containing substrate, in a hybrid scheme between the in-target and pitcher-catcher configurations. An analogous strong performance is shown by the hydrogen-enriched boron nanofoams, an even more interesting result considering the lower total number of boron atoms present due to the foam low density. Considering the target design, with a substrate not containing boron, a large number of fusion reactions happen in the foam plasma, with a possible contribution to ions acceleration given by the coulomb explosion of the nanoparticles composing the foam. This result is seen only on the low angle CR-39, while almost no alpha particle are able to reach the high angle detector. One possible explanation could be the high screening effect of the surrounding foam on the alpha particle emitted at high angles from deep within the foam, effect reduced at 45° . This is coherent with the absence of the effect for the BN targets.

The experimental results are indeed promising, with both target configurations—CH nanostructured coating on BN and hydrogen-enriched boron nanofoams—showing excellent performances in alpha particle production. The results confirm the validity of nanostructured material as laser-facing components in laser-matter interaction applications, and warrant further investigation and development in the target properties to capitalize on this first results and further optimize the targets. A deeper investigation if the experimental results, also aided by numerical simulations to explain the observed behaviour, would be particularly useful for any future development.



Part IV

Conclusions and perspectives

Conclusions and perspectives

Conclusions

This PhD thesis focuses on the production, characterization and experimental test of low-density nanostructured foams, as promising materials able to enhance laser absorption in laser-matter interaction applications. From inertial confinement fusion to laser-driven particle acceleration to proton-boron fusion, the optimization of the process is of central importance to overcome the present-day limitations, in light of the demanding requirements of the applications of greater societal relevance—such as clean energy production through nuclear fusion or hadrontherapy cancer treatment.

As illustrated in Chapter 3, nanofoams are promising materials both for their extremely low density—approaching the critical plasma density, thus allowing an efficient laser-plasma coupling—and due to their complex structure at the nanoscale, which also has an important influence in laser-matter interaction. For these reasons, proper control and tunability of material properties is key, and is the main topic addressed in Part II of this thesis. A comprehensive investigation of nanofoam production through Pulsed Laser Deposition (PLD), along with their characterization, is exploited for this aim.

First in Chapter 5 the production of carbon nanofoams through both ns-PLD and the unconventional fs-PLD is investigated, showing the evolution of material properties as a function of the main deposition parameters: the laser fluence and the background gas pressure. Among the two, the first one had a minor effect, while the second was the main driver behind the material structure and properties: the morphology evolved from compact films in vacuum to tree-like morphologies at intermediate pressures (50 Pa of argon), and finally gave rise to nanofoams at higher pressures. The film

average density, in great part consequence of its morphology, followed an analogous trend, with a sharp decrease in correspondence to the main morphological transition. An in-flight aggregation mechanism is confirmed for both techniques, and the fractal aggregate properties (nanoparticle radius, gyration radius and fractal dimension) are investigated in function of the same deposition parameters, establishing a qualitative relation between aggregate properties and nanofoam morphology and a quantitative one with nanofoam density. Raman characterization and EDXS mass thickness maps complete the characterization and support the other findings. Through the investigation into a well-known material (carbon), important insights into the deposition process were obtained, along with the differences—limited but significant—between ns and fs-PLD, such as lower uniformity and higher density at equal pressure for the latter.

Exploiting these insights, the analysis is extended to other elements (boron, silicon, copper, tungsten and gold) in Chapter 6, showing the great flexibility of fs-PLD in achieving nanofoams of materials with very different properties. Porous nanofoams up to 100s μm in thickness were successfully produced, with low density (10-100 mg/cm^3) and very similar morphology. The evolution of film density over background argon pressure followed an analogous behaviour than the case of carbon, hinting at the same aggregation mechanism. Thanks to the analysis for different elements with varying properties, the morphology evolution is explained through a simple model of the background gas slowing effect, where the nanoparticle size and density (along with the background pressure) are the main driving parameters. Interestingly, the direct production of nanoparticles in fs-PLD is confirmed by the nanoparticle-assembled films obtained in vacuum, with carbon being the only exception. Another relevant finding is the possibility to obtain nanofoam materials with the same fluence in fs-PLD, opening the possibility to produced mixed nanofoams through codeposition.

The investigation of nanofoam materials and their production through PLD is finally capitalized for the production of nanofoam-based targets for experimental laser-matter interaction campaigns, in the three fields introduced in Chapter 2: laser-driven particle acceleration, inertial confinement fusion (ICF) and proton-boron fusion. In Part III, the experimental campaigns are described, showing promising preliminary results (data analysis is still underway in all cases).

In Chapter 7, carbon nanofoam-based entirely produced double-layer targets (DLTs) are successfully exploited for proton acceleration, combining freestanding thin aluminum substrates (obtained with magnetron sputtering) with carbon nanofoams produced through ns-PLD. The campaign is carried out at the VEGA 3 petawatt-class laser at CLPU. The experimental test of the

DLT highlighted the great importance of both the target and its holder, especially considering the modification of adjacent regions of the target that can compromise subsequent shots. Preliminary data support an enhancement in maximum proton energies compared to bare targets, despite the results can be strongly influenced by the laser contrast.

Multiple kinds of carbon nanofoams, with varying morphology and density, are investigated as ablator material for inertial confinement fusion in Chapter 8. Both ns and fs-PLD produced foams are considered in a preparatory numerical investigation, with the two techniques able to produce nanofoams of the same density but different morphological features. A slower shockwave velocity, together with higher pressures at the shockfront are highlighted, with the higher density foams showing the best performance. An optimal foam thickness in the order of 150 μm leads to the maximum ablation loading enhancement. These results were exploited in the target design phase, and also considering the limited laser shot available, carbon nanofoams of different densities were produced through ns-PLD. The experimental activity performed at the high energy ABC laser gave promising results for the higher density (26 mg/cm^3) tree-like carbon films, that showed an increased laser energy absorption and improved ablation loading—demonstrated by the higher volume of the ablation crater on bulk substrates. Interestingly, lower density carbon nanofoams appeared transparent to the laser, despite the overcritical average density, likely due to the foam porous structure (not light-tight).

Finally, the potential of fs-PLD is fulfilled in the production of hydrogen-enriched boron nanofoam targets, by codeposition of boron and a polymer (HDPE). The targets are tested on the Taranis laser at the Queen's University Belfast laboratories, high intensity laser with \approx picosecond pulse duration. As detailed in Chapter 9, a significant enhancement of alpha particle yield was demonstrated for the mixed boron-CH nanofoam targets, when compared to boron nanofoams or boron nitride compact targets. Moreover, the data support the interpretation of fusion reactions happening in the foam, with a possible contribution due to the ions accelerated by coulomb explosion of the nanoparticles composing the nanofoam material.

As a last remark, it is worthwhile to consider that the three experiments were performed on quite different laser systems, each leading to distinct optimal target properties (such as nanofoam density and thickness): in laser-driven ion acceleration, where the TNSA is the main mechanism, the interaction of the high-intensity short-pulse laser with the solid foil is indeed necessary, thus the main purpose of the nanofoam coating is to enhance the hot electron generation, and lead to a tighter laser focusing through relativistic-self focusing effects. Therefore, a near critical density foam of some tens

of micrometers is ideal. On the contrary, in the ICF applications considered the carbon nanofoam should serve as ablator, with the purpose to increase the ablation loading on the substrate. Consequently, a total absorption of laser in the foam is advantageous in this case, and together with the higher laser energy and longer pulse duration it leads to the preference of higher density (20-50 mg/cm³) and higher thickness (hundreds of μm) foams. The proton-boron fusion experiment presents similar conditions, where all the laser should be absorbed in the foam in order to give energy to the boron ions and protons. In this case, higher densities lead also to higher reaction rate due to the increased concentration of reactants, and can sustain the interaction with the laser without premature plasma dispersion. Therefore, densities in the order of 100 mg/cm³ are coupled with hundreds of μm of thickness. This highlights once again the importance of a versatile technique for target production in laser-matter interaction applications.

Perspectives

Considering the variety of topics addressed in this PhD thesis, along with the promising results, there are many avenues worth to pursue in future works: first, the finalization of the data analysis of the three experiments, currently underway, with the aim to consolidate the preliminary results mentioned here.

In support of the comprehensive experimental work performed with PLD, a theoretical investigation into foam structure would be of particular interest: considering nanoparticles of different sizes as the basic constituents, and their aggregation into fractal aggregates exploiting diffusion-limited or reaction-limited cluster-cluster aggregation, or ballistic aggregation models, with the aim to reproduce the experimentally observed structures. This, together with a more in-depth investigation into the nature of ablated species with varying deposition conditions (i.e. through visible spectroscopy of the ablation plume, mass spectrometry of ablated species or few-shot deposition analysis), could deepen the understanding of the whole process, leading to a model able to predict the nanostructure properties starting from target material properties and deposition conditions. The fs-PLD in particular could be exploited even more extensively in the production of nanostructured low-density materials and nanofoams, enlarging the analysis to other elements, composites (such as oxides) and other codeposition possibility of specific applicative interest. Moreover, considering the experience gained thanks to the extensive experimental activity performed, some modification of the fs-PLD apparatus could be implemented to avoid the most common practical issues of the technique; for instance, the tendency to bore a hole in the target due

to the high deposition rate and small spot size could be limited with a larger relative speed of the laser on the target, or exploiting cylindrical targets.

Among the main remaining challenges for exploiting nanofoam-based targets for high-intensity laser-driven particle accelerators, the issues related to targetry and in particular target integrity and high repetition rate operation are of certain relevance. Nanofoam materials do not present high structural integrity, therefore two avenues of intervention could be related to proper target holder design to protect the neighbouring targets, or investigation into increasing the mechanical properties of the foam—such as thermal treatment or through chemical reaction, with potential impact on the foam structure. The work on carbon nanofoams as ablaters for ICF is just a first investigation, with much space for further experiments—for instance, studying a greater variety of foam properties, such as higher density or tuned density gradients. Considering the discrepancies between the preliminary 1D hydrodynamic simulations and the experimental results, 2D and/or 3D simulation including the foam structure would be of great help in understanding the physical processes taking place. Moreover, high-Z nanofoam (e.g. gold nanofoams) could be investigated for effective X-ray generation in indirect-drive ICF. Similar considerations are valid for the proton-boron fusion campaign, being an exploratory first experiment that also would benefit from the insights of a simulation campaign (e.g. for confirming and quantifying the contribution of coulomb explosion, or to determine the ideal B:H ratio in those conditions). Exploring different possibilities for hydrogen inclusion would also be of interest, in order to avoid or further reduce unwanted carbon/oxygen ions in the plasma, and overcome the difficulties connected with the fs-PLD codeposition of boron and HDPE.

Bibliography

- [1] Theodore H Maiman et al. Stimulated optical radiation in ruby. 1960.
- [2] Fred J McClung and Robert W Hellwarth. Giant optical pulsations from ruby. *Applied Optics*, 1(101):103–105, 1962.
- [3] LE Hargrove, Richard L Fork, and MA Pollack. Locking of he–ne laser modes induced by synchronous intracavity modulation. *Applied Physics Letters*, 5(1):4–5, 1964.
- [4] The Nobel Prize in Physics 2018. NobelPrize.org. Nobel Prize Outreach AB 2024. <https://www.nobelprize.org/prizes/physics/2018/press-release/>. [Online; accessed 23-Aug-2024].
- [5] Donna Strickland and Gerard Mourou. Compression of amplified chirped optical pulses. *Optics communications*, 55(6):447–449, 1985.
- [6] Jin Woo Yoon, Yeong Gyu Kim, Il Woo Choi, Jae Hee Sung, Hwang Woon Lee, Seong Ku Lee, and Chang Hee Nam. Realization of laser intensity over 10^{23} w/cm². *Optica*, 8(5):630–635, 2021.
- [7] ICUIL - International Committee on Ultra-High Intensity Lasers. <https://www.icuil.org/downloadss/laser-labs.html>. [Online; accessed 23-Aug-2024].
- [8] Zhaoyang Li, Yuxin Leng, and Ruxin Li. Further development of the short-pulse petawatt laser: Trends, technologies, and bottlenecks. *Laser & Photonics Reviews*, 17(1):2100705, 2023.
- [9] Andrew Harrison, Victor Malka, Daniele Margarone, and Katalin Varjú. Opening up high-performance laser science to the world at the extreme light infrastructure (eli). *Europhysics News*, 54(5):25–27, 2023.
- [10] Mary L Spaeth, KR Manes, DH Kalantar, PE Miller, JE Heebner, ES Bliss, DR Spec, TG Parham, PK Whitman, PJ Wegner, et al. Description of the nif laser. *Fusion Science and Technology*, 69(1):25–145, 2016.
- [11] P Vivini and M Nicolaizeau. The Imj: overview of recent advancements and very first experiments. *High Power Lasers for Fusion Research III*, 9345:934503, 2015.
- [12] Paul Gibbon. *Short pulse laser interactions with matter: an introduction*. World Scientific, 2005.
- [13] Eugene G Gamaly and Andrei V Rode. Physics of ultra-short laser interaction with matter: From phonon excitation to ultimate transformations. *Progress in Quantum Electronics*, 37(5):215–323, 2013.

Bibliography

- [14] Lorenzo Torrisi, A Borrielli, and D Margarone. Study on the ablation threshold induced by pulsed lasers at different wavelengths. *Nuclear Instruments and Methods in Physics Research Section B: Beam Interactions with Materials and Atoms*, 255(2):373–379, 2007.
- [15] Sivanandan S Harilal, Justin R Freeman, Prasoon K Diwakar, and Ahmed Hassanein. Femtosecond laser ablation: Fundamentals and applications. In *Laser-Induced Breakdown Spectroscopy: Theory and Applications*, pages 143–166. Springer, 2014.
- [16] Baerbel Rethfeld, Dmitriy S Ivanov, Martin E Garcia, and Sergei I Anisimov. Modelling ultrafast laser ablation. *Journal of Physics D: Applied Physics*, 50(19):193001, 2017.
- [17] Patrick Lorazo, Laurent J Lewis, and Michel Meunier. Short-pulse laser ablation of solids: from phase explosion to fragmentation. *Physical review letters*, 91(22):225502, 2003.
- [18] Antoine Rousse, Christian Rischel, S Fourmaux, Ingo Uschmann, Stéphane Sebban, G Grillon, Ph Balcou, Eckhart Förster, Jean-Paul Geindre, Patrick Audebert, et al. Non-thermal melting in semiconductors measured at femtosecond resolution. *Nature*, 410(6824):65–68, 2001.
- [19] Tobias Zier, Eeuwe S Zijlstra, Alan Kalitsov, Ioannis Theodonis, and Martin E Garcia. Signatures of nonthermal melting. *Structural Dynamics*, 2(5), 2015.
- [20] R Stoian, D Ashkenasi, A Rosenfeld, and EEB Campbell. Coulomb explosion in ultrashort pulsed laser ablation of Al₂O₃. *Physical review B*, 62(19):13167, 2000.
- [21] Michael NR Ashfold, Frederik Claeysens, Gareth M Fuge, and Simon J Henley. Pulsed laser ablation and deposition of thin films. *Chemical Society Reviews*, 33(1):23–31, 2004.
- [22] Daniel J Förster, Beat Jäggi, Andreas Michalowski, and Beat Neuenschwander. Review on experimental and theoretical investigations of ultra-short pulsed laser ablation of metals with burst pulses. *Materials*, 14(12):3331, 2021.
- [23] M Capitelli, A Casavola, G Colonna, and AJSAPBAS De Giacomo. Laser-induced plasma expansion: theoretical and experimental aspects. *Spectrochimica Acta Part B: Atomic Spectroscopy*, 59(3):271–289, 2004.
- [24] SM Hankin, DM Villeneuve, PB Corkum, and DM Rayner. Intense-field laser ionization rates in atoms and molecules. *Physical Review A*, 64(1):013405, 2001.
- [25] Thomas James Morrow Boyd and Jeffrey John Sanderson. *The physics of plasmas*. Cambridge university press, 2003.
- [26] A Pukhov and J Meyer-ter Vehn. Relativistic magnetic self-channeling of light in near-critical plasma: three-dimensional particle-in-cell simulation. *Physical review letters*, 76(21):3975, 1996.
- [27] C Gahn, GD Tsakiris, A Pukhov, J Meyer-ter Vehn, G Pretzler, P Thirolf, D Habs, and KJ Witte. Multi-MeV electron beam generation by direct laser acceleration in high-density plasma channels. *Physical Review Letters*, 83(23):4772, 1999.
- [28] Hiroyuki Daido, Mamiko Nishiuchi, and Alexander S Pirozhkov. Review of laser-driven ion sources and their applications. *Reports on progress in physics*, 75(5):056401, 2012.
- [29] Simon Martin Hooker. Developments in laser-driven plasma accelerators. *Nature Photonics*, 7(10):775–782, 2013.
- [30] William Kruer. *The physics of laser plasma interactions*. CRC Press, 2019.
- [31] W Seka, DH Edgell, JF Myatt, AV Maximov, RW Short, VN Goncharov, and HA Baldis. Two-plasmon-decay instability in direct-drive inertial confinement fusion experiments. *Physics of Plasmas*, 16(5), 2009.
- [32] M Cipriani, S Yu Gusakov, F Consoli, R De Angelis, AA Rupasov, P Andreoli, G Cristofari, G Di Giorgio, and M Salvadori. Time-dependent measurement of high-power laser light reflection by low-Z foam plasma. *High Power Laser Science and Engineering*, 9:e40, 2021.

- [33] DW Forslund, JM Kindel, and EL Lindman. Theory of stimulated scattering processes in laser-irradiated plasmas. *The Physics of Fluids*, 18(8):1002–1016, 1975.
- [34] Fabrizio Consoli, Vladimir T Tikhonchuk, Matthieu Bardon, Philip Bradford, David C Carroll, Jakub Cikhardt, Mattia Cipriani, Robert J Clarke, Thomas E Cowan, Colin N Danson, et al. Laser produced electromagnetic pulses: generation, detection and mitigation. *High Power Laser Science and Engineering*, 8:e22, 2020.
- [35] François Amiranoff, S Baton, D Bernard, B Cros, D Descamps, F Dorchie, F Jacquet, Victor Malka, JR Marques, G Mattheussent, et al. Observation of laser wakefield acceleration of electrons. *Physical Review Letters*, 81(5):995, 1998.
- [36] Toshiki Tajima, XQ Yan, and T Ebisuzaki. Wakefield acceleration. *Reviews of Modern Plasma Physics*, 4(1):7, 2020.
- [37] GA Bagdasarov, PV Sasorov, VA Gasilov, AS Boldarev, OG Olkhovskaya, Carlo Benedetti, SS Bulanov, A Gonsalves, H-S Mao, Carl B Schroeder, et al. Laser beam coupling with capillary discharge plasma for laser wakefield acceleration applications. *Physics of Plasmas*, 24(8), 2017.
- [38] EL Clark, K Krushelnick, JR Davies, Matthew Zepf, M Tatarakis, FN Beg, A Machacek, PA Norreys, MIK Santala, I Watts, et al. Measurements of energetic proton transport through magnetized plasma from intense laser interactions with solids. *Physical Review Letters*, 84(4):670, 2000.
- [39] Anatoly Maksimchuk, Shaoting Gu, Kirk Flippo, Donald Umstadter, and V Yu Bychenkov. Forward ion acceleration in thin films driven by a high-intensity laser. *Physical Review Letters*, 84(18):4108, 2000.
- [40] RA Snavely, MH Key, SP Hatchett, TE Cowan, Markus Roth, TW Phillips, MA Stoyer, EA Henry, TC Sangster, MS Singh, et al. Intense high-energy proton beams from petawatt-laser irradiation of solids. *Physical review letters*, 85(14):2945, 2000.
- [41] Andrea Macchi, Marco Borghesi, and Matteo Passoni. Ion acceleration by superintense laser-plasma interaction. *Reviews of Modern Physics*, 85(2):751, 2013.
- [42] J Badziak. Laser-driven ion acceleration: methods, challenges and prospects. In *Journal of Physics: Conference Series*, volume 959, page 012001. IOP Publishing, 2018.
- [43] M Nishiuchi, NP Dover, M Hata, H Sakaki, Ko Kondo, HF Lowe, T Miyahara, H Kiriyama, JK Koga, N Iwata, et al. Dynamics of laser-driven heavy-ion acceleration clarified by ion charge states. *Physical Review Research*, 2(3):033081, 2020.
- [44] Muhammad Noaman-ul Haq, Hamad Ahmed, Thomas Sokollik, Lule Yu, Zezhou Liu, Xiaohui Yuan, Fang Yuan, Mohammad Mirzaie, Xulei Ge, Liming Chen, et al. Statistical analysis of laser driven protons using a high-repetition-rate tape drive target system. *Physical Review Accelerators and Beams*, 20(4):041301, 2017.
- [45] M Borghesi, A Bigongiari, S Kar, A Macchi, L Romagnani, P Audebert, J Fuchs, T Toncian, O Willi, SV Bulanov, et al. Laser-driven proton acceleration: source optimization and radiographic applications. *Plasma Physics and Controlled Fusion*, 50(12):124040, 2008.
- [46] Gianluca Sarri, CA Cecchetti, R Jung, P Hobbs, S James, J Lockyear, RM Stevenson, Domenico Doria, DJ Hoarty, O Willi, et al. Spatially resolved measurements of laser filamentation in long scale length underdense plasmas with and without beam smoothing. *Physical Review Letters*, 106(9):095001, 2011.
- [47] CAJ Palmer, PT Campbell, Yong Ma, Luca Antonelli, AFA Bott, Gianluca Gregori, James Halliday, Yiftak Katzir, Peter Kordell, Karl Krushelnick, et al. Field reconstruction from proton radiography of intense laser driven magnetic reconnection. *Physics of Plasmas*, 26(8), 2019.

Bibliography

- [48] Sachie Kimura and Aldo Bonasera. Deuteron-induced reactions generated by intense lasers for pet isotope production. *Nuclear Instruments and Methods in Physics Research Section A: Accelerators, Spectrometers, Detectors and Associated Equipment*, 637(1):164–170, 2011.
- [49] Zhanliang Sun. Production of nuclear medicine radioisotopes with ultra-intense lasers. *AIP Advances*, 11(4), 2021.
- [50] Ken WD Ledingham, Paul R Bolton, Naoya Shikazono, and C-M Charlie Ma. Towards laser driven hadron cancer radiotherapy: A review of progress. *Applied Sciences*, 4(3):402–443, 2014.
- [51] Pankaj Chaudhary, Giuliana Milluzzo, Hamad Ahmed, Boris Odlozilik, Aaron McMurray, Kevin M Prise, and Marco Borghesi. Radiobiology experiments with ultra-high dose rate laser-driven protons: methodology and state-of-the-art. *Frontiers in Physics*, 9:624963, 2021.
- [52] V Yu Bychenkov, VT Tikhonchuk, and SV Tolokonnikov. Nuclear reactions triggered by laser-accelerated high-energy ions. *Journal of Experimental and Theoretical Physics*, 88:1137–1142, 1999.
- [53] Changbo Fu, Jie Bao, Liming Chen, Jianjun He, Long Hou, Liang Li, Yanfei Li, Yutong Li, Guoqian Liao, Yongjoo Rhee, et al. Laser-driven plasma collider for nuclear studies. *Science bulletin*, 60:1211–1213, 2015.
- [54] Bruce A Remington, David Arnett, R Paul, Drake, and Hideaki Takabe. Modeling astrophysical phenomena in the laboratory with intense lasers. *Science*, 284(5419):1488–1493, 1999.
- [55] Hideaki Takabe and Yasuhiro Kuramitsu. Recent progress of laboratory astrophysics with intense lasers. *High Power Laser Science and Engineering*, 9:e49, 2021.
- [56] W Bang, BJ Albright, PA Bradley, EL Vold, JC Boettger, and JC Fernandez. Uniform heating of materials into the warm dense matter regime with laser-driven quasimonoenergetic ion beams. *Physical Review E*, 92(6):063101, 2015.
- [57] David Riley. Generation and characterisation of warm dense matter with intense lasers. *Plasma Physics and Controlled Fusion*, 60(1):014033, 2017.
- [58] M Roth, D Jung, K Falk, N Guler, O Deppert, M Devlin, A Favalli, J Fernandez, D Gautier, M Geissel, et al. Bright laser-driven neutron source based on the relativistic transparency of solids. *Physical review letters*, 110(4):044802, 2013.
- [59] Annika Kleinschmidt, V Bagnoud, O Deppert, Andrea Favalli, S Frydrych, J Hornung, D Jahn, G Schaumann, A Tebartz, F Wagner, et al. Intense, directed neutron beams from a laser-driven neutron source at phelix. *Physics of Plasmas*, 25(5), 2018.
- [60] AJ Mackinnon, PK Patel, M Borghesi, RC Clarke, RR Freeman, H Habara, SP Hatchett, D Hey, DG Hicks, S Kar, et al. Proton radiography of a laser-driven implosion. *Physical review letters*, 97(4):045001, 2006.
- [61] CM Brenner, SR Mirfayzi, DR Rusby, C Armstrong, A Alejo, LA Wilson, R Clarke, H Ahmed, NMH Butler, D Haddock, et al. Laser-driven x-ray and neutron source development for industrial applications of plasma accelerators. *Plasma Physics and Controlled Fusion*, 58(1):014039, 2015.
- [62] Marianna Barberio, S Veltri, Massimiliano Sciscio, and Patrizio Antici. Laser-accelerated proton beams as diagnostics for cultural heritage. *Scientific Reports*, 7(1):40415, 2017.
- [63] Matteo Passoni, Luca Fedeli, and Francesco Mirani. Superintense laser-driven ion beam analysis. *Scientific reports*, 9(1):9202, 2019.
- [64] F Mirani, A Maffini, F Casamichiela, A Pazzaglia, A Formenti, D Dellasega, V Russo, D Vavasori, D Bortot, M Huault, et al. Integrated quantitative pixe analysis and edx spectroscopy using a laser-driven particle source. *Science advances*, 7(3):eabc8660, 2021.

- [65] TM Ostermayr, C Kreuzer, FS Englbrecht, J Gebhard, J Hartmann, A Huebl, D Haffa, P Hilz, K Parodi, J Wenz, et al. Laser-driven x-ray and proton micro-source and application to simultaneous single-shot bi-modal radiographic imaging. *Nature communications*, 11(1):6174, 2020.
- [66] J Braenzel, AA Andreev, K Platonov, M Klingsporn, L Ehrentraut, W Sandner, and M Schnürer. Coulomb-driven energy boost of heavy ions for laser-plasma acceleration. *Physical review letters*, 114(12):124801, 2015.
- [67] Adam Higginson, RJ Gray, Martin King, RJ Dance, SDR Williamson, NMH Butler, Robbie Wilson, Rémi Capdessus, Chris Armstrong, JS Green, et al. Near-100 mev protons via a laser-driven transparency-enhanced hybrid acceleration scheme. *Nature communications*, 9(1):724, 2018.
- [68] Malte Kaluza, Jörg Schreiber, Marko IK Santala, George D Tsakiris, Klaus Eidmann, Jürgen Meyer-ter Vehn, and Klaus J Witte. Influence of the laser prepulse on proton acceleration in thin-foil experiments. *Physical review letters*, 93(4):045003, 2004.
- [69] T Ceccotti, A Lévy, H Popescu, F Réau, P dâOliveira, P Monot, JP Geindre, E Lefebvre, and Ph Martin. Proton acceleration with high-intensity ultrahigh-contrast laser pulses. *Physical review letters*, 99(18):185002, 2007.
- [70] P McKenna, DC Carroll, Olle Lundh, F Nürnberg, Keith Markey, S Bandyopadhyay, D Batani, RG Evans, R Jafer, Saty Kar, et al. Effects of front surface plasma expansion on proton acceleration in ultraintense laser irradiation of foil targets. *Laser and Particle Beams*, 26(4):591–596, 2008.
- [71] F Wagner, CP João, J Fils, T Gottschall, J Hein, J Körner, J Limpert, M Roth, T Stöhlker, and V Bagnoud. Temporal contrast control at the phelix petawatt laser facility by means of tunable sub-picosecond optical parametric amplification. *Applied physics B*, 116:429–435, 2014.
- [72] Cédric Thauray, Fabien Quere, J-P Geindre, Anna Levy, Tiberio Ceccotti, P Monot, Michel Bougeard, F Réau, P dâOliveira, Patrick Audebert, et al. Plasma mirrors for ultrahigh-intensity optics. *Nature Physics*, 3(6):424–429, 2007.
- [73] S Buffechoux, J Psikal, M Nakatsutsumi, L Romagnani, A Andreev, K Zeil, M Amin, P Antici, T Burris-Mog, A Compant-La-Fontaine, et al. Hot electrons transverse refluxing in ultraintense laser-solid interactions. *Physical review letters*, 105(1):015005, 2010.
- [74] SA Gaillard, T Kluge, KA Flippo, M Bussmann, B Gall, T Lockard, M Geissel, DT Offermann, M Schollmeier, Y Sentoku, et al. Increased laser-accelerated proton energies via direct laser-light-pressure acceleration of electrons in microcone targets. *Physics of Plasmas*, 18(5), 2011.
- [75] Satyabrata Kar, Hamad Ahmed, Rajendra Prasad, Mirela Cerchez, Stephanie Brauckmann, Bastian Aurand, Giada Cantono, Prokopis Hadjisolomou, Ciaran LS Lewis, Andrea Macchi, et al. Guided post-acceleration of laser-driven ions by a miniature modular structure. *Nature communications*, 7(1):10792, 2016.
- [76] D Margarone, O Klimo, IJ Kim, J Prokpek, J Limpouch, TM Jeong, T Mocek, J Pšikal, HT Kim, J Proška, et al. Laser-driven proton acceleration enhancement by nanostructured foils. *Physical review letters*, 109(23):234801, 2012.
- [77] M Blanco, María Teresa Flores-Arias, C Ruiz, and M Vranic. Table-top laser-based proton acceleration in nanostructured targets. *New Journal of Physics*, 19(3):033004, 2017.
- [78] E Yazdani, R Sadighi-Bonabi, H Afarideh, J Yazdanpanah, and H Hora. Enhanced laser ion acceleration with a multi-layer foam target assembly. *Laser and Particle Beams*, 32(4):509–515, 2014.
- [79] Irene Prencipe, A Sgattoni, David Dellasega, Luca Fedeli, Lorenzo Cialfi, Il Woo Choi, I Jong Kim, Karol Adam Janulewicz, KF Kakolee, Hwang Woon Lee, et al. Development of foam-based layered targets for laser-driven ion beam production. *Plasma Physics and Controlled Fusion*, 58(3):034019, 2016.

Bibliography

- [80] Elkhan Richard Sadik-Zada, Andrea Gatto, and Yannic Weißnicht. Back to the future: Revisiting the perspectives on nuclear fusion and juxtaposition to existing energy sources. *Energy*, page 129150, 2023.
- [81] Samuele Meschini, Francesco Laviano, Federico Ledda, Davide Pettinari, Raffella Testoni, Daniele Torsello, and Bruno Panella. Review of commercial nuclear fusion projects. *Frontiers in Energy Research*, 11:1157394, 2023.
- [82] Jeffrey P Freidberg. *Plasma physics and fusion energy*. Cambridge university press, 2008.
- [83] Jozef Ongena, R Koch, R Wolf, and H Zohm. Magnetic-confinement fusion. *Nature Physics*, 12(5):398–410, 2016.
- [84] Norbert Holtkamp, ITER Project Team, et al. An overview of the iter project. *Fusion Engineering and Design*, 82(5-14):427–434, 2007.
- [85] R Betti and OA Hurricane. Inertial-confinement fusion with lasers. *Nature Physics*, 12(5):435–448, 2016.
- [86] Roy Kishony and Dov Shvarts. Ignition condition and gain prediction for perturbed inertial confinement fusion targets. *Physics of Plasmas*, 8(11):4925–4936, 2001.
- [87] RS Craxton, KS Anderson, TR Boehly, VN Goncharov, DR Harding, JP Knauer, RL McCrory, PW McKenty, DD Meyerhofer, JF Myatt, et al. Direct-drive inertial confinement fusion: A review. *Physics of Plasmas*, 22(11), 2015.
- [88] John Lindl. Development of the indirect-drive approach to inertial confinement fusion and the target physics basis for ignition and gain. *Physics of plasmas*, 2(11):3933–4024, 1995.
- [89] Max Tabak, James Hammer, Michael E Glinsky, William L Kruer, Scott C Wilks, John Woodworth, E Michael Campbell, Michael D Perry, and Rodney J Mason. Ignition and high gain with ultrapowerful lasers. *Physics of Plasmas*, 1(5):1626–1634, 1994.
- [90] Stefano Atzeni, X Ribeyre, G Schurtz, AJ Schmitt, B Canaud, R Betti, and LJ Perkins. Shock ignition of thermonuclear fuel: principles and modelling. *Nuclear fusion*, 54(5):054008, 2014.
- [91] D Batani, S Baton, A Casner, S Depierreux, M Hohenberger, O Klimo, M Koenig, C Labaune, X Ribeyre, C Rousseaux, et al. Physics issues for shock ignition. *Nuclear Fusion*, 54(5):054009, 2014.
- [92] H Abu-Shawareb, R Acree, P Adams, J Adams, B Addis, R Aden, P Adrian, BB Afeyan, M Aggleton, L Aghaian, et al. Achievement of target gain larger than unity in an inertial fusion experiment. *Physical Review Letters*, 132(6):065102, 2024.
- [93] H Abu-Shawareb, R Acree, P Adams, J Adams, B Addis, R Aden, 2P Adrian, BB Afeyan, M Aggleton, L Aghaian, et al. Lawson criterion for ignition exceeded in an inertial fusion experiment. *Physical review letters*, 129(7):075001, 2022.
- [94] Dimitri Batani, Arnaud Colaitis, Fabrizio Consoli, Colin N Danson, Leonida Antonio Gizzi, Javier Honrubia, Thomas Kühn, Sebastien Le Pape, Jean-Luc Miquel, Jose Manuel Perlado, et al. Future for inertial-fusion energy in europe: a roadmap. *High Power Laser Science and Engineering*, 11:e83, 2023.
- [95] S Stave, MW Ahmed, RH France III, SS Henshaw, B Müller, BA Perdue, RM Prior, MC Spraker, and HR Weller. Understanding the b11 (p, α) $\alpha\alpha$ reaction at the 0.675 mev resonance. *Physics Letters B*, 696(1-2):26–29, 2011.
- [96] William M Nevins. A review of confinement requirements for advanced fuels. *Journal of Fusion Energy*, 17(1):25–32, 1998.
- [97] Daniele Margarone, Julien Bonnalet, Lorenzo Giuffrida, Alessio Morace, Vasiliki Kantarelou, Marco Tosca, Didier Raffestin, Philippe Nicolai, Antonino Picciotto, Yuki Abe, et al. In-target proton–boron nuclear fusion using a pw-class laser. *Applied sciences*, 12(3):1444, 2022.

- [98] Warren McKenzie, Dimitri Batani, Thomas A Mehlhorn, Daniele Margarone, Fabio Belloni, E Michael Campbell, Simon Woodruff, Jan Kirchhoff, Adrian Paterson, Sergey Pikuz, et al. Hb11â understanding hydrogen-boron fusion as a new clean energy source. *Journal of Fusion Energy*, 42(1):17, 2023.
- [99] Antonino Picciotto, D Margarone, A Velyhan, P Bellutti, J Krasa, A Szydłowski, Giuseppe Bertuccio, Yongbiao Shi, A Mangione, J Prokupek, et al. Boron-proton nuclear-fusion enhancement induced in boron-doped silicon targets by low-contrast pulsed laser. *Physical Review X*, 4(3):031030, 2014.
- [100] GAP Cirrone, L Manti, D Margarone, G Petringa, L Giuffrida, A Minopoli, A Picciotto, G Russo, F Cammarata, P Pisciotto, et al. First experimental proof of proton boron capture therapy (pbct) to enhance protontherapy effectiveness. *Scientific Reports*, 8(1):1141, 2018.
- [101] Nhan Hau Tran, Tatiana Shtam, Yaroslav Yu Marchenko, Andrey L Konevega, and Dmitry Lebedev. Current state and perspectives for proton boron capture therapy. *Biomedicines*, 11(6):1727, 2023.
- [102] Pavel Bláha, Chiara Feoli, Stefano Agosteo, Marco Calvaruso, Francesco Paolo Cammarata, Roberto Catalano, Mario Ciocca, Giuseppe Antonio Pablo Cirrone, Valeria Conte, Giacomo Cuttone, et al. The proton-boron reaction increases the radiobiological effectiveness of clinical low-and high-energy proton beams: novel experimental evidence and perspectives. *Frontiers in Oncology*, 11:682647, 2021.
- [103] C Labaune, C Baccou, S Depierreux, C Goyon, G Loisel, V Yahia, and J Rafelski. Fusion reactions initiated by laser-accelerated particle beams in a laser-produced plasma. *Nature Communications*, 4(1):2506, 2013.
- [104] Lorenzo Giuffrida, Fabio Belloni, Daniele Margarone, Giada Petringa, Giuliana Milluzzo, Valentina Scuderi, Andriy Velyhan, Marcin Rosinski, Antonino Picciotto, Milan Kucharik, et al. High-current stream of energetic α particles from laser-driven proton-boron fusion. *Physical Review E*, 101(1):013204, 2020.
- [105] Valeriia Istokskaia, Marco Tosca, Lorenzo Giuffrida, Jan Psikal, Filip Grepl, Vasiliki Kantarelou, Stanislav Stancek, Sabrina Di Siena, Arsenios Hadjikyriacou, Aodhan McIlvenny, et al. A multi-mev alpha particle source via proton-boron fusion driven by a 10-gw tabletop laser. *Communications Physics*, 6(1):27, 2023.
- [106] Mihail C Roco. The long view of nanotechnology development: the national nanotechnology initiative at 10 years, 2011.
- [107] Philip Moriarty. Nanostructured materials. *Reports on Progress in Physics*, 64(3):297, 2001.
- [108] Bharat Bhushan. *Springer handbook of nanotechnology*. Springer, 2017.
- [109] Herbert Gleiter. Nanostructured materials: basic concepts and microstructure. *Acta materialia*, 48(1):1–29, 2000.
- [110] Bing Q Han, Enrique J Lavernia, Farghalli A Mohamed, et al. Mechanical properties of nanostructured materials. *Rev. Adv. Mater. Sci*, 9(1):1–16, 2005.
- [111] Xinghang Zhang, Khalid Hattar, Youxing Chen, Lin Shao, Jin Li, Cheng Sun, Kaiyuan Yu, Nan Li, Mitra L Taheri, Haiyan Wang, et al. Radiation damage in nanostructured materials. *Progress in Materials Science*, 96:217–321, 2018.
- [112] Gerasimos Konstantatos and Edward H Sargent. Nanostructured materials for photon detection. *Nature nanotechnology*, 5(6):391–400, 2010.
- [113] François Flory, Ludovic Escoubas, and Gérard Berginc. Optical properties of nanostructured materials: a review. *Journal of Nanophotonics*, 5(1):052502–052502, 2011.

Bibliography

- [114] M Martínez-Calderon, A Rodríguez, A Dias-Ponte, MC Morant-Miñana, M Gómez-Aranzadi, and SM Olaizola. Femtosecond laser fabrication of highly hydrophobic stainless steel surface with hierarchical structures fabricated by combining ordered microstructures and lipss. *Applied Surface Science*, 374:81–89, 2016.
- [115] Tao Xu, Ning Zhang, Heather L Nichols, Donglu Shi, and Xuejun Wen. Modification of nanostructured materials for biomedical applications. *Materials Science and Engineering: C*, 27(3):579–594, 2007.
- [116] Peter Koegler, Andrew Clayton, Helmut Thissen, Gil Nonato C Santos, and Peter Kingshott. The influence of nanostructured materials on biointerfacial interactions. *Advanced drug delivery reviews*, 64(15):1820–1839, 2012.
- [117] Kui-Qing Peng, Xin Wang, and Shuit-Tong Lee. Gas sensing properties of single crystalline porous silicon nanowires. *Applied Physics Letters*, 95(24), 2009.
- [118] Jin-Song Hu, Ling-Ling Ren, Yu-Guo Guo, Han-Pu Liang, An-Min Cao, Li-Jun Wan, and Chun-Li Bai. Mass production and high photocatalytic activity of zns nanoporous nanoparticles. *Angewandte chemie*, 117(8):1295–1299, 2005.
- [119] Heon-Cheol Shin and Meilin Liu. Copper foam structures with highly porous nanostructured walls. *Chemistry of materials*, 16(25):5460–5464, 2004.
- [120] Yung Chiun Her and Sing Lin Huang. Growth mechanism of te nanotubes by a direct vapor phase process and their room-temperature co and no2 sensing properties. *Nanotechnology*, 24(21):215603, 2013.
- [121] R Abdel-Karim, Y Reda, and A Abdel-Fattah. Nanostructured materials-based nanosensors. *Journal of The Electrochemical Society*, 167(3):037554, 2020.
- [122] Xueqiang Zhang, Xinbing Cheng, and Qiang Zhang. Nanostructured energy materials for electrochemical energy conversion and storage: a review. *Journal of energy chemistry*, 25(6):967–984, 2016.
- [123] N Raveendran Shiju and Vadim V Gulians. Recent developments in catalysis using nanostructured materials. *Applied Catalysis A: General*, 356(1):1–17, 2009.
- [124] Francisco Zaera. Nanostructured materials for applications in heterogeneous catalysis. *Chemical Society Reviews*, 42(7):2746–2762, 2013.
- [125] Chunping Xu, Prasaanth Ravi Anusuyadevi, Cyril Aymonier, Rafael Luque, and Samuel Marre. Nanostructured materials for photocatalysis. *Chemical Society Reviews*, 48(14):3868–3902, 2019.
- [126] Antonino Salvatore Arico, Peter Bruce, Bruno Scrosati, Jean-Marie Tarascon, and Walter Van Schalkwijk. Nanostructured materials for advanced energy conversion and storage devices. *Nature materials*, 4(5):366–377, 2005.
- [127] WP Steckle, JR Schoonover, NE Lanier, and A Nobile. Dopeable styrenic foams used in inertial fusion targets. *Journal of materials science*, 41:4055–4060, 2006.
- [128] Lin Zhang, Xuan Luo, Yongheng Fan, Kai Du, and Qiang Yin. Development of perdeuterated polymer foams for inertial confinement fusion targets in china. *Plasma and Fusion Research*, 4:S1005–S1005, 2009.
- [129] Dustin A Gilbert, Edward C Burks, Sergey V Ushakov, Patricia Abellan, Ilke Arslan, Thomas E Felter, Alexandra Navrotsky, and Kai Liu. Tunable low density palladium nanowire foams. *Chemistry of Materials*, 29(22):9814–9818, 2017.
- [130] Jiaying Huang, Shabnam Virji, Bruce H Weiller, and Richard B Kaner. Nanostructured polyaniline sensors. *Chemistry—A European Journal*, 10(6):1314–1319, 2004.
- [131] Sergei Yu Gus' kov and Vladislav B Rozanov. Interaction of laser radiation with a porous medium and formation of a nonequilibrium plasma. *Quantum Electronics*, 27(8):696, 1997.

- [132] M Cipriani, S Yu Gus'kov, R De Angelis, F Consoli, AA Rupasov, P Andreoli, G Cristofari, G Di Giorgio, and F Ingenito. Laser-supported hydrothermal wave in low-dense porous substance. *Laser and Particle Beams*, 36(1):121–128, 2018.
- [133] Alessandro Zani, David Dellasega, Valeria Russo, and Matteo Passoni. Ultra-low density carbon foams produced by pulsed laser deposition. *Carbon*, 56:358–365, 2013.
- [134] Andrei V Rode, ST Hyde, EG Gamaly, RG Elliman, DR McKenzie, and S Bulcock. Structural analysis of a carbon foam formed by high pulse-rate laser ablation. *Applied Physics A*, 69:S755–S758, 1999.
- [135] Irene Prencipe, Josefina Metzkes-Ng, Andrea Pazzaglia, Constantin Bernert, David Dellasega, Luca Fedeli, Arianna Formenti, Marco Garten, Thomas Kluge, Stephan Kraft, et al. Efficient laser-driven proton and bremsstrahlung generation from cluster-assembled foam targets. *New Journal of Physics*, 23(9):093015, 2021.
- [136] Matteo Passoni, FM Arioli, Lorenzo Cialfi, David Dellasega, Luca Fedeli, Arianna Formenti, Anna Chiara Giovannelli, Alessandro Maffini, Francesco Mirani, Andrea Pazzaglia, et al. Advanced laser-driven ion sources and their applications in materials and nuclear science. *Plasma Physics and Controlled Fusion*, 62(1):014022, 2019.
- [137] Cosima Stubenrauch, Angelika Menner, Alexander Bismarck, and Wiebke Drenckhan. Emulsion and foam templating—promising routes to tailor-made porous polymers. *Angewandte Chemie International Edition*, 57(32):10024–10032, 2018.
- [138] Huaping Zhao, Min Zhou, Liaoyong Wen, and Yong Lei. Template-directed construction of nanostructure arrays for highly-efficient energy storage and conversion. *Nano Energy*, 13:790–813, 2015.
- [139] Bryce C Tappan, Stephen A Steiner III, and Erik P Luther. Nanoporous metal foams. *Angewandte Chemie International Edition*, 49(27):4544–4565, 2010.
- [140] Geon Dae Moon, Sungwook Ko, Yuho Min, Jie Zeng, Younan Xia, and Unyong Jeong. Chemical transformations of nanostructured materials. *Nano Today*, 6(2):186–203, 2011.
- [141] Michael S Silverstein. Polyhipes: Recent advances in emulsion-templated porous polymers. *Progress in Polymer Science*, 39(1):199–234, 2014.
- [142] Yiding Liu, James Goebel, and Yadong Yin. Templated synthesis of nanostructured materials. *Chemical Society Reviews*, 42(7):2610–2653, 2013.
- [143] Dingcai Wu, Fei Xu, Bin Sun, Ruowen Fu, Hongkun He, and Krzysztof Matyjaszewski. Design and preparation of porous polymers. *Chemical reviews*, 112(7):3959–4015, 2012.
- [144] Dmitry Bokov, Abduladheem Turki Jalil, Supat Chupradit, Wanich Suksatan, Mohammad Javed Ansari, Iman H Shewael, Gabdrakhman H Valiev, and Ehsan Kianfar. Nanomaterial by sol-gel method: synthesis and application. *Advances in Materials Science and Engineering*, 2021:1–21, 2021.
- [145] Jin Ho Bang and Kenneth S Suslick. Applications of ultrasound to the synthesis of nanostructured materials. *Advanced materials*, 22(10):1039–1059, 2010.
- [146] Heberton Wender, Pedro Migowski, Adriano F Feil, Sergio R Teixeira, and Jairton Dupont. Sputtering deposition of nanoparticles onto liquid substrates: Recent advances and future trends. *Coordination Chemistry Reviews*, 257(17-18):2468–2483, 2013.
- [147] S Anu Mary Ealia and Manickam Puratchiveeran Saravanakumar. A review on the classification, characterisation, synthesis of nanoparticles and their application. In *IOP conference series: materials science and engineering*, volume 263, page 032019. IOP Publishing, 2017.
- [148] Adawiya J Haider, Taif Alawsai, Mohammed J Haider, Bakr Ahmed Taha, and Haydar Abdulameer Marhoon. A comprehensive review on pulsed laser deposition technique to effective nanostructure production: Trends and challenges. *Optical and Quantum Electronics*, 54(8):488, 2022.

Bibliography

- [149] James A Greer. History and current status of commercial pulsed laser deposition equipment. *Journal of Physics D: Applied Physics*, 47(3):034005, 2013.
- [150] Andrei V Rode, Eugene G Gamaly, and Barry Luther-Davies. Formation of cluster-assembled carbon nano-foam by high-repetition-rate laser ablation. *Applied Physics A*, 70:135–144, 2000.
- [151] A Maffini, A Pazzaglia, D Dellasega, V Russo, and M Passoni. Growth dynamics of pulsed laser deposited nanofoams. *Physical Review Materials*, 3(8):083404, 2019.
- [152] AA Voevodin and MS Donley. Preparation of amorphous diamond-like carbon by pulsed laser deposition: a critical review. *Surface and Coatings Technology*, 82(3):199–213, 1996.
- [153] Paul Meakin. Models for colloidal aggregation. *Annual Review of Physical Chemistry*, 39(1):237–267, 1988.
- [154] Tamás Vicsek. *Fractal growth phenomena*. World scientific, 1992.
- [155] JH Bin, WJ Ma, HY Wang, MJV Streeter, C Kreuzer, D Kiefer, M Yeung, S Cousens, PS Foster, B Dromey, et al. Ion acceleration using relativistic pulse shaping in near-critical-density plasmas. *Physical review letters*, 115(6):064801, 2015.
- [156] M Olazabal-Loumé, Ph Nicolai, G Riazuelo, M Grech, J Breil, S Fujioka, A Sunahara, N Borisenko, and VT Tikhonchuk. Simulations of laser imprint reduction using underdense foams and its consequences on the hydrodynamic instability growth. *New Journal of Physics*, 15(8):085033, 2013.
- [157] R De Angelis, F Consoli, S Yu Gus' kov, AA Rupasov, P Andreoli, G Cristofari, and G Di Giorgio. Laser-ablated loading of solid target through foams of overcritical density. *Physics of Plasmas*, 22(7), 2015.
- [158] Lu Zhang, Yongkun Ding, Zhiwei Lin, Hang Li, Longfei Jing, Zheng Yuan, Zhiwen Yang, Xiulan Tan, Longyu Kuang, Wenhai Zhang, et al. Demonstration of enhancement of x-ray flux with foam gold compared to solid gold. *Nuclear Fusion*, 56(3):036006, 2016.
- [159] OA Hurricane, PK Patel, R Betti, DH Froula, SP Regan, SA Slutz, MR Gomez, and MA Sweeney. Physics principles of inertial confinement fusion and us program overview. *Reviews of Modern Physics*, 95(2):025005, 2023.
- [160] A Yogo, H Daido, SV Bulanov, K Nemoto, Y Oishi, T Nayuki, T Fujii, K Ogura, S Orimo, A Sagisaka, et al. Laser ion acceleration via control of the near-critical density target. *Physical Review E*, 77(1):016401, 2008.
- [161] Luca Fedeli, Arianna Formenti, Lorenzo Cialfi, Andrea Pazzaglia, and Matteo Passoni. Ultra-intense laser interaction with nanostructured near-critical plasmas. *Scientific reports*, 8(1):3834, 2018.
- [162] Gennady Miloshevsky. Ultrafast laser matter interactions: modeling approaches, challenges, and prospects. *Modelling and Simulation in Materials Science and Engineering*, 30(8):083001, 2022.
- [163] Andrea Lübcke, Alexander A Andreev, Sandra Höhm, Ruediger Grunwald, Lutz Ehrentraut, and Matthias Schnürer. Prospects of target nanostructuring for laser proton acceleration. *Scientific reports*, 7(1):44030, 2017.
- [164] Matteo Passoni, A Sgattoni, Irene Prencipe, Luca Fedeli, David Dellasega, Lorenzo Cialfi, Il Woo Choi, I Jong Kim, Karol Adam Janulewicz, Hwang Woon Lee, et al. Toward high-energy laser-driven ion beams: Nanostructured double-layer targets. *Physical Review Accelerators and Beams*, 19(6):061301, 2016.
- [165] Richard Edward Olson, Ramon J Leeper, SA Yi, John L Kline, AB Zylstra, Robert Ross Peterson, R Shah, T Braun, J Biener, BJ Koziowski, et al. Wetted foam liquid fuel icf target experiments. In *Journal of Physics: Conference Series*, volume 717, page 012042. IOP Publishing, 2016.

- [166] AS Moore, NB Meezan, J Milovich, S Johnson, R Heredia, TF Baumann, M Biener, SD Bhandarkar, H Chen, L Divol, et al. Foam-lined hohlraum, inertial confinement fusion experiments on the national ignition facility. *Physical Review E*, 102(5):051201, 2020.
- [167] SX Hu, W Theobald, PB Radha, JL Peebles, SP Regan, A Nikroo, MJ Bonino, DR Harding, VN Goncharov, N Petta, et al. Mitigating laser-imprint effects in direct-drive inertial confinement fusion implosions with an above-critical-density foam layer. *Physics of Plasmas*, 25(8), 2018.
- [168] Vittorio Ciardiello. Theoretical study of high power laser interaction with novel nano structured foam materials for inertial confinement fusion research. Politecnico di Milano, 2022.
- [169] Maria Sole Galli De Magistris. Production of novel nanostructured targets for high-intensity laser-plasma interaction experiments. Politecnico di Milano, 2023.
- [170] Alessandro Milani. Laser-driven proton-boron nuclear fusion with nanostructured targets. Politecnico di Milano, 2024.
- [171] B Verhoff, SS Harilal, JR Freeman, PK Diwakar, and A Hassanein. Dynamics of femto-and nanosecond laser ablation plumes investigated using optical emission spectroscopy. *Journal of Applied Physics*, 112(9), 2012.
- [172] ERC ENSURE. <https://www.ensure.polimi.it>. [Online; accessed 6-May-2024].
- [173] Beverley J Inkson. Scanning electron microscopy (sem) and transmission electron microscopy (tem) for materials characterization. In *Materials characterization using nondestructive evaluation (NDE) methods*, pages 17–43. Elsevier, 2016.
- [174] Andrea Pazzaglia, Alessandro Maffini, David Dellasega, Alessio Lamperti, and Matteo Passoni. Reference-free evaluation of thin films mass thickness and composition through energy dispersive x-ray spectroscopy. *Materials Characterization*, 153:92–102, 2019.
- [175] CLPU - Centro de Laseres Pulsados. <https://www.clpu.es/en>. [Online; accessed 9-May-2024].
- [176] ENEA Frascati. <https://www.frascati.enea.it>. [Online; accessed 9-May-2024].
- [177] TARANIS - Queen’s University Belfast. <https://www.qub.ac.uk/research-centres/light-matter-interactions/Facilities/TARANISLaser/>. [Online; accessed 9-May-2024].
- [178] T Dzelzainis, G Nersisyan, D Riley, L Romagnani, H Ahmed, A Bigongiari, M Borghesi, D Doria, B Dromey, M Makita, et al. The taranis laser: A multi-terawatt system for laser-plasma investigations. *Laser and Particle Beams*, 28(3):451–461, 2010.
- [179] Alessandro Maffini, Davide Orecchia, Andrea Pazzaglia, Margherita Zavelani-Rossi, and Matteo Passoni. Pulsed laser deposition of carbon nanofoam. *Applied Surface Science*, 599:153859, 2022.
- [180] Ramin Dastanpour, Jocelyne M Boone, and Steven N Rogak. Automated primary particle sizing of nanoparticle aggregates by tem image analysis. *Powder Technology*, 295:218–224, 2016.
- [181] Jian Li, Qian Du, and Caixin Sun. An improved box-counting method for image fractal dimension estimation. *Pattern recognition*, 42(11):2460–2469, 2009.
- [182] G Odriozola, Arturo Moncho-Jorda, A Schmitt, J Callejas-Fernández, R Martínez-García, and Roque Hidalgo-Alvarez. A probabilistic aggregation kernel for the computer-simulated transition from dlca to rlca. *Europhysics Letters*, 53(6):797, 2001.
- [183] Andrea C Ferrari and John Robertson. Interpretation of raman spectra of disordered and amorphous carbon. *Physical review B*, 61(20):14095, 2000.

Bibliography

- [184] Davide Orecchia, Alessandro Maffini, Margherita Zavelani-Rossi, and Matteo Passoni. Versatile synthesis of nanofoams through femtosecond pulsed laser deposition. *Small Structures*, page 2300560, 2024.
- [185] Jacques Perrière, Chantal Boulmer-Leborgne, Ratiba Benzerga, and Sylvain Tricot. Nanoparticle formation by femtosecond laser ablation. *Journal of Physics D: Applied Physics*, 40(22):7069, 2007.
- [186] Miklos Lenner, Andrey Kaplan, Ch Huchon, and Richard E Palmer. Ultrafast laser ablation of graphite. *Physical Review B: Condensed Matter and Materials Physics*, 79(18):184105, 2009.
- [187] Paul S Epstein. On the resistance experienced by spheres in their motion through gases. *Physical Review*, 23(6):710, 1924.
- [188] AV Limaye and RE Amritkar. Theory of growth of ballistic aggregates. *Physical Review A*, 34(6):5085, 1986.
- [189] Alessandro Maffini, Francesco Mirani, Marta Galbiati, Kevin Ambrogioni, Francesco Gatti, Maria Sole Galli De Magistris, Davide Vavassori, Davide Orecchia, David Dellasega, Valeria Russo, et al. Towards compact laser-driven accelerators: exploring the potential of advanced double-layer targets. *EPJ Techniques and Instrumentation*, 10(1):15, 2023.
- [190] Andrea Pazzaglia, Luca Fedeli, Arianna Formenti, Alessandro Maffini, and Matteo Passoni. A theoretical model of laser-driven ion acceleration from near-critical double-layer targets. *Communications Physics*, 3(1):133, 2020.
- [191] A Maffini, M Cipriani, D Orecchia, V Ciardiello, A Formenti, F Consoli, M Passoni, and Yuji Fukuda. Numerical study of carbon nanofoam targets for laser-driven inertial fusion experiments. *Laser and Particle Beams*, 2023:e1, 2023.
- [192] KS Gus'kov and Sergei Yu Gus'kov. Efficiency of ablation loading and the limiting destruction depth of material irradiated by a high-power laser pulse. *Quantum Electronics*, 31(4):305, 2001.
- [193] EA Bolkhovitinov, BL Vasin, S Yu Gus'kov, I Ya Doskach, AA Erokhin, BV Kruglov, MV Osipov, VN Puzyrev, VB Rozanov, AA Rupasov, et al. Crater formation in a target under the action of a high-power laser pulse. *Plasma Physics Reports*, 30:183–186, 2004.
- [194] C Baccou, V Yahia, S Depierreux, C Neuville, C Goyon, F Consoli, R De Angelis, JE Ducret, G Boutoux, J Rafelski, et al. Cr-39 track detector calibration for h, he, and c ions from 0.1-0.5 mev up to 5 mev for laser-induced nuclear fusion product identification. *Review of Scientific Instruments*, 86(8), 2015.
- [195] MS Schollmeier, JJ Bekx, J Hartmann, E Schork, M Speicher, AF Brodersen, A Fazzini, P Fischer, E Gaul, B Gonzalez-Izquierdo, et al. Differentiating multi-mev, multi-ion spectra with cr-39 solid-state nuclear track detectors. *Scientific Reports*, 13(1):18155, 2023.